Aalto University
School of Chemical
Engineering

Aleksi Rinta-Paavola

NUMERICAL SIMULATION OF PASSIVE FIRE PROTECTION SYSTEMS

Master´s Programme in Chemical, Biochemical and Materials Engineering

Major in Chemical Engineering

Master's thesis for the degree of Master of Science in Technology submitted for inspection, Espoo, 4 September, 2017.

Supervisor Professor Simo Hostikka

Instructor D.Sc. (Technology) Hannu-Petteri Mattila

Aalto-yliopisto
Kemian tekniikan korkeakoulu

Aalto-yliopisto, PL 11000, 00076 AALTO
www.aalto.fi

Diplomityön tiivistelmä

Tekijä Aleksi Rinta-Paavola

Työn nimi Passiivisten palontorjuntajärjestelmien numeerinen mallintaminen

Laitos Rakennustekniikan laitos

Professuuri Paloturvallisuustekniikka

Työn valvoja Prof. Simo Hostikka

Työn ohjaaja TkT Hannu-Petteri Mattila

Päivämäärä 4.9.2017 **Sivumäärä** 110+46 **Kieli** Englanti

Tiivistelmä

Kivivillatuotteiden palotestauksen nykykäytäntö on testaaminen polttokokeissa. Kokeissa villalevy asetetaan vasten uunia, jonka palotila noudattaa määriteltyä lämpötilakäyrää, esimerkiksi ISO 834-1 -standardin mukaista. Kokeet vievät kuitenkin aikaa ja resursseja, joten tarve villan käyttäytymistä polttokokeen aikana kuvaavalle simulaatiomallille on ilmeinen. Kyseisenlaista mallia voidaan käyttää laajempien kokonaisuuksien tulipalomallinnusten ja riskianalyysien perustana. Työn tavoitteena on muodostaa numeerinen simulaatiomalli, joka on validoitu toimimaan suurelle joukolle erilaisia villoja.

Mallinnuksen työkaluina olivat MATLAB R2017a ja Fire Dynamics Simulator 6.5.3 (FDS). Sekä MATLABiin rakennettu ja FDS:n olemassa ollut lämmönjohtavuusmalli perustuvat aikariippuvaiseen lämmönsiirtoyhtälöön. Työssä selvitettiin kivivillan termiset ominaisuudet ja reaktioparametrit. Termiset ominaisuudet selvitettiin kirjallisuudesta ja implementoitiin sellaisenaan, verraten mahdollisiin kokeellisiin mittauksiin. Reaktioparametrit selvitettiin termoanalyyttisesti ja sovitettiin malliin kylmän puolen konvektiolämmönsiirron kanssa vastaamaan kokeellisia tuloksia. Pienen mittakaavan polttokoetta kuvaamaan kehitettiin erilliset yksiulotteiset mallit sekä MATLABilla että FDS:llä. Suuren mittakaavan polttokokeita mallintava kaksiulotteinen malli tehtiin FDS:llä sen betatestausvaiheessa olevalla kolmiulotteisella lämmönjohtavuusratkaisijalla.

Lopputuloksena todettiin, että validia yksiulotteista simulaatiomallia kaikille eri villatyypeille ei ole mahdollista saada aikaan ilman laajoja jatkotutkimuksia. Matalan tiheyden ja syttyvän aineen pitoisuuden villoilla mallien sopivuus oli tyydyttävällä tasolla, mutta tiheiden ja paljon sideainetta tai öljyä sisältävien villojen sopivuus oli ongelmallisempi. Merkittävimpiä syitä on todennäköisesti virheellinen olettama hapen riittävyydestä villan sisäisissä palamisreaktioissa koko polttokokeen ajaksi ja epävarmuus kokeellisiin mittauksiin sovitetussa lämmönjohtavuuden säteilykomponentissa.

Kaksiulotteinen malli jäi puutteelliseksi betavaiheessa olevan kolmiulotteisen lämmönjohtavuusratkaisijan keskeneräisyyden vuoksi. FDS:n pyrolyysimoduuli ei ole kytketty kolmiulotteiseen ratkaisijaan, mikä tekee reaktioden mallintamisen mahdottomaksi. Lisäksi lämmönsiirto kaasusta kiinteään faasiin todettiin mahdottomaksi mallintaa nykyisessä kolmiulotteisessa mallissa.

Avainsanat Paloeriste, kivivilla, palotestaus, numeerinen mallinnus, lämmönsiirto, termoanalyyttiset menetelmät, MATLAB, FDS

Aalto University
School of Chemical
Technology

Aalto University, P.O. BOX 11000, 00076 AALTO
www.aalto.fi

Abstract of master's thesis

Author Aleksi Rinta-Paavola

Title of thesis Numerical Simulation of Passive Fire Protection Systems

Department Department of Civil Engineering

Professorship Fire Safety Engineering

Thesis supervisor Prof. Simo Hostikka

Thesis advisor D.Sc. (Technology) Hannu-Petteri Mattila

Date 4.9.2017 **Number of pages** 110+46 **Language** English

Abstract

The current practice in fire testing of stone wool products is to study them in fire resistance tests. In these experiments a wool slab is installed against a furnace whose temperature follows a certain temperature curve, for example the one set by the standard ISO 834-1. These experiments consume time and resources, so a need exists for a simulation model describing behaviour of a wool during a fire test. Such model could be employed in fire modelling of larger entities and as a basis of fire risk analyses. The objective of this thesis is to form a numerical simulation model that is validated to be operational for several different types of wool.

MATLAB R2017a and Fire Dynamics Simulator 6.5.3 (FDS) were utilized as simulation tools. Both thermal conductivity models, the one built into MATLAB and the one already existing in FDS are based on transient heat transfer equation. In this work thermal properties and reaction parameters of wool were solved. Thermal properties were found out from literature and implemented as such, comparing to possible experimental measurements. Reaction parameters were solved thermoanalytically and were fitted in model along with the cold side convective heat transfer to correspond to experimental results. To model small scale fire tests, a one-dimensional model was built in both MATLAB and FDS. A two-dimensional model to describe large scale fire tests was built in FDS utilizing its three-dimensional thermal conductivity solver, still in beta phase.

It was concluded that it is not possible to obtain a valid one-dimensional model for all types of wool without extensive further research. In wools with low densities and combustible fractions, the fit of simulation was on a satisfactory level, but with wools that are dense or rich in binder or oil, the fitting was more problematic. One of the most significant reasons for this is probably the erroneous assumption on readily available oxygen inside wool for combustion over the whole test and uncertainties in the fitted radiative component of thermal conductivity.

The two-dimensional model was left defective due to incompleteness of the three-dimensional thermal conductivity solver. The FDS pyrolysis module is not yet coupled to the three-dimensional solver, thus disabling the opportunity to model reactions. In addition, heat transfer from gaseous to solid phase was judged to be impossible to model in the current version of the three-dimensional model.

Keywords Fire insulator, stone wool, numerical simulation, heat transfer, thermoanalytical methods, MATLAB, FDS

Preface

This Master's thesis was done for Paroc Group Oy Materials Research and Innovation department at Parainen, Finland, during February 2017 – August 2017. This thesis is an interdisciplinary project, since it has been a collaboration between School of Chemical Engineering and School of Engineering at Aalto University.

Design and development of stone wool and other fire protection materials are currently based on resource-, and time consuming fire resistance tests carried out in test furnaces. This acts as the motivation for the goal of this thesis, which is to develop a validated numerical simulation model that predicts heat transfer and reactions inside a wool during a fire resistance test. The outcome of the work is a simulation model, which describes high-temperature heat transfer inside a wool and considers the effect of exothermic reactions of wool by a reaction scheme formulated in this work.

I would like to present my thanks to Professor Simo Hostikka for giving me the opportunity for this interesting interdisciplinary thesis project. I am grateful of his support with the numerical calculation tools and guidance throughout the thesis work. I am already looking forward to our next project, my doctoral thesis.

I would equally like to thank D.Sc. (Technology) Hannu-Petteri Mattila from Paroc Group of his expertise and bearing with my barrage of questions. I appreciate his commitment to this project and giving all the help necessary for the completion of my thesis. I also thank Paroc Group Oy for funding my thesis through Foundation for Aalto University Science and Technology.

Last but not least, warm thanks to my family for their support and encouragement to take the leap of faith of starting a doctoral thesis in a new field. Thanks belong also to my friends with whom I have shared all of the ups and downs and some seriously bad humor over this half a year.

Espoo, August 31, 2017

Aleksi Rinta-Paavola

Table of contents

List of symbols

A	Area	[m^2]
	Pre-exponential factor	$\left[\frac{1}{\mathrm{s}}\right]$
c	Speed of light	$299792458\ \frac{\mathrm{m}}{\mathrm{s}}$
c_p	Specific heat capacity in constant pressure	$\left[\frac{\mathrm{J}}{\mathrm{kg \cdot K}}\right]$
C	Degree of conversion	[dimensionless]
D	Radiation distribution factor	[dimensionless]
D_f	Fiber diameter	[m]
e	Specific extinction coefficient	$\left[\frac{\mathrm{m}^2}{\mathrm{kg}}\right]$
E_a	Activation energy	$\left[\frac{\mathrm{J}}{\mathrm{mol}}\right]$
E_b	Blackbody emissive power	$\left[\frac{\mathrm{W}}{\mathrm{m}^2}\right]$
$E_{b\lambda}$	Spectral blackbody emissive power	$\left[\frac{\mathrm{W}}{\mathrm{m}^2}\right]$
f	Ratio of insulation material density to fiber material density	[dimensionless]
g	Gravitational acceleration of Earth	$9.81\ \frac{\mathrm{m}}{\mathrm{s}^2}$
Gr	Grashof number	[dimensionless]
h	Convective heat transfer coefficient	$\left[\frac{\mathrm{W}}{\mathrm{m}^2\mathrm{K}}\right]$
h	Planck's constant	$6.626176 \cdot 10^{-34}$ Js
k	Thermal conductivity	$\left[\frac{\mathrm{W}}{\mathrm{m \cdot K}}\right]$
k_B	Boltzmann constant	$1.380662 \cdot 10^{-23}\ \frac{\mathrm{J}}{\mathrm{K}}$
Kn	Knudsen number	[dimensionless]
L_c	Characteristic length scale	[m]
M	Molar mass	$\left[\frac{\mathrm{g}}{\mathrm{mol}}\right]$
	Extinction coefficient	$\left[\frac{1}{\mathrm{m}}\right]$
n	Refractive index	[dimensionless]

	Sample size	[dimensionless]
N	Scattering coefficient	$\left[\frac{1}{\mathrm{m}}\right]$
N_A	Avogadro number	$6.022045 \cdot 10^{23}\ \frac{1}{\mathrm{mol}}$
N_s	Reaction order	[dimensionless]
p	Pressure	[pa; bar]
P	Absorption coefficient	$\left[\frac{1}{\mathrm{m}}\right]$
Pr	Prandtl number	[dimensionless]
q^c	Convective heat flux	$\left[\frac{\mathrm{W}}{\mathrm{m}^2}\right]$
q^r	Radiative heat flux	$\left[\frac{\mathrm{W}}{\mathrm{m}^2}\right]$
$\dot{Q}$	Heat flow	[W]
$\dot{Q}'''$	Heat release rate per unit volume	$\left[\frac{\mathrm{W}}{\mathrm{m}^3}\right]$
r	Reaction rate	$\left[\frac{1}{\mathrm{s}}\right]$
R	Universal gas constant	$8.31441\ \frac{\mathrm{J}}{\mathrm{K \cdot mol}}$
R^2	Coefficient of determination	[dimensionless]
s	Standard deviation	[varies]
S	Shape index	[dimensionless]
t	Time	[s; min]
	Test quantity in *t*-test	[dimensionless]
T	Temperature	[K; °C]
x	Mass fraction	[dimensionless]
	Length coordinate	[m]
X_p	Relative amount of unconverted matter	[dimensionless]
y	Volume fraction	[dimensionless]
	Second length coordinate in 2-D model	[m]

Greek letters

α	Thermal diffusivity	$\left[\frac{\mathrm{m}^2}{\mathrm{s}}\right]$
	Fraction of fibers oriented parallel to heat flux	[dimensionless]
β	Rosseland mean extinction coefficient	$\left[\frac{1}{\mathrm{m}}\right]$
	Heating rate	$\left[\frac{°\mathrm{C}}{\mathrm{s}}\right]$
	Thermal expansion coefficient	$\left[\frac{1}{\mathrm{K}}\right]$
γ	Specific heat ratio	[dimensionless]
$\delta_r T$	Relative uncertainty of simulation model	[%]
ΔH_r	Heat of reaction	$\left[\frac{\mathrm{J}}{\mathrm{kg}}\right]$
Δt	Time step size	[s]
ΔT	Temperature difference	[K]
	Pyrolysis range	[K]
Δx	Mesh size	[m]
ε	Emissivity	[dimensionless]
λ	Mean free path	[m]
	Wavelength	[m]
Λ	Parameter in air thermal conductivity correlation	$4.358 \cdot 10^{-3}\ \frac{\mathrm{W}}{\mathrm{m \cdot K}}$
ν	Kinematic viscosity	$\left[\frac{\mathrm{m}^2}{\mathrm{s}}\right]$
ν_s	Yield of solid residue as mass fraction	[dimensionless]
ξ	Fibrous fraction of mineral material	[dimensionless]
ρ	Density	$\left[\frac{\mathrm{kg}}{\mathrm{m}^3}\right]$
σ	Stefan-Boltzmann constant	$5.670367 \cdot 10^{-8}\ \frac{\mathrm{W}}{\mathrm{m}^2\mathrm{K}^4}$
τ	Dimensionless time (Fourier number)	[dimensionless]
φ	Porosity	[dimensionless]

ϕ	Fiber angle of inclination from horizontal level	[°; rad]

Abbreviations

CFD	Computational Fluid Dynamics
DSC	Differential Scanning Calorimetry
DTA	Differential Thermal Analysis
FDS	Fire Dynamics Simulator
HRRPUA	Heat Release Rate Per Unit Area
HRRPUV	Heat Release Rate Per Unit Volume
LOI	Loss On Ignition
NIST	National Institute of Standards and Technology
TG	Thermogravimetry

1 Introduction

The objective of this master's thesis is to create a numerical simulation model to describe high temperature heat transfer in stone wool. In this thesis, a model to describe heat transfer is created first in one dimension. Consequently, a two-dimensional model is implemented utilizing information from the one-dimensional model. Finally, these models are validated to predict thermal behavior of stone wool over a set of initial values describing the material properties. A validated model to describe behavior of wool under fire conditions could be employed in various research tasks within insulation industry and in building of fire risk analyses.

1.1 Background for research and goals

Stone wool is an insulation material widely used in construction industry as passive fire protection systems. By definition, passive fire protection systems are such measures against fire spreading that work irrespective of human action or functionality of technical apparatus (Sutton, 2015). Fireproofing by incombustible insulation materials falls within this category. Notwithstanding the end-application of a passive fire protection system, low thermal conductivity, low density and incombustibility are required. (Sutton, 2015) Stone wool meets these criteria.

Development of passive fire protection materials is based on standardized test routines. A simulation model to predict behavior of different product types under fire would be a useful tool in product development and performance assessment for stone wool products. A validated simulation tool would also be helpful in building fire risk analyses, as simulation is commonly employed in this field (Steel Construction Institute, 2014). Therefore a need for such tool does clearly exist.

Some research have already been done in numerical modeling of behavior of stone wool under high temperatures, e.g. in the master's thesis of Juhani Nurmi (2016). However, as it is not the main topic of his thesis, the simulation model built in his thesis contains some simplifications. It is not validated to work for different stone wools of various properties, and is only in one dimension. A lot of other published research focuses only on prediction of thermal conductivity of the insulation material (Andersen and Dyrbøl, 1998; Karamanos et al., 2004; Veiseh and Hakkaki-Fard, 2009, Livkiss et al., 2017). A valid model describing simultaneously heat transfer and reactions inside stone wool is therefore lacking.

Since this thesis focuses exclusively on modeling of stone wool fire behavior, a more profound approach could be afforded. The goal of this thesis is to build a validated numerical simulation model for heat transfer in stone wool in high temperatures. The model developed in this thesis takes into account the fibrous nature of the stone wool material. It examines contribution of each type of heat transfer separately to heat transmission within a wool. The types of heat transfer considered are conduction, convection and radiation. The model includes heat release by thermal decomposition of binder resin matrix and dust binding oil and solid phase reactions in the stone wool material. These solid phase reactions include, but may not be limited to crystallization and oxidation of fiber material.

One further goal of this thesis is to gain understanding of physical and chemical phenomena occurring inside stone wool at high temperatures. Contribution of many phenomena are not yet well known, and uncertainties remain for example in the role of solid phase reactions, high temperature thermal conductivity, reaction kinetics of organic fraction decomposition and availability of oxygen for this process.

1.2 Research methods

A one-dimensional model for heat transfer is executed in both MATLAB R2017a and Fire Dynamics Simulator (FDS) version 6.5.3. MATLAB, developed by MathWorks, Inc., is a versatile and a widely known program and programming language in numerical calculation. FDS is a computational fluid dynamics (CFD) tool for fire modeling, developed in co-operation by National Institute of Standards and Technology (NIST) and VTT Technical Research Centre of Finland.

Firstly, a numerical model of one-dimensional heat transfer is developed in MATLAB, based on numerical approximation of the transient heat transfer equation. This model will include thermal conductivity and specific heat capacity as correlations as functions of temperature. The modeling of heat release rate by decomposition reactions is based on Arrhenius equation. In FDS, same properties are defined as a function of temperature as a series of ramps. Release of heat by exothermic decomposition of fiber binders is modeled by the FDS pyrolysis model. Initial kinetic parameters were found out by thermoanalytic methods. These parameters are fitted to correspond to experimental data from small scale fire tests, carried out in a $0.6 \cdot 0.6$ m furnace. Other fitted parameters include the convective heat transfer in the cold side, thickness of the furnace walls that act as the radiative source on the hot side, and the radiative component of thermal conductivity.

Thermal properties of conductivity and specific heat capacity for each material present are obtained from literature and compared to experimental measurements when applicable.

A two-dimensional model of heat transfer in stone wool is built by using the three-dimensional heat transfer solver of FDS, which is in a beta testing phase at the time of writing. The aim of the two-dimensional model is to predict effects of steel profiles inside the test structure in large scale fire tests, carried out in 3 · 3 m furnaces.

Finally, models built with both MATLAB and FDS need to be validated. Validation is defined as a process which determines how precisely the real phenomenon corresponds to the prediction offered by a simulation model. A validation process consists of three steps, which are “comparing model predictions with experimental measurements, quantifying the differences in light of uncertainties in both the measurements and model inputs, and deciding if the model is appropriate for the given application”. (McGrattan et al., 2017, pp. 1-3) Herein, the validation process is carried out by comparing simulated temperature developments obtained by both MATLAB and FDS models to actual experimental results. Experimental fire resistance tests for various stone wool types are carried out in a furnace following a design fire temperature program defined by the standard ISO 834-1. Temperature development during these experiments is measured by thermocouples placed on the cold side of the examined stone wool slab.

2 Theory

This chapter discusses first stone wool production technology to elaborate the causes of its fibrous nature. Then, general material properties are discussed, and finally the underlying phenomena of heat transfer present in the stone wool material. Some different numerical calculation methods for heat transfer in fibrous materials in the previous research are discussed as well.

2.1 Stone wool manufacturing process

Figure 1 presents the scheme of stone wool manufacturing process.

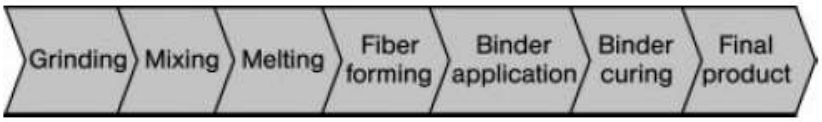

Figure 1. Stone wool manufacturing process principle (Pico et al., 2012).

Grinding and mixing refer to comminution of rock feedstock and adjusting the feed properties by combining several different minerals into a single raw material stream (Pico et al., 2012). Nowadays, in addition to minerals of suitable compositions, for example basalt (Pico et al., 2012) or amphibolite (Karamanos et al., 2004), recycled materials such as glass or blast furnace slag could be used to reduce environmental impact (Pico et al., 2012). Additives are introduced in order to improve product quality or process performance. For example, the rock melt viscosity could be controlled by addition of limestone. (Karamanos et al., 2004; Pico et al., 2012)

The pretreated mineral feedstock is melted in a furnace at a temperature of approximately 1500 °C (Karamanos et al., 2004). Melting is carried out in industrial scale either in a glass melting tank furnace, which is similar to type used in glass production, or in a cupola furnace. Tank furnaces could be powered either by fossil fuels or could be all electric, while cupola furnaces are traditionally coke-fired. Cupola furnaces produce less uniform rock melt and are generally smaller in production capacity, but they could operate on coarser feed. (Pico et al., 2012)

Stone wool obtains its fibrous structure in centrifugation phase. Internal and external centrifugal processes are the two conventional methods in industrial stone wool manufacturing. Although in the internal centrifugal process the feed is mainly glass melt, rock melts of suitable composition could be used as well. Figure 2 presents both processes. (Pico et al., 2012)

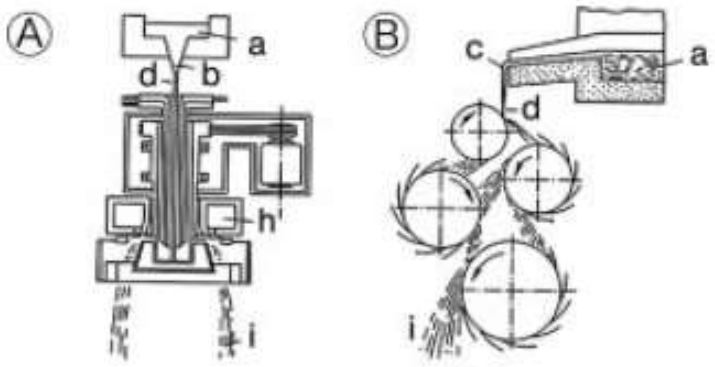

Figure 2. A) Internal and B) external centrifugal process. a) Rock melt, b) bushing, c) spout, d) melt stream, h) burner, i) fiber stream. (Pico et al., 2012)

In the internal centrifugal process, melt is introduced into a rotating cylinder, where its revolution speed in the order of 2000 rpm drives the melt to the cylinder walls. The peripheral wall of the cylinder, in the figure visible in the bottom, is perforated. Primary fibers released from these holes are entrained by hot gases from the burner and drawn to longer fibers. (Pico et al., 2012)

In the external centrifugal process the melt flow is introduced into a rotor in the top, where it is distributed to additional rotors (Pico et al., 2012). Melt is driven off the rotors as droplets and stretched to fibers due to centrifugal forces (Pico et al., 2012; Chapelle et al., 2014). In the external centrifugal process a large portion of raw material, even 40 wt-% will remain as droplets in the ready product (Pico et al., 2012). The external centrifugal process is the most dominant one of these two (Chapelle et al., 2014), and also the production technology of stone wool materials studied in this thesis.

Formed fibrous filaments are collected pneumatically to yield an unformed stone wool mat and injected with binder resin and dust-binding oil. Phenol-formaldehyde resin is the most common option but others do exist as well. This injected stone wool is then pressed into plate form and fed continuously on a conveyor belt into a binder curing oven, where the resin is hardened. At little below 200 °C resins start combining with the fibers, and finally at around 250 °C resins are fully polymerized

and hardened, giving stone wool the form of a hard plate. As a final stage, the stone wool plate could be cut into any desired geometry. (Karamanos et al., 2004; Pico et al., 2012; Chapelle et al., 2014) Resins and oils in the wool, accounting at maximum for 10 and 1 wt-% of the wool respectively (Pico et al., 2012), are also the components decomposing in exothermic reactions when the wool is under heating.

2.2 Structure of stone wool

The fibrous nature of stone wool affects its mechanical properties and its usability as a thermal, and also as an acoustic insulator (Chapelle et al., 2014). Stone wools are highly porous fiber networks materials. Porosity, i.e. air volume fraction within the material can exceed 98 %. Specific surface area is typically between 0.1 and 0.25 m^2/g. (Andersen and Dyrbøl, 1998; Karamanos et al., 2004; Pico et al., 2012; Chapelle et al., 2014) Thermal insulation capacity is specifically based on this air enclosed within mineral fibers (Karamanos et al., 2004).

Because of its fibrous and porous structure, stone wool finds application also as acoustic insulators (Jensen and Raspet, 2010; Chapelle et al., 2014). Acoustic perturbations are dissipated due to their thermal and viscous interactions with pore walls (Jensen and Raspet, 2010; Peyrega and Jeulin, 2013). Since acoustic properties of stone wool are not within the scope of this thesis, they are not discussed in more detail.

Most of the fibers are 3 to 6 µm in diameter and at most, some centimeters long (Pico et al., 2012; Chapelle et al., 2014). However, these fiber properties are not homogenous, but instead follow always some certain distribution (Chapelle et al., 2014). For example, fiber diameter distribution is centered around two peaks at 2.8 and 6.6 µm in the commercial stone wool product analyzed in the research of Chapelle et al. (2014). Length distribution is centered on short fibers, at around 100 µm (Chapelle et al., 2014). These fiber properties depend on employed production technology and properties of rock melt. Properties of individual fibers are not that important, since the combination of the fibers and binder determines the end product to a greater extent. (Pico et al., 2012)

Spatial orientation of fibers follow a certain distribution (Chapelle et al., 2014). A significant part of fibers is randomly oriented, (Chapelle et al., 2014; Buska et al., 2015) especially in the horizontal plane defined by x-, and y-axes where no preferential orientation was detected in the research of Chapelle et al. (2014). On

the contrary, Buska and Mačiulaitis (2007) reported the dominant fiber direction in the xy-plane to be along the axial direction of the conveyor belt of the production line. Orientation to the direction of perpendicular z-axis is more regular. Buska et al. (2015) and Pico et al. (2012) mention that most fibers are parallel to the horizontal xy-plane. Chapelle et al. (2014) instead found out that the fiber orientation distribution with respect to z-axis is centered at around 40° angle from the xy-plane in the investigated wool. The reported distribution shows that a great degree of fibers are oriented randomly also in the z-direction. Fiber orientation and the three-dimensional structure of stone wool is elaborated here in Figure 3, which presents a three-dimensional image of a stone wool fiber network obtained by x-ray tomography. (Chapelle et al., 2014)

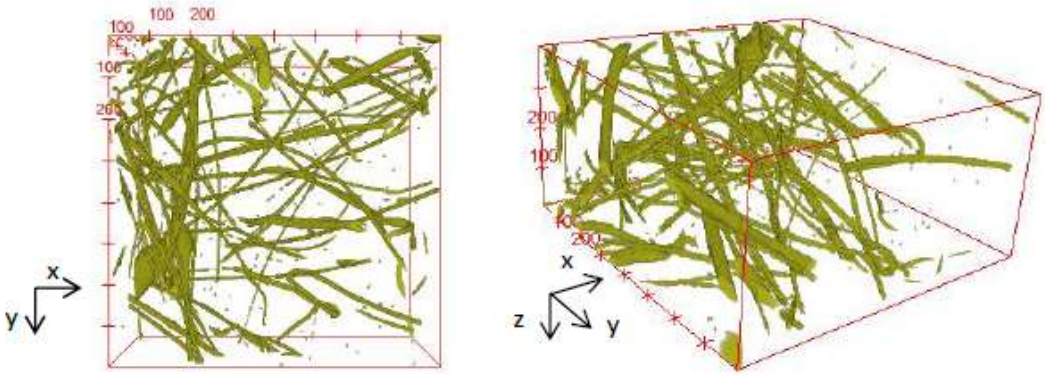

Figure 3. Stone wool fiber network structure, as obtained by x-ray tomography imaging. (Chapelle et al., 2014)

This aforementioned anisotropy in the fibrous microstructure affects directly some macroscopical properties of the material, namely thermal conductivity and mechanical strength. Thermal conductivity of wool is the highest along the direction the fibers are aligned. (Karamanos et al., 2004) In this case, a larger portion of heat could be conducted directly in the solid phase that has a thermal conductivity of one or two order of magnitudes higher than air, depending on the temperature (Stephan and Laesecke, 1985; Hofmeister et al., 2016). Otherwise, more heat transfer should have to occur across the air cavities within the material (Karamanos et al., 2004).

Buska and Mačiulaitis (2007) found out that stone wool could sustain a lot of mechanical stress in the dominant fiber direction. Buska and Mačiulaitis (2007) measured in their research the stress required to compress a sample into 90 % of its original volume, i.e. to deform it by 10 %. As a result, along the dominant fiber

direction a larger compressive stress was required to cause similar displacements than in other directions. However, even before this 10 % deformation was achieved when compressing along the fiber direction, the stone wool sample did rupture at around 5-6 %. In other directions, material did not rupture even under higher deformations of tens of percents. Therefore, one could deduce that stone wool is rather brittle material in the fiber direction. Higher wool density seems to increase the compressive strength (Buska and Mačiulaitis, 2007). Higher binder amount also contributes to higher mechanical strength (Steponaitis et al., 2012).

2.3 Heat transfer in stone wool

Heat transfer occurs by conduction, radiation or convection. The first two are the most prevalent in stone wool, when heat transfers by conduction along the fibers or across the stagnant air gaps, or by radiation as chain of photon absorption, emission and scattering between individual fibers. Many papers argue that the contribution of convection into heat transfer inside the stone wool material is insignificant, and can thus be neglected. (Andersen and Dyrbøl, 1998; Tleoubaev, 1998; Karamanos et al., 2004; Veiseh and Hakkaki-Fard, 2009) Instead, convection becomes a relevant heat transfer mechanism only in complete buildings, where stone wool slabs are installed along with other structures. In real constructions, air gaps between the insulation layer and other structures are difficult to avoid. Air gaps wider than 5 mm are already sufficient to give rise to convective heat transfer. Presence of convection could lead to increases of up to 12-13 % in heat flow through the wall. (Stankevičius et al., 2013)

At a room temperature, radiation accounts approximately for 30 % of the total heat transfer (Andersen and Dyrbøl, 1998). When temperature increases, it is reasonable to assume that the portion of radiative heat transfer is likely to increase. Findings from research of Spinnler et al. (2004), where other ceramic fibrous insulation material was under examination, support this. Figure 4 shows that radiative fraction of heat transfer becomes increasingly dominant, while temperature rises.

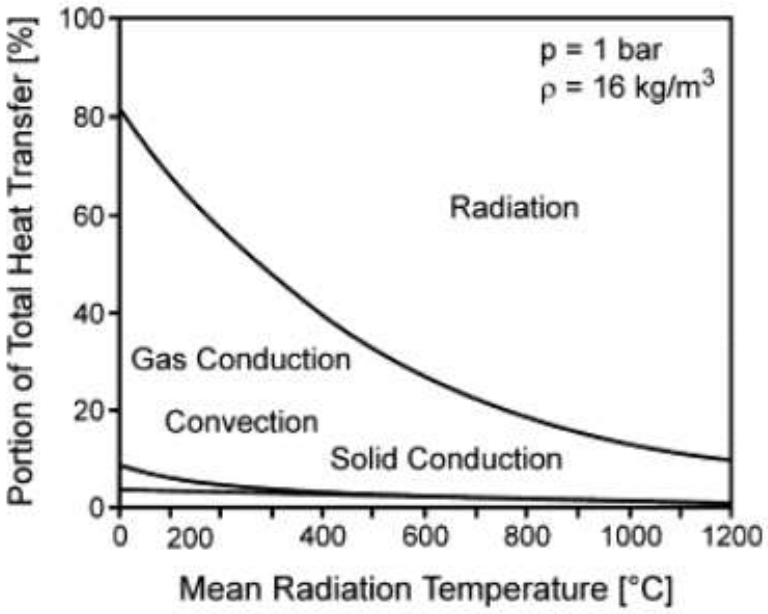

Figure 4. Fractions of different heat transfer mechanisms as a function of temperature (Spinnler et al., 2004).

This is based on the thermal emissive power of a body increasing in proportion to the fourth power of temperature. This relation is known as the Stefan-Boltzmann law, presented as Equation 1.

$$q^r = \varepsilon\sigma T^4 = \varepsilon E_b \quad (1)$$

where ε is emissivity, $\sigma = 5.670367 \cdot 10^{-8}\ \frac{\mathrm{W}}{\mathrm{m^2K^4}}$ is the Stefan-Boltzmann constant and E_b is the blackbody emissive power.

As Figure 4 shows, gas conduction is the most important mechanism of heat transfer at low temperatures in fibrous insulators. It is surpassed by radiation as temperature increases. If this data is applicable also to stone wool, assumption of negligible role of convection is sensible. The figure clearly shows that its role goes nonexistent at elevated temperatures, and heat transfer at high temperatures is specifically the point of interest in this thesis.

As discussed in Section 2.2, heat transfer by conduction varies anisotropically with respect to the fiber orientation (Karamanos et al., 2004). This applies also for the radiative heat transfer. If fibers are oriented in perpendicular to the direction of thermal radiation, a lot more back-scattering is induced than in the case of parallel orientation. This reduces the magnitude of radiant heat transfer. (Lee, 1989)

Equation 2 describes transient heat transfer (Drysdale, 2011). Relevant equations for one-, and two-dimensional heat transfer could be derived from Equation 2, and are presented as Equations 3 and 4, respectively. Equations 3 and 4 take into account the change of thermal conductivity as a function of temperature.

$$\nabla^2 T = \frac{1}{\alpha}\frac{\partial T}{\partial t} - \frac{\dot{Q}'''}{k} = \frac{1}{\frac{k}{\rho c_p}}\frac{\partial T}{\partial t} - \frac{\dot{Q}'''}{k} \quad (2)$$

$$\rho c_p \frac{\partial T}{\partial t} = \frac{\partial}{\partial x}\left(k\frac{\partial T}{\partial x}\right) + \dot{Q}''' \quad (3)$$

$$\rho c_p \frac{\partial T}{\partial t} = \frac{\partial}{\partial x}\left(k\frac{\partial T}{\partial x}\right) + \frac{\partial}{\partial y}\left(k\frac{\partial T}{\partial y}\right) + \dot{Q}''' \quad (4)$$

In these equations, T is temperature, t is time, $\dot{Q}'''$ is heat release rate per unit volume, x and y are length along their respective coordinate axis directions. k is thermal conductivity, ρ is density, c_p is specific heat capacity and α is thermal diffusivity which is thermal conductivity divided by the product of density and specific heat capacity. Effect of exothermic binder decomposition and stone wool fiber high temperature reactions could be introduced into the heat transfer model by the source term $\dot{Q}'''$.

If heat transfer inside a stone wool material is described with a one-equation model according to or derived from Equation 2, an effective thermal conductivity k_{eff} should be defined. It accounts for heat transfer both by conduction either in fibers or over cavities, and by radiation. For example, Karamanos et al. (2004) present a method, where thermal conductivities by solely one mechanism are calculated separately, and then k_{eff} is obtained as their sum according to Equation 5.

$$k_{eff} = k_{cond} + k_{rad} \quad (5)$$

where k_{cond} and k_{rad} are the conductive and radiative components of thermal conductivity, respectively.

It is also possible to examine radiative heat transfer as a separate phenomenon, independent of other heat transfer in the system. This requires formation of a separate model for radiative heat flux q^r inside the stone wool material. Radiative heat flux could be combined to one-dimensional heat transfer model as shown in Equation 6. Radiative heat flux is coupled into the equation by the term $\frac{\partial q^r}{\partial x}$, which represents its gradient, or the sum of absorption and emission over a differential volume element. This kind of approach in one-dimensional analyses has been taken by several researchers in modelling of heat transfer through fibrous materials. (Andersen and Dyrbøl, 1998; Yuen et al., 2003; Veiseh and Hakkaki-Fard, 2009)

$$\rho c_p \frac{\partial T}{\partial t} = \frac{\partial}{\partial \mathrm{x}}\left(k \frac{\partial T}{\partial x}\right) + \dot{Q}''' - \frac{\partial q^r}{\partial x} \quad (6)$$

2.4 Previous research

A lot of previous numerical simulation effort to model heat transfer in fibrous insulators has been devoted specifically to modelling of radiative heat transfer (Andersen and Dyrbøl, 1998; Asllanaj et al., 2002; Yuen et al., 2003; Veiseh and Hakkaki-Fard, 2009). The whole conductive component is in some cases solved as a function of temperature just by an empirical correlation (Asllanaj et al., 2002; Veiseh and Hakkaki-Fard, 2009). However, some more sophisticated methods for determination of heat transfer by conduction do exist, which take into account fiber orientation. Such methods are for example the ones presented in the works of Futschik and Witte (1993) and Karamanos et al. (2004). Equation 7 presents the method used by Karamanos et al. (2004).

$$k_{cond} = k_s^* + \frac{k_g^* - k_s^*}{1 + \frac{f}{1+f}\left(1 + z\frac{k_g^* - k_s^*}{k_g^* + k_s^*}\right)} \quad (7)$$

where k_{cond} is conductive component of thermal conductivity, k_s^* and k_g^* are thermal conductivities of solid and gas phase, respectively, f is the ratio of insulation material density to fiber material density and z is a coefficient dependent on fiber orientation. It should be noted, that k_s^* and k_g^* are not continuous phase values k_s and k_g but instead calculated from them according to Equations 8 and 9, respectively. Hence, they are denoted by asterisk.

$$k_s^* = f^2 k_s \quad (8)$$

$$k_g^* = \frac{k_g}{\Omega + 2\Psi \frac{2-\alpha}{\alpha} \cdot \frac{2\gamma}{\gamma} \cdot \frac{Kn}{Pr}} \quad (9)$$

where $\alpha \in [0,1]$ is energy exchange factor between molecules of air and fibers, γ is specific heat ratio, Kn is Knudsen number given by Equation 10 and Pr is the Prandtl number. Values of parameters Ω and Ψ are as follows: $\Omega = 1$, $\Psi = 0$ when $Kn < 0.01$, $\Omega = 1$, $\Psi = 1$, when $0.01 < Kn < 10$ and $\Omega = 0$, $\Psi = 1$, when $Kn > 10$. In Knudsen number λ is the mean free path of an air molecule and L_c is the characteristic length scale, calculated according to Equation 11.

$$Kn = \lambda / L_c \quad (10)$$

$$L_c = \frac{\pi}{4} \frac{D_f}{f} \quad (11)$$

where D_f is the fiber diameter.

Futschik and Witte (1993) present a method developed originally by Bankvall (1972), which first calculates thermal conductivity of a fibrous insulating material in directions both perpendicular and parallel to fiber orientation. Equations 12 and 13 define these conductivities, respectively.

$$k_{perp} = \frac{k_g k_s}{\varphi k_s + (1-\varphi) k_g} \quad (12)$$

$$k_{para} = \varphi k_g + (1-\varphi) k_s \quad (13)$$

where k_{perp} and k_{para} are thermal conductivities in perpendicular and parallel directions, respectively and φ is porosity. These equations could be combined to yield k_{cond} according to Equation 14, if the fraction α of fibers oriented in parallel to heat flux are known. (Futschik and Witte, 1993)

$$k_{cond} = \alpha k_{para} + (1-\alpha) k_{perp} \quad (14)$$

Futschik and Witte (1993) also refer to unit cell conduction model by Imakoma et al. (1990). It is a separately presented model from the previous one, but it could be applied to give k_{cond} as a function of fiber angle of inclination ϕ from the horizontal plane according to Equation 15.

$$k_{cond} = k_{para} \sin^2 \phi + k_{perp} \cos^2 \phi \quad (15)$$

Naturally, the values of k_s and k_g depend on temperature. It is easily understandable, why conductive heat transfer is given such a minor emphasis in existing literature. After all, it is simpler and more straightforward phenomenon than radiative heat transfer, which includes a multitude of complex exchanges between individual fibers.

If radiative heat flux is examined as a separate phenomenon, it is connected into the heat transfer model by the Equation 6. In the one-dimensional case, the radiative heat flux is most conventionally modeled with one-, or two-flux models (Linford et al., 1974; Andersen and Dyrbøl, 1998; Yuen et al., 2003; Spinnler et al., 2004; Veiseh and Hakkaki-Fard, 2009).

In a one-flux model, radiative heat flux within the material is calculated as a function of penetration depth into material, taking into account the effect of backscattering and emissive power from the wall opposing the heat flux (Yuen et al., 2003; Veiseh and Hakkaki-Fard, 2009). Equation 16 presents as an example the model presented by Veiseh and Hakkaki-Fard (2009).

$$q_r(x) = \sigma(\varepsilon_H D_{Hi} T_H^4 - \varepsilon_H D_{iH} T_i^4) + \sigma(\varepsilon_i D_{iC} T_i^4 - \varepsilon_C D_{Ci} T_C^4)$$
$$+\sigma \sum_{j=1}^{i} \left(\varepsilon_j D_{ji} T_j^4 - \varepsilon_i D_{ij} T_i^4\right) + \sigma \sum_{j=i+1}^{n} \left(\varepsilon_i D_{ij} T_i^4 - \varepsilon_j D_{ji} T_j^4\right) \qquad (16)$$

where x equals to the location of i:th discretization plane, when the total number of planes is n. Hot and cold bounding plates are denoted by subscripts H and C, respectively. D_{Hi} and D_{Ci} are radiation distribution factors from the hot and cold bounding plates to the fiber layer, respectively, and conversely D_{iH} and D_{iC} are from the fiber layer to the bounding plates. D_{ij} and D_{ji} are radiation distribution factors between different volume elements of the insulating medium.

On the right hand side of Equation 16, the first term represents the radiative heat flux emitted from the hot bounding plate and absorbed by fibers at location i. The second term describes the heat flux emitted by fibers at location i and absorbed by the cold plate. Third and fourth terms describe radiant heat transfer between the different volume elements of fibrous material. (Veiseh and Hakkaki-Fard, 2009)

In the research of Veiseh and Hakkaki-Fard (2009) radiation distribution factors were determined by Monte Carlo Ray Trace method. In this method a three-dimensional model of the fibrous medium was built. Then a large amount of simulated energy bundles were sent from random locations at the surface under

examination, and the location of absorption after a series of scatterings was solved by simulation. Finally, radiation distribution factor was obtained as a ratio between amounts of absorbed energy bundles and total amount of iteration rounds. (Veiseh and Hakkaki-Fard, 2009) Yuen et al. (2003) similarly employed Monte Carlo method in determination of the parameters for their model.

In a two-flux model instead, flux in each direction is modeled with its own equation. After solving for individual fluxes in each direction, the net flux could be obtained as their difference. (Linford et al., 1974; Andersen and Dyrbøl, 1998) Equations 17 and 18 present an example of a simple two-flux model (Linford et al., 1974).

$$\frac{dq_{r,1}(x)}{dx} = -Mq_{r,1}(x) + Nq_{r,2}(x) + P\sigma[T(x)]^4 \quad (17)$$

$$-\frac{dq_{r,2}(x)}{dx} = -Mq_{r,2}(x) + Nq_{r,1}(x) + P\sigma[T(x)]^4 \quad (18)$$

where $q_{r,1}$ is radiative heat flux directed from the hot to the cold side. The flux $q_{r,2}$ is directed into the opposing direction. N is the back-scattering coefficient, P is the absorption coefficient and $M = N + P$ is the extinction coefficient.

These coefficients could be determined experimentally by infrared transmission measurements. As transmittance is dependent from these coefficients, they could be solved by fitting the mathematical expression of transmittance to experimental data. (Linford et al., 1974) Andersen and Dyrbøl (1998) in turn solved adsorption and scattering efficiencies in their two-flux model by employing a computer code, which was not specified in more detail.

A simpler way to include radiative heat transfer into a model would be to calculate its contribution to effective thermal conductivity (Futschik and Witte, 1993; Karamanos et al., 2004; Zhao et al., 2012; Modest, 2013; Grinchuk, 2014). Equation 19 determines the magnitude of the radiative component of thermal conductivity (Zhao et al., 2012; Modest, 2013; Grinchuk, 2014).

$$k_{rad} = \frac{16n^2\sigma T^3}{3\beta} \quad (19)$$

where β is the Rosseland mean extinction coefficient and n is the refractive index. From here on it is simply referred to as extinction coefficient. Refractive index of stone wool fibers lies in the region of from 1.6 to 1.8 (Jørgensen et al., 1994; Williams et al., 2004). In this work however a lower value of 1.2 was found out to result into the best correspondence with the experimental data.

By definition, the Rosseland mean extinction coefficient is determined according to Equation 20 (Zhao et al., 2012).

$$\beta = \left[\int_0^\infty \frac{1}{\beta_\lambda} \cdot \frac{\partial E_{b\lambda}}{\partial E_b} d\lambda\right]^{-1} = \left\{\int_0^\infty \frac{1}{\beta_\lambda} \cdot \frac{2\pi h^2 c^3 \exp\left(\frac{hc}{k_B T\lambda}\right)}{4k_B \sigma \lambda^6 T^5 \left[\exp\left(\frac{hc}{k_B T\lambda}\right)-1\right]^2} d\lambda\right\}^{-1} \quad (20)$$

where β_λ is a wavelength-specific spectral extinction coefficient, $E_{b\lambda}$ is the spectral blackbody emissive power from Planck's law, E_b is the blackbody emissive power, λ is wavelength, $h = 6.626176 \cdot 10^{-34}$ Js is the Planck's constant, $c = 299792458\ \frac{\mathrm{m}}{\mathrm{s}}$ is the speed of light and $k_B = 1.380662 \cdot 10^{-23}\ \frac{\mathrm{J}}{\mathrm{K}}$ is the Boltzmann constant.

In this thesis a simpler method is used. Extinction coefficient could be also determined by Equation 21 (Karamanos et al., 2004).

$$\beta = \rho e \quad (21)$$

where ρ is material density and e is the specific extinction coefficient. In this thesis, the specific extinction coefficient is determined according to an empirical correlation discussed further in this work in Subsection 3.7.10.

3 Materials and experimental methods

This chapter presents firstly the wool types studied in this this thesis. Afterwards it discusses the experimental procedures utilized in this work. These procedures are thermogravimetric analysis and differential scanning calorimetry, which are employed to determine kinetic parameters of different reactions occurring inside wool under fire conditions. Finally, the chapter presents correlations from literature for different material properties and convection.

3.1 Wool types

Variety of different stone wool types and their experimental fire resistance test results are studied in the validation process of the simulation model built in this thesis. Wool slab structural parameters studied in this work are the slab thickness, wool density, loss on ignition (LOI), oil content, fiber content, fiber mean thickness and fiber mean angle of orientation. LOI is determined as a relative mass loss of wool under heating in high temperatures. One should remember that in any part of this thesis LOI does not refer to limiting oxygen index, for which LOI is an established abbreviation in the field of fire safety engineering. The studied set of wools is chosen so that sufficiently different wools with respect to each parameter would be represented to examine reliably their effect on behavior of wool under fire circumstances. Table 1 lists every wool studied in this work along with aforementioned structural parameters. Each wool is assigned with a specific number with which the wool is referred to later on in the work, for example “wool 2”. Slab thickness is from the small scale fire tests. Wools 25 and 27 are tested also in large scale fire tests. The slab thickness was 70 mm in the large scale tests studied in this work. Highlighted fiber angles are either not yet measured or the measurement was erroneous. In these cases, the table shows a guessed angle of orientation used in calculations.

Table 1. Different stone wools included in this work.

Wool no.	Slab thickness (mm)	Wool density (kg/m^3)	LOI (%)	Oil content (%)	Fiber content (%)	Fiber mean thickness (µm)	Fiber mean angle (°)
1	61.9	101.4	1.5	0.08	63.2	4.7	3.6
2	62.4	100.5	1.3	0.2	61.8	5.1	14.8
3	60.0	97.2	1.4	0.09	60.1	4.6	19.3
4	63.2	95.3	1.2	0.13	59.2	4.4	41.7
5	61.7	100.7	1.2	0.15	61.1	4.6	46.4
6	60.5	100.2	1.1	0.15	57.5	4.9	17.2
7	60.0	99.6	1.1	0.19	62.0	3.7	29.9
8	61.8	90.2	1.3	0.25	66.5	3.3	6.5
9	61.1	69.8	1.3	0.32	62.2	3.3	6.5
10	61.7	79.3	1.5	0.46	61.4	3.4	6.5
11	60.1	90.3	1.3	0.11	56.1	4.0	4.9
12	60.1	90.3	1.4	0.13	61.5	3.9	4.2
13	61.4	100.0	1.4	0.11	62.0	4.4	4.3
14	60.3	100.9	1.5	0.11	61.3	3.7	5.1
15	61.0	138.8	2.1	0.11	64.6	3.8	1.5
16	41.2	107.2	1.3	0.11	63.7	3.8	3.0
17	72.7	78.9	1.6	0.27	65.7	3.3	6.5
18	61.3	141.2	1.9	0.09	59.7	3.4	1.3
19	61.9	147.7	1.5	0.18	59.0	5.3	1.9
20	52.0	38.3	0.7	0.08	62.2	4.7	0.8
21	60.5	147.3	1.3	0.13	56.4	3.2	1.5
22	75.7	66.3	6.9	0.29	61.5	4.0	2.4
23	75.2	71.1	9.0	0.27	62.0	4.1	1.9
24	76.2	51.4	9.8	0.21	64.7	4.4	1.0
25	71.5	63.9	1.1	0.02	58.1	4.3	2.9
26	72.8	75.1	1.2	0.01	57.5	4.6	2.9
27	60.4	85.0	1.3	0.02	61.5	4.0	3.8
28	75.0	68.5	4.7	0.26	61.1	4.3	1.1
29	75.7	48.7	6.7	0.24	61.6	4.0	1.5
30	75.3	48.2	4.8	0.15	63.1	4.5	3.95
Maximum	76.2	147.7	9.8	0.46	66.5	5.3	46.4
Minimum	41.2	38.3	0.7	0.01	56.1	3.2	0.8
Average	64.3	89.8	2.5	0.16	61.3	4.1	8.4
			1.3	When excluding high-binder wools 22-24 and 28-30.			

3.2 Cellulosic fire curve ISO 834-1

As a rough categorization, fully developed compartment fires may be divided into two categories of cellulosic and hydrocarbon fires. In cellulosic fires wood, paper, fabrics and such act as a fuel, while in hydrocarbon fires fuels include for example

gas and petrochemicals. Temperature developments in these two fire types vary greatly, hydrocarbon fires being much quicker. Therefore, in fire test situations they are reproduced with different standard temperature curves. The purpose of standardized fire temperature curves is to provide systematic means for easily reproducible fire tests in different laboratories worldwide. (Das, 2014)

The experimental data for the validation process is obtained when the hot side of the stone wool slab is heated up in a furnace according to temperature curve described by the standard ISO 834-1. Meanwhile temperature on the opposing cold side is measured by thermocouples. The standard ISO 834-1, known also as EN 1363-1, describes a ventilation controlled cellulosic fire, i.e. the type of fire expected to occur in a normal building. Equation 22 describes temperature as a function of time according to this standard. (Das, 2014)

$$T(t) = T_0 + 345\, log_{10}(8t + 1) \qquad (22)$$

where t is time in minutes and T_0 is the ambient temperature.

Figure 5 presents temperature development defined by the ISO 834-1, along with some other fire curves (Das, 2014). ISO 834-1 requires that furnace temperature reaches 739 °C in 15 minutes, 842 °C in 30 minutes, 945 °C in 60 minutes and 1049 °C in 120 minutes. The standard defines also the maximum tolerable pressure gradient along the furnace height. (Danish Institute of Fire and Security Technology)

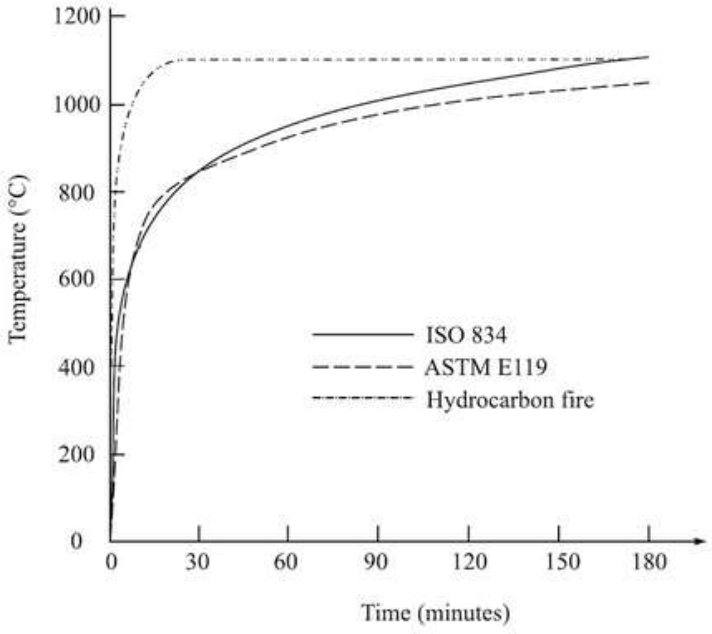

Figure 5. ISO 834-1 and some other standard fire curves (Das, 2014).

3.3 Set-up of fire resistance experiments

Experimental research on heat transfer in actual wool slabs is carried out in furnace experiments. In these experiments, a furnace set to reproduce the standard fire curve ISO 834-1 acts as a heat source.

In the small scale fire tests the examined 60 · 60 cm wool slab is separated from the combustion chamber of the furnace by a thin metal sheet, and is attached tightly into it. The sheet is typically one millimeter thick. Heat transfers through the wool slab and is subsequently released into ambient conditions. Temperature on the cold side is observed by several K-type thermocouples with wire thicknesses of 2 · 0.81 mm. Installation of thermocouples on the cold side complies with the standard SFS-EN 1363-1 (Finnish Standards Association, 2000). The measuring ends of thermocouples are covered with 30 · 30 · 2 mm inorganic insulating pads. The pad and thermocouple are attached tightly into the slab either by heat-resistant glue or by clips held in place by pins, as is the case in Figure 7. If glue is used, none should end up between the measuring end of thermocouple and wool or pad.

Furnace temperature is being observed as well. However, during the first minutes of experiment the actual furnace temperature lags behind the value defined in the standard ISO 834-1. Figure 6 shows this by comparing three temperature time series measured inside the furnace (Furnace 1-3) against the standard during first ten minutes of an experiment. The figure shows also that after this initial period, furnace temperatures follow the standard with a good precision. Figure 7 presents the experimental set-up where the wool slab lies attached to the small-scale furnace and thermocouples are intact. An overview of the set-up is shown left in the figure whereas a close-up of the wool slab surface is presented on the right. On both pictures the steel sheet separating the furnace opening and the wool slab is visible.

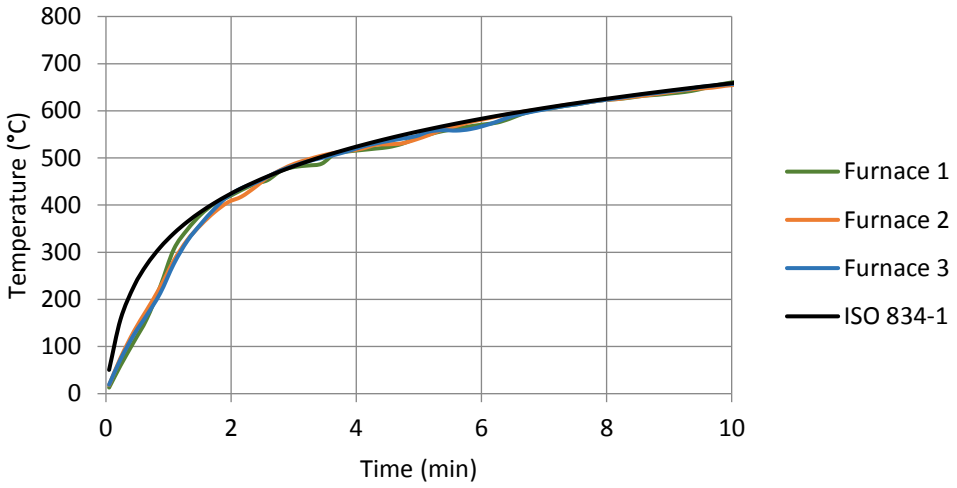

Figure 6. Measured temperature time series inside the furnace compared against the ISO 834-1 standard fire curve.

Figure 7. On left, overview of the small scale furnace test set-up; on right, a close-up of an attached wool slab.

On the contrary to the small scale furnace, the large scale one is controlled with plate thermoelements which measure temperature just next to the surface of the steel sheet. In principle, this gives a better reproducibility and comparability between results from different furnaces.

The size of the furnace combustion chamber opening is 3 · 3 meters in the large scale fire test set-up. A 4.5 mm thick steel sheet lies attached to a counterpiece equally sized with the furnace opening. Wool slab pieces are installed on the cold side of the sheet, held in place by vertical steel profiles repeating every 60 cm and spot welded nails. A total of 11 thermocouples are installed on the cold side. Five of them are attached in the middle of individual slab pieces and the rest on the contact points between the pieces or above the steel profiles. Readings only from the five thermocouples in the middle of the slab pieces are considered when calculating the average cold side temperature.

Figure 8 presents a large scale furnace. On left, the furnace is closed, the installed wool slab is facing into ambient conditions and thermocouples are being installed. In the middle, the furnace is just opened after the completion of a fire test. Plate thermoelements extending from the back of the furnace are visible. When the furnace is assembled, plate thermoelements are in a close contact with the steel sheet. On right is pictured the detached counterpiece just after the completion of a test, where the steel sheet is glowing red.

Figure 8. On left, wool slabs attached to an assembled furnace; in the middle, fireplace of the furnace; on right, the counterpiece with the metal sheet.

3.4 Thermogravimetry

Thermogravimetry (TG) is a thermal analysis method, in which the change of a sample mass is observed as a function of temperature or time. In most applications temperature is increased by a constant rate of 5 – 20 K/min. (Warrington and Höhne, 2008) Figure 9 presents a generic example of TG curve. In this figure, the output of TG analysis include the relative mass of the sample and its decomposition rate as a function of temperature. (McGrattan et al., 2016, pp. 80-84)

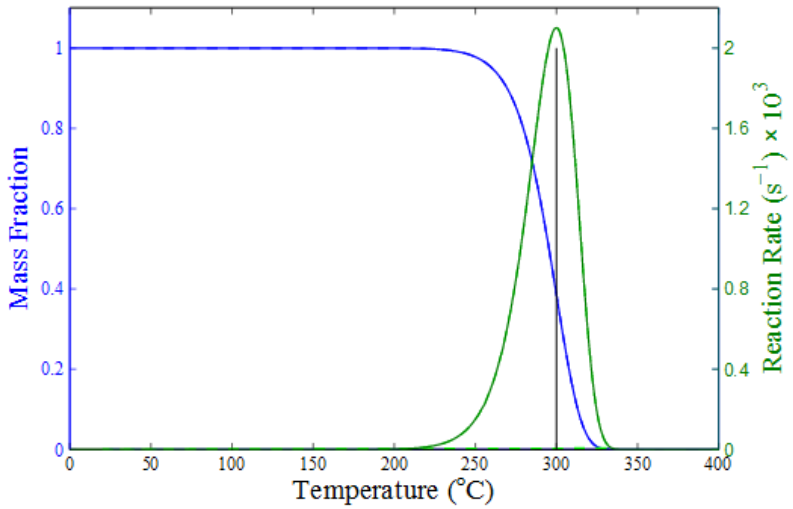

Figure 9. Mass fraction and reaction rate as a function of temperature from thermogravimetric analysis results (McGrattan et al., 2016, pp. 80-84).

Lyon et al. (2011) have presented a method for determining Arrhenius equation parameters for thermally decomposing compounds from thermogravimetric data. Equation 23 presents the Arrhenius equation.

$$r = \left(\frac{\rho_{s,i}}{\rho_s(0)}\right) A_i e^{-\frac{E_{a,i}}{RT}} \tag{23}$$

where r is the reaction rate, $\rho_{s,i}$ is the density of component i inside the material layer, $\rho_s(0)$ is the initial density of the material layer, A is pre-exponential factor, E_a is reaction activation energy, $R = 8.31441\ \frac{\mathrm{J}}{\mathrm{K{\cdot}mol}}$ is the universal gas constant and T is absolute temperature.

In a TG analysis curve the temperature where the reaction rate is at highest is the reference temperature T_p. The corresponding reaction rate is the reference rate r_p. Figure 9 marks this location with a black vertical line. Equations 24 and 25 present the method for calculation of the Arrhenius equation parameters, taking use of the

aforementioned reference values (McGrattan et al., 2010; Lyon et al., 2011; McGrattan et al., 2016, pp. 80-84). This method applies for first-order reactions (Lyon et al., 2011).

$$E_a \approx \frac{RT_p^2}{\beta}\frac{er_p}{x_0} \quad (24)$$

$$A \approx \frac{er_p}{x_0} e^{\frac{E_a}{RT_p}} \quad (25)$$

where β is the heating rate and x is the mass fraction of analyzed component in the whole system. Subscript 0 indicates the initial state. If the system consists only of one component, then $x_0 = 1$.

The ratio of r_p and x_0 could be estimated by Equation 26 with the pyrolysis range ΔT. In Figure 9, the pyrolysis range is the width of the base of the reaction rate curve. The method assumes the rate curve to be roughly triangular. Equation 26 could be substituted into Equations 24 and 25. (McGrattan et al., 2016, pp. 80-84)

$$\frac{r_p}{x_0} = \frac{2\beta}{\Delta T}(1 - \nu_s) \quad (26)$$

where ν_s is the yield of solid residue as a mass fraction from the initial amount of the analyzed component.

3.5 Differential scanning calorimetry and differential thermal analysis

Differential scanning calorimetry (DSC) is a thermal analysis method which measures heat flows to and from a sample under heating. Measurement is based on comparing temperature of the sample to an inert reference material, usually alumina. Among various other applications, quantities relevant for this work measurable by DSC include the heat of reaction. (Warrington and Höhne, 2008)

Based on DSC –analysis data, specific heat capacity c_p could be calculated based on momentary heat flow according to Equation 27 (Mettler Toledo, 2010). Integral over a peak denoting a reaction in DSC-thermogram yields the heat of reaction ΔH_r, according either to Equation 28 or 29, depending on the DSC output format used. Area corresponding to the heat of reaction is measured from the baseline determined by the initial state of the graph.

$$c_p = \frac{\dot{Q}}{m\beta} \quad (27)$$

$$\Delta H_r = \int_{T_1}^{T_2} c_p(T) - c_{p,0}\, dT \quad (28)$$

$$\Delta H_r = \int_{t_1}^{t_2} \frac{\dot{Q}(t) - \dot{Q}_0}{m}\, dt \quad (29)$$

where $\dot{Q}$ is the heat flow into the sample, m is the sample mass, β is the heating rate, and T_1 or t_1 and T_2 or t_2 are temperature or time in the beginning and the end of the DSC peak, respectively. Subscript zero stands for the baseline level. The heat flow is negative if reaction is exothermic.

Differential thermal analysis (DTA) is an analysis method where temperature of a sample is compared against an inert reference sample with well-known thermal properties. Reference material is commonly alumina. Similarly to DSC, DTA can recognize exo-, and endothermic reactions based on the temperature difference between the sample and a reference. (Warrington and Höhne, 2008)

Herein, differential thermal analysis is applied to determine kinetics for solid fiber material reactions according to the Kissinger method (Kissinger, 1957). In this method the DTA experiment is carried out with multiple differing heating rates. Each experiment yields the reference temperature T_p as the location of the maximum temperature difference with respect to the reference sample. At T_p Equation 30 holds. (Kissinger, 1957)

$$\frac{E_a \beta}{R T_p^2} = A N_S X_p^{N_S - 1} e^{-\frac{E_a}{R T_p}} \quad (30)$$

where definitions set for variables at Section 3.4 apply. Here X_p refers to relative amount of unconverted matter at the moment of T_p and N_S is the reaction order.

Thermogravimetric data to determine the value of X_p is not necessary, since the so-called Kissinger approximation allows to assume that $N_S X_p^{N_S - 1} \approx 1$. Independently of the heating rate, the expression is always very nearly equal to unity. Therefore, Equation 30 yields Equation 31. Further, by taking natural logarithms, one obtains Equation 32.

$$\frac{E_a \beta}{R T_p^2} = A e^{-\frac{E_a}{R T_p}} \quad (31)$$

$$ln \frac{\beta}{T_p^2} = ln \frac{AR}{E_a} - \frac{E_a}{R T_p} \quad (32)$$

Therefore, when from several experiments $\ln\frac{\beta}{T_p^2}$ is plotted against $\frac{1}{T_p}$, the obtained slope is equal to $\frac{E_a}{R}$. Now when the activation energy is known, A could be determined from the constant term of Equation 32. (Kissinger, 1957)

Reaction order could be estimated from the shape of a DTA peak. Firstly, the shape index S is determined according to Figure 10. (Kissinger, 1957)

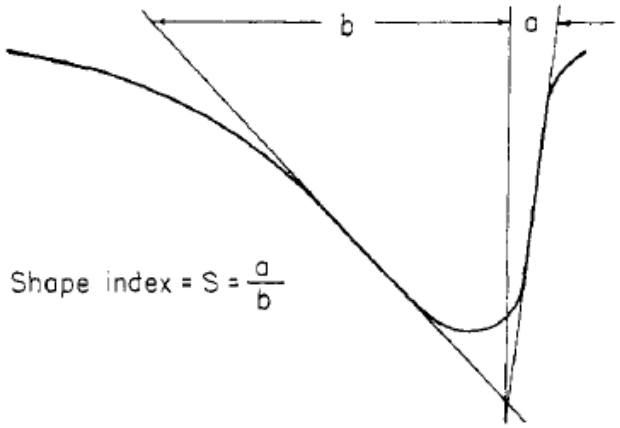

Figure 10. Determination of the shape index S from a DTA peak. Equation 33 gives an estimation of reaction order based on the shape index. (Kissinger, 1957)

$$N_S = 1.26\sqrt{S} \quad (33)$$

3.6 High temperature thermal conductivity of wool

Thermal conductivity of stone wool in high temperatures up to 660 °C is measured according to the standard EN 12667. The standard specifies a guarded hot plate testing apparatus and the testing procedure, and is a so-called absolute technique where a sample is placed between a heat source and a heat sink (Zhao et al., 2016). In this technique the sample is heated with a constant power $\dot{Q}$. After a steady state is achieved, i.e. the temperature difference ΔT between the hot and the cold side reaches a constant value, thermal conductivity k is estimated according to Equation 34 derived from the Fourier's law of heat transfer (Zhao et al., 2016).

$$k = \frac{\dot{Q}x}{A\Delta T} \quad (34)$$

where x is the distance between temperature measurement points and A is the cross sectional area of the measured sample.

To be specific, heat losses from the apparatus should be reduced from the value of $\dot{Q}$, but in a properly insulated set-up they are less than 2 % of the total heat flow. Heat losses by convection and radiation are often minimized by carrying out the measurements under vacuum and radiation shields. Additionally, thermocouples should be thin and made of low-conductivity alloy to avoid conduction of heat by the thermocouples themselves. (Zhao et al., 2016)

Buratti et al. (2014) have used in their research a guarded hot plate apparatus that complies with the standard EN 12667, and described the experimental set-up more in detail. The cold and hot plates were set to specific constant temperatures with the sample placed between them. In their research, the sizes of measured rectangular samples were 300 by 300 mm. As Figure 11 presents, heat flow meters are located in the middle of both plates, otherwise the plate constituting of guarded area. This is in order to ensure the heat transfer to be one-dimensional on the measuring area. (Buratti et al., 2014)

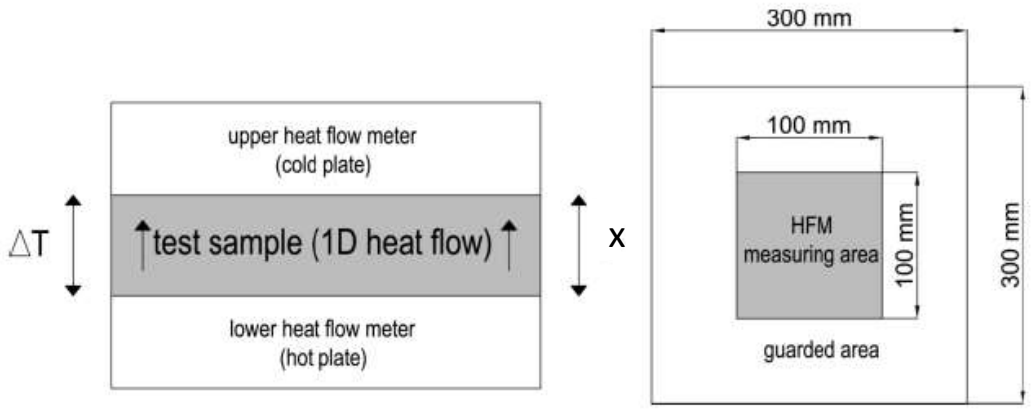

Figure 11. Set-up of a thermal conductivity measurement in accordance with the standard EN 12667. HFM stands for heat flow meter. (Buratti et al., 2014)

3.7 Literature data

Many quantities necessary for this work are well documented and widely found in literature. Properties of air are a good example of a such quantity. Subsections 3.7.1 - 3.7.10 describe which quantities are calculated according to correlations found in literature or found as constants. Modification of some correlations was necessary in order to improve the fit of simulations to experimental results.

3.7.1 Thermal conductivity of air

Thermal conductivity of air k_g is modeled after the correlation presented by Stephan and Laesecke (1985). The correlation is fitted into measurement data from various previous research papers. It is valid over a wide temperature range, from the dew point of air at cryogenic temperature range up to approximately 1200 °C. Equation 35 presents the correlation with its terms rearranged. (Stephan and Laesecke, 1985)

$$k_g = \Lambda\left(C_1 T_R^{-1} + C_2 T_R^{-\frac{2}{3}} + C_3 T_R^{-\frac{1}{3}} + C_4 + C_5 T_R^{\frac{1}{3}} + C_6 T_R^{\frac{2}{3}} + C_7 T_R + C_8 T_R^{\frac{4}{3}} + C_9 T_R^{\frac{5}{3}}\right) \quad (35)$$

where $T_R = T/T_c$ is reduced temperature, the absolute temperature in K divided by critical temperature of air $T_c = 132.52$ K. Equation 36 defines the parameter Λ and Table 2 lists the values of parameters C of the correlation. (Stephan and Laesecke, 1985)

$$\Lambda = \frac{R^{5/6} p_c^{2/3}}{\left(T_c M_a N_A^2\right)^{1/6}} = 4.358 \cdot 10^{-3} \ \frac{\mathrm{W}}{\mathrm{m \cdot K}} \quad (36)$$

where R is the universal gas constant, $p_c = 37.663$ bar is the critical pressure of air, $M_a = 28.97$ g/mol is the molar mass of air and $N_A = 6.022045 \cdot 10^{23} \ \frac{1}{\mathrm{mol}}$ is the Avogadro number.

Table 2. Values of parameters C in Equation 35.

C_1	33.9729025	C_6	607.339582
C_2	-164.702679	C_7	-368.790121
C_3	262.108546	C_8	111.296674
C_4	-21.5346955	C_9	-13.4122465
C_5	-443.445815		

The correlation contains also a part which is dependent on the gas density, but its value is insignificantly small in atmospheric pressure range (Stephan and Laesecke, 1985). It is therefore omitted from the correlation. The obtained value of k_g is substituted into Equations 12 and 13 along with conductivity of solid phase to arrive into the conductive component of thermal conductivity k_{cond}.

3.7.2 Specific heat capacity of air

Fitting a polynomial correlation into data presented by Keskinen (1989) yielded a correlation for specific heat capacity of air as a function of temperature. Figure 12 presents the data points and also the fitted correlation.

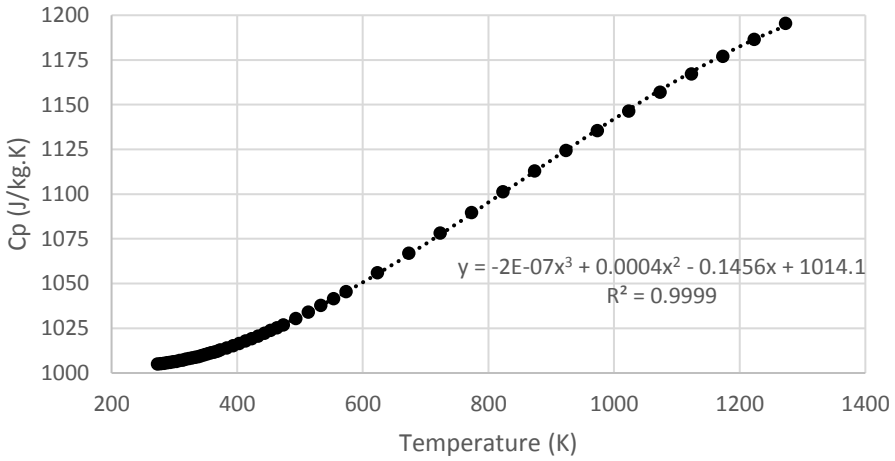

Figure 12. Specific heat capacity of air as a function of temperature according to Keskinen (1989).

As the figure shows, the fit of the polynomial correlation is near-perfect when its degree equals three, coefficient of determination being $R^2 = 0.9999$. Therefore, the fitted correlation presented as Equation 37 defines the specific heat capacity of air $c_{p,g}$ as a function of temperature.

$$c_{p,g} = -2 \cdot 10^{-7} \cdot T^3 + 0.0004T^2 - 0.1456T + 1014.1 \left[\frac{\mathrm{J}}{\mathrm{kg \cdot K}}\right] \quad (37)$$

3.7.3 Thermal conductivity of fiber material

Hofmeister et al. (2016) present in their article thermal property correlations for a variety of glassy and molten lavas. Of the materials investigated in the paper, "Continental basalt" corresponds best to studied stone wools with respect to mineral composition. Table 3 presents the composition of Continental basalt.

Table 3. Composition of Continental basalt in weight percentages (Hofmeister et al., 2016).

SiO_2	TiO_2	Al_2O_3	Fe_2O_3	MgO	CaO	Na_2O	K_2O	MnO	P_2O_5
39.13	2.81	14.9	12.13	4.08	12.18	5.63	5.42	0.29	1.48

Equation 38 presents the correlation for thermal conductivity of glassy Continental basalt (Hofmeister et al., 2016). Obtained conductivity is assumed to be equal to the thermal conductivity of solid phase k_s.

$$k_s = A + BT + CT^{-2} + DT^{1/2} \left[\frac{\mathrm{W}}{\mathrm{m \cdot K}}\right] \quad (38)$$

where T is the absolute temperature and constants A to D are specific correlation parameters for each glass type. For Continental basalt holds $A = 1.9863$, $B = 0.0012735$, $C = 7263.5$ and $D = -0.064536$.

It is worth noting that parameters B and D were given erroneously in the paper, as they were presented there in scientific notation but their exponents were untruthfully positive instead of negative. By applying this correction, computational thermal conductivities as a function of temperature were identical to the ones presented in the article as graphs. (Hofmeister et al., 2016)

3.7.4 Specific heat capacity of fiber material

Hofmeister et al. (2016) offer a correlation also for specific heat capacity of glassy Continental basalt, presented as Equation 39. Similarly, it is assumed to be equal to specific heat capacity of solid fiber material $c_{p,s}$.

$$c_{p,s} = A + BT + CT^{-2} \left[\frac{\mathrm{J}}{\mathrm{kg \cdot K}}\right] \quad (39)$$

where now applies $A = 950$, $B = 0.16$ and $C = -0.135$. T is similarly the absolute temperature.

Figure 13 compares specific heat capacity of solid phase calculated by this correlation to a DSC thermogram. The thermogram presented herein is a result of an analysis of recycled stone wool melt carried out in nitrogen atmosphere. Comparison reaches into 1000 °C, which is approximately the melting point of the wool material.

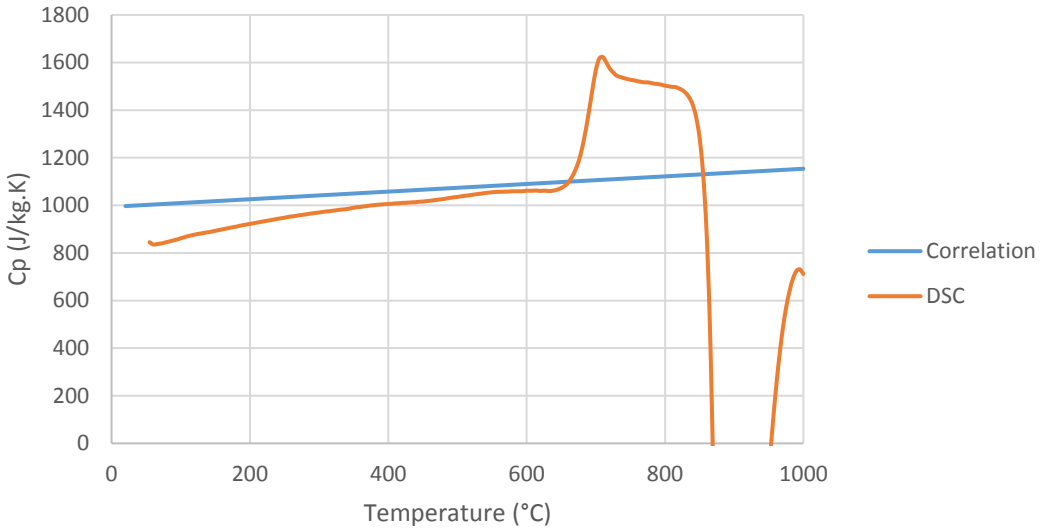

Figure 13. Specific heat capacity of the fiber-forming material as a function of temperature determined either by the correlation (Hofmeister et al. 2016) or by DSC measurements.

The exothermic peak starting at 800 ˚C extends to -5000 $\frac{\mathrm{J}}{\mathrm{kg \cdot K}}$. Figure 13 shows that apart from endo-, and exothermic peaks, correlation follows well the values from the DSC analysis of recycle melt. The correlation is therefore determined to be representative of specific heat capacity of the solid phase of wool.

3.7.5 Effective thermal conductivity of wool

Effective thermal conductivity of wool is a sum of conductive and radiative components, as described in Section 2.4. Effective thermal conductivity calculation is based on Equations 5, 12, 13, 15 and 19. These equations are presented also in here to clarify the method.

$$k_{perp} = \frac{k_g k_s}{\varphi k_s + (1-\varphi)k_g} \quad (12)$$

$$k_{para} = \varphi k_g + (1-\varphi)k_s \quad (13)$$

$$k_{cond} = k_{para}\, sin^2\, \phi + k_{perp}\, cos^2\, \phi \quad (15)$$

$$k_{rad} = \frac{16 n^2 \sigma T^3}{3\beta} \quad (19)$$

$$k_{eff} = k_{cond} + k_{rad} \quad (5)$$

where k is thermal conductivity, subscripts $perp$, g, s, $para$, $cond$, rad, eff standing for in direction perpendicular to fibers, gaseous phase, solid phase, in direction parallel to fibers, conductive component, radiative component and effective value, respectively. φ is porosity, ϕ fiber angle of orientation, n the refractive index and β the Rosseland mean extinction coefficient.

Based on comparison with experimental thermal conductivity data obtained by guarded hot plate method described in Section 3.6 and quality of the fit of simulations, the index of refraction of fibers is set to 1.2. In addition, thermal conductivity in direction parallel to fibers k_{para} is multiplied by 0.7 to improve agreement between simulated and experimental results for wools with high fiber orientation angles. Therefore, Equation 40 substitutes Equation 13.

$$k_{para} = 0.7\left[\varphi k_g + (1-\varphi)k_s\right] \quad (40)$$

Without the modification the model assumes that fibers are infinitely long straight cylinders, which is clearly untrue. Instead, contacts between individual fibers causes a drop in thermal conductivity in direction parallel to fiber orientation compared to this ideal case (Futschik and Witte, 1993; Grinchuk, 2014).

Figure 14 presents measured and calculated thermal conductivities of wools with different densities as a function of temperature. Measured wools are named according to their densities, 70, 100 and 130 kg/m^3, respectively as they are not included in the set of wools studied in this thesis. Wools that correspond best to these, are wools 9, 1 and 15, with densities of 69.8, 101.4 and 138.8 kg/m^3, respectively. From the measured wools, parameters such as fiber content, fiber thickness and fiber orientation are not available, so the conductivity predicted by the model could not be proven to be exact. However, shapes of the computational curves are similar to experimental measurements and the predicted conductivity falls consistently with increasing density. Measurements are carried out by the guarded hot plate method described in Section 3.6.

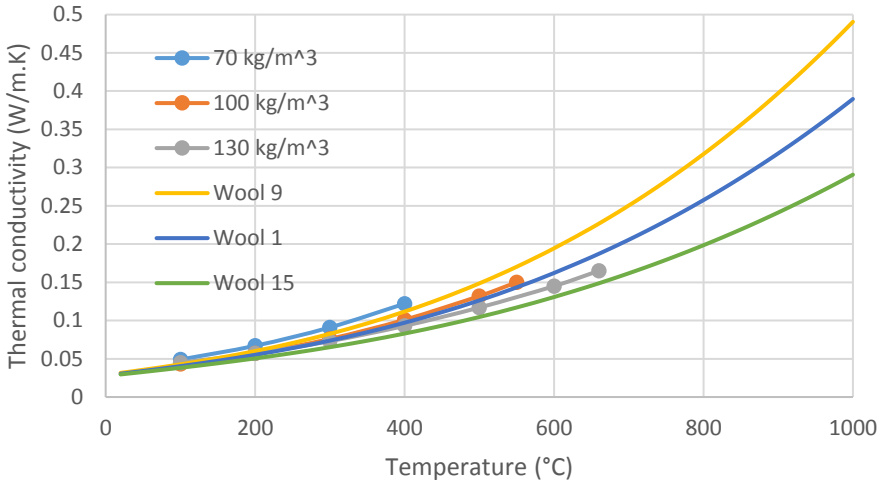

Figure 14. Comparison of measured and calculated thermal conductivities for wools with different densities.

3.7.6 Specific heat capacity of wool

Effective specific heat capacity of stone wool is obtained from specific heat capacities of air and solid phase, weighed by their respective mass fractions in the material. Equation 41 gives the mass fraction of solid phase x_s.

$$x_s = \frac{\rho_s(1-\varphi)}{\rho_s(1-\varphi)+\rho_g\varphi} \tag{41}$$

where ρ_s and ρ_g are densities of solid phase and air, respectively and φ is porosity. Density of air as a function of temperature is determined by fitting a power correlation to data presented by Keskinen (1989). Figure 15 presents the data points and also the fitted correlation.

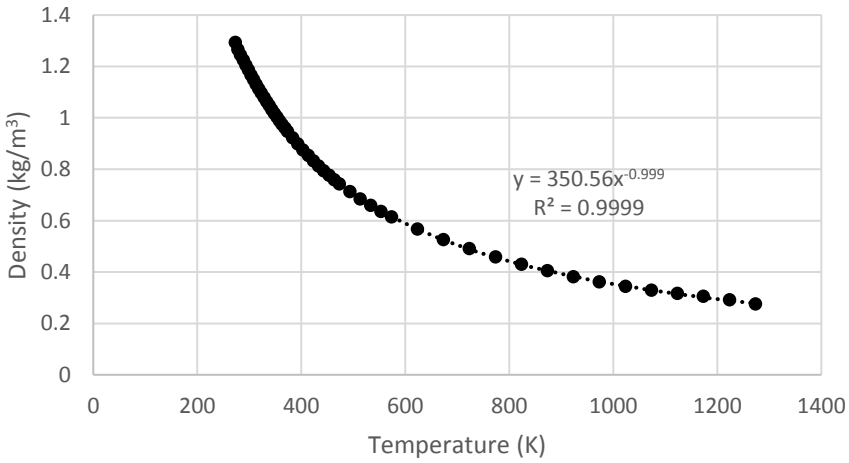

Figure 15. Density of air as a function of temperature according to Keskinen (1989).

Also in this case it is obvious that the fit of the correlation is good since the coefficient of determination is almost equal to unity. Equation 42 presents the fitted correlation to determine the density of air as a function of temperature.

$$\rho_g = 350.56 \cdot T^{-0,999} \ [\mathrm{kg/m^3}] \qquad (42)$$

Finally, Equation 43 gives effective specific heat capacity of stone wool $c_{p,w}$ from respective mass fractions and specific heat capacities of solid fiber material and air.

$$c_{p,w} = x_s c_{p,s} + (1 - x_s) c_{p,g} \qquad (43)$$

3.7.7 Thermal properties of carbon steel

The metal sheet separating the wool slab from furnace is composed of carbon steel. Equation 44 presents a correlation to determine its thermal conductivity k_m as a function of temperature (Franssen and Real, 2010).

$$k_m = 54 - 0.0333T \ \left[\frac{\mathrm{W}}{\mathrm{m \cdot K}}\right] \qquad \text{for } 20\ ℃ \leq T < 800\ ℃ \qquad (44)$$

where T is temperature in °C. At the temperatures between 800 and 1200 °C applies $k_m = 27.3 \ \frac{\mathrm{W}}{\mathrm{m \cdot K}}$.

Set of equations 45 determines the specific heat capacity of steel $c_{p,m}$ as a function of temperature. T is similarly in °C. (Franssen and Real, 2010)

$$c_{p,m} = 425 + 0.773 \cdot T - 1.69 \cdot 10^{-3} T^2 + 2.22 \cdot 10^{-6} T^3 \ \left[\frac{\mathrm{J}}{\mathrm{kg \cdot K}}\right] \qquad (45)$$

$$\text{for } 20\ ℃ \leq T < 600\ ℃$$

$$c_{p,m} = 666 + \frac{13002}{738 - T} \ \left[\frac{\mathrm{J}}{\mathrm{kg \cdot K}}\right] \qquad \text{for } 600\ ℃ \leq T < 735\ ℃$$

$$c_{p,m} = 545 + \frac{17820}{T - 731} \ \left[\frac{\mathrm{J}}{\mathrm{kg \cdot K}}\right] \qquad \text{for } 735\ ℃ \leq T < 900\ ℃$$

$$c_{p,m} = 650 \ \frac{\mathrm{J}}{\mathrm{kg \cdot K}} \qquad \text{for } 900\ ℃ \leq T < 1200\ ℃$$

Nurmi (2016) has used in his work a density of 7850 kg/m^3 for carbon steel. Densities of many different carbon steel grades fall close to this varying around the aforementioned value (Mordfin, 2002). Therefore the density of 7850 kg/m^3 is judged to be applicable in this work as well.

3.7.8 Thermal properties of brick

The insides of a furnace are composed of brickwork, whose thermal mass causes its temperature not to follow the ISO 834-1 temperature curve directly, but with a lag instead. As the furnace walls act as the emissive source within the furnace, its thermal properties need to be taken into account. Specific heat capacity, density and thermal conductivity of fire brick are 829 $\frac{\mathrm{J}}{\mathrm{kg \cdot K}}$, 1790 kg/m^3 and 1 $\frac{\mathrm{W}}{\mathrm{m \cdot K}}$, respectively (American Society of Heating, Refrigerating and Air-Conditioning Engineers, 2013). Specific heat capacity of fire brick stays practically constant over the whole temperature range from ambient to the 1000 °C of fire conditions (Hu et al., 1993). Change of thermal conductivity as a function of temperature needs not to be considered since the furnace is implemented into the model in a simplified manner where conduction through the brick layer is excluded from calculations.

3.7.9 Convective and radiative heat transfer

Heat transferred through the wool slab will eventually be released into ambient conditions on the cold side by convection and radiation. Radiative heat release to ambient is calculated simply by the Stefan-Boltzmann law, and convective heat transfer coefficient is solved by correlation proposed by Drysdale (2011). Convective heat transfer from the cold side of the wool slab is assumed to occur by laminar natural convection. Therefore, Equation 46 gives the convective heat transfer coefficient. (Drysdale, 2011).

$$h = k_g \cdot C(Gr \cdot Pr)^{1/4} \cdot \frac{1}{l} \tag{46}$$

where k_g is thermal conductivity of air as defined by Equation 35, Gr and Pr are Grashof and Prandtl numbers, respectively, and l is the characteristic length scale, here the height of the wool slab, being equal to 0.6 m.

It should be noted that in the original correlation the constant term C is equal to 0.59, but setting C to 0.12 results into better agreement between simulated and experimental results. The justification for this modification is that the initial correlation applies only for free convection (Drysdale, 2011). Figure 7 however

shows that there is a small table right below the wool slab in the test set-up, which acts as an obstruction for convection. Uncertainties related to convection in the test set-up are included into the modified constant, which also allowed for exclusion of the convection length scale from the sensitivity analysis.

Prandtl number, the ratio of momentum diffusivity to thermal diffusivity, is assumed to hold a constant value of $Pr = 0.71$, which applies for dry air at 15 °C (Dixon, 2007). Prandtl number remains almost constant over a wide temperature range, especially if air is dry (Tsilingiris, 2008). Equation 47 defines the Grashof number, the ratio of product of buoyant and inertial forces to the square of viscous forces.

$$Gr = \frac{g l^3 \beta (T_L - T_0)}{\nu^2} \quad (47)$$

where $g = 9.81\ \frac{\mathrm{m}}{\mathrm{s}^2}$ is the gravitational acceleration due to the gravity of Earth, β is thermal expansion coefficient, T_L and T_0 are wool slab cold side and ambient temperatures, respectively and ν is kinematic viscosity of air at at the surface film temperature, which is assumed to be the mean of T_L and T_0.

According to Dixon (2007), thermal expansion coefficient of air is an inverse of absolute temperature T according to Equation 48. Thermal expansion coefficient calculated herein is based on the surface film temperature of the slab.

$$\beta = \frac{1}{T} \quad (48)$$

The kinematic viscosity of air is necessary in the calculation of Grashof number. Correlation to calculate the kinematic viscosity is obtained by fitting a second-degree polynomial correlation to the data presented by Keskinen (1989). Figure 16 presents the data points and the fitted correlation, which is also presented as Equation 49. The figure proves that the fit inside the chosen interval is good, as the coefficient of determination is equal to 1.

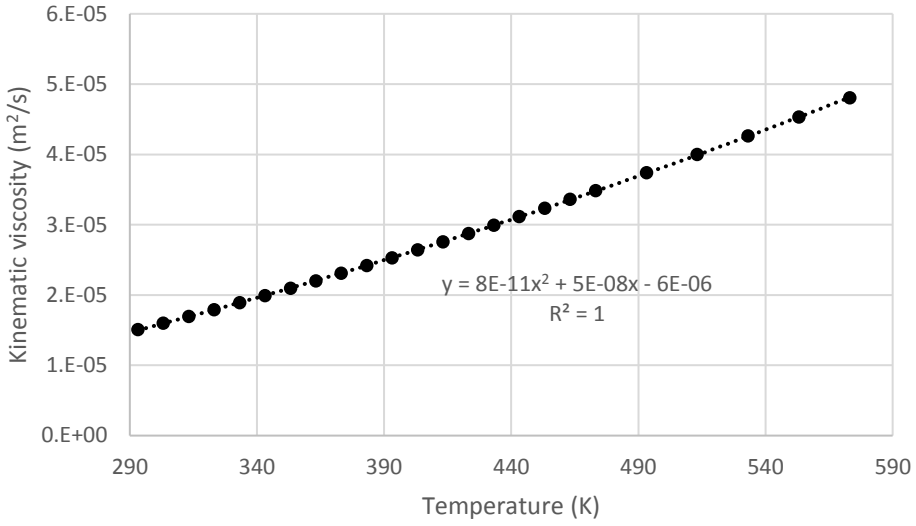

Figure 16. Kinematic viscosity of air as a function of temperature according to Keskinen (1989).

$$\nu = 8 \cdot 10^{-11} T^2 + 5 \cdot 10^{-8} T - 6 \cdot 10^{-6} \ [\mathrm{m^2/s}] \qquad (49)$$

where T is the absolute temperature. In the calculation of Grashof number, the kinematic viscosity of air is based on the surface film temperature.

The regime of fitting for the correlation is chosen conservatively to be from ambient to 300 °C = 573.15 K. Even with the wools with large combustible organic fractions, such as wools 23 and 24, maximum experimental cold surface temperature never exceeds 330 °C, meaning the surface film temperature remains well under 200 °C.

For Equation 46 to be valid, convection needs to be laminar, i.e. $10^4 < Gr \cdot Pr < 10^9$ (Drysdale, 2011). Figure 17 presents the Grashof number as a function of temperature, calculated with the procedure described in this subsection. The figure clearly shows that the Grashof number never exits the laminar regime so Equation 46 could be considered valid for this case.

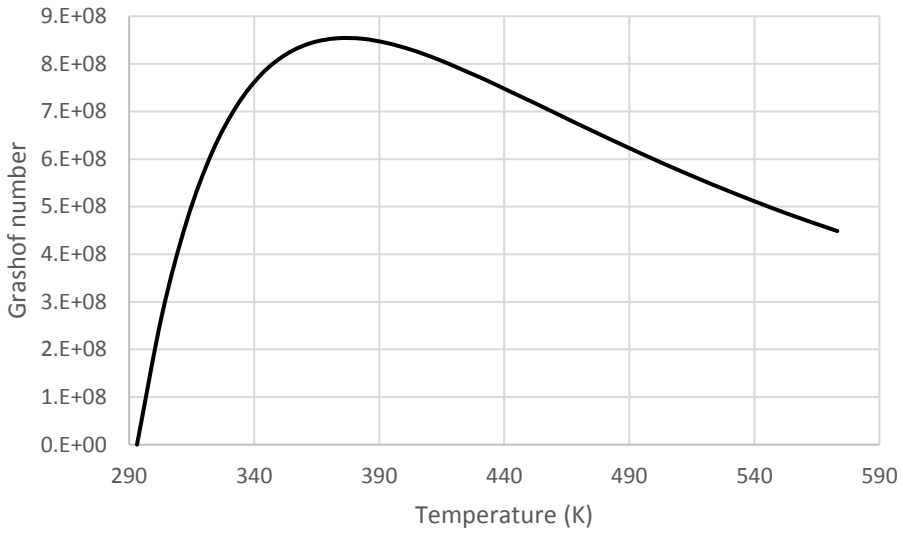

Figure 17. Grashof number on the cold side of the wool slab as a function of temperature.

Estimations on heat transfer properties between the furnace and steel sheet are based on literature values. Convective heat transfer coefficient between the ISO 834-1 curve –following gas phase and furnace walls including the metal sheet was set to 25 $\frac{\mathrm{W}}{\mathrm{m^2K}}$ according to suggestion in Eurocode 1 standard (European Committee for Standardization, 2002). One definitive value was however not available for steel and furnace wall emissivities as both vary depending on the source. In the literature review part of their research paper, Sadiq et al. (2013) reported a range from 0.7 to 0.8 for steel emissivity in fire situations. In the experimental part of their research they suggested a temperature dependency of steel emissivity, the emissivity at high temperatures being 0.69 (Sadiq et al., 2013). In a fire situation steel naturally picks up soot that increases its emissivity. Persaud et al. (1994) estimated the emissivity of a soot-covered steel sheet to be equal to 0.85. Purkiss and Li (2014) suggest emissivity of unity for furnace walls, whereas Staggs and Phylaktou (2008) used a value of 0.7.

3.7.10 Extinction coefficient

The correlation to describe extinction coefficient necessary for calculation of the radiative component of thermal conductivity could not be found from literature. A correlation based on laboratory experiments performed by Partek Oy Ab is used instead. Equation 50 presents the correlation for specific extinction coefficient e.

$Equation\ not\ shown\ here\ as\ non-public\ information.$ (50)

The correlation was modified to return higher values for extinction coefficient. The modification was necessary to counter overpredicted thermal conductivity since the specific extinction coefficient predicted by the original correlation was most likely too low. As the specific extinction coefficient is on mass basis, same specific extinction coefficient on denser wools results into lower radiative thermal conductivity. Therefore, increasing error towards denser wools in final temperature led to suspect issues in the correlation itself. Executed modifications improved significantly the fit of simulations of heavy wools in the order of 140 kg/m^3. Meanwhile, the simulation results of less dense wools remained practically unchanged.

Extinction coefficient β is in turn determined according to Equation 21 as a product of wool density and specific extinction coefficient. However, as practically only fibrous material contributes to extinction of radiation, the equation is modified for the model accordingly. Therefore in the model extinction coefficient is the product of specific extinction coefficient, density of wool excluding combustible organics $\rho_{w\neg o}$ i.e. just inorganic fraction and the fiber fraction ξ. Fiber fraction is the portion of the material of mineral origin that is in fibrous form, instead of shots, the pearl-like residues of the droplets out of whom the fibers were drawn from. Therefore, Equation 51 is used instead in calculation of the extinction coefficient.

$$\beta = e\rho_{w\neg o}\xi \quad (51)$$

4 Numerical methods

This chapter describes first the numerical calculation software tools employed in this thesis. Afterwards, it describes more in detail the numerical integration method employed in processing of numerical data, as well as the numerical approximation of transient heat transfer equation employed in the model.

4.1 MATLAB

MATLAB, standing for Matrix Laboratory, is a computing environment and a programming language aimed at numerical calculation. As the name states, the objective of MATLAB is to make solving of problems involving matrix algebra as simple as possible. (Hahn and Valentine, 2017) As MATLAB is purely numerical calculation software, there are naturally no aids in helping in parameter determination as there are in FDS, as discussed in the next section. Obviously all models describing heat transfer and heat release in chemical reactions should be implemented into MATLAB by their respective numerical approximations. General heat transfer is modeled in MATLAB according to Equation 54 presented in Section 4.4, along with its boundary conditions.

4.2 Fire Dynamics Simulator

Fire Dynamics Simulator (FDS) is an open source fire modeling program, released initially in 2000. Essentially it is a large-eddy simulation computational fluid dynamics simulator to model low Mach number flows related with combustion processes. (McGrattan et al., 2012)

As FDS is a simulator that focuses especially on fire modelling, it has models of varying complexity for combustion reactions. In the most simple case it is enough to just specify the heat release rate per unit area (HRRPUA) and some reaction fuel from FDS material library. As this work is concerned with burning of solid fuels, namely binder matrix and dust binder oil, combustion models for solid fuels are discussed further in here. In the simple pyrolysis model of solid fuels it is enough to give just HRRPUA, ignition temperature and the most essential material properties of density, specific heat capacity and thermal conductivity. The more complex pyrolysis model calculates heat release rates based on Arrhenius equation, presented as Equation 23. When given reference temperature and reference rate from TG data according to Figure 9, or the temperature range during which the mass loss occurs, FDS calculates the Arrhenius parameters according to the

procedure described by Equations 24 and 25 (McGrattan et al., 2010; Lyon et al., 2011). In addition, the complex pyrolysis model requires the same material properties as the simple one. Additionally, heat of modeled reaction is required as an input. Material degradation could be modeled through multiple consecutive reactions and the yield of resulting residual char could also be determined. (McGrattan et al., 2016, pp. 80-84) To obtain as precise model as possible for heat transfer in stone wool, the complex pyrolysis model is chosen to describe decomposition of binder and oil.

Although the main focus of FDS is on the modeling of fire phenomena in gaseous phase, it contains also a heat transfer solver in solid phase (McGrattan et al., 2016, pp. 80-84) that in current version 6.5.3 works in one dimension. The one-dimensional solver works by principle of a finite difference method similar to one built in MATLAB. A three-dimensional heat transfer model for solid phase in FDS is under development phase at the time of writing. FDS is used in parallel with MATLAB to model one-dimensional heat transfer, and obtained results are compared against each other. Two-dimensional heat transfer is modeled exclusively with FDS utilizing its three-dimensional solver, due to inherent complexity associated with the addition of one more spatial dimension.

4.3 Numerical integration

Every numerical integration in this work is carried out by employing the following quadrature rule known as the midpoint rule. Equation 52 presents the midpoint rule in its general form (Pitkäranta, 2005).

$$\int_a^b f(x)\,dx \approx (b-a) f\left(\frac{a+b}{2}\right) \qquad (52)$$

where a and b are the beginning and end points of the (sub)interval over which the function is integrated.

Therefore, in the mid-point rule the value of the integral of a function $f(x)$ within the (sub)interval $[a, b]$ is approximated as the area of a rectangle whose base is $b - a$ and height the arithmetic mean of values of $f(x)$ in the end points of the interval. Numerical integration of some function over a certain range is always carried out by dividing it into multiple subintervals. Therefore, the obtained approximation for the integral over the defined range is the sum of areas of rectangles for all subintervals.

The composite quadrature based on employing the mid-point rule over multiple subintervals in the whole integration range is often the most precise of the Riemann sums approximating an integral (Pitkäranta, 2005). Therefore it is chosen as the numerical integration method in this work. In any case, as experimental data points are densely packed in performed analyses, differences between the midpoint and other methods should be insignificant.

4.4 One-dimensional heat transfer model

One dimensional heat transfer is modeled by incorporating the radiative component of heat transfer into the effective thermal conductivity. The one-dimensional heat transfer model is obtained by differentiation of heat transfer equation presented as Equation 2. Before differentiation, the equation has been multiplied elementwise by thermal diffusivity, which is thermal conductivity divided by the product of density and specific heat capacity. Herein the change of thermal conductivity and specific heat capacity as a function of temperature is taken into account by declaring them in the form of $k_{eff}(T)$ or $c_p(T)$. Equation 53 presents the differentiated equation.

$$\frac{1}{\Delta x}\left[\frac{k_{eff}\left(T_{i+\frac{1}{2}}(t)\right)}{\rho\cdot c_p\left(T_i(t)\right)}\left(\frac{\Delta T(t)}{\Delta x}\right)_{i+\frac{1}{2}} - \frac{k_{eff}\left(T_{i-\frac{1}{2}}(t)\right)}{\rho\cdot c_p\left(T_i(t)\right)}\left(\frac{\Delta T(t)}{\Delta x}\right)_{i-\frac{1}{2}}\right] = \frac{T_i(t+\Delta t)-T_i(t)}{\Delta t} - \frac{\dot{Q}'''(t)}{\rho\cdot c_p\left(T_i(t)\right)} \quad (53)$$

where Δx is mesh size, Δt is time step, ΔT is temperature difference, and subscript i stands for the ordinal number of a mesh grid counting from the hot side. Subscripts $i+\frac{1}{2}$ and $i-\frac{1}{2}$ stand for values at grid cell boundaries.

Temperature after one time step $T_i(t+\Delta t)$ at each location could be calculated by an explicit method obtained by rearranging terms in Equation 53. Equation 54 presents this method.

$$T_i(t+\Delta t) = T_i(t) + \frac{\Delta t}{\Delta x}\left\{\rho c_p\left(T_i(t)\right)\left[k_{eff}\left(T_{i+\frac{1}{2}}(t)\right)\left(\frac{\Delta T(t)}{\Delta x}\right)_{i+\frac{1}{2}} - k_{eff}\left(T_{i-\frac{1}{2}}(t)\right)\left(\frac{\Delta T(t)}{\Delta x}\right)_{i-\frac{1}{2}}\right]\right\} + \frac{\Delta t\dot{Q}'''(t)}{\rho\cdot c_p\left(T_i(t)\right)} \quad (54)$$

Thermal conductivity in previous equations is determined to be its effective value k_{eff}, which is the sum of conductive and radiative components.

Equation 55 describes heat transfer within the separating steel sheet. It is assumed to be a thermally thin object, so temperature profile within it could be considered homogenous. Therefore, Equation 55 is similar to 54, except terms describing receiving and giving off the heat are directly implemented boundary conditions for hot and cold boundaries.

$$T_s(t+\Delta t) = T_s(t) + \frac{\Delta t}{x_{sheet}}\left[\frac{k_s(T_s)}{\rho_{steel}\cdot c_{p,steel}(T_s)}\frac{T_1 - T_s}{\Delta x/2} + \frac{\sigma\left(\varepsilon_F T_F^4 - \varepsilon_{steel} T_s^4\right)}{\rho_{steel}\cdot c_{p,steel}(T_s)} + \frac{h_f(T_G - T_s)}{\rho_{steel}\cdot c_{p,steel}(T_s)}\right] \quad (55)$$

where x_{sheet} is the thickness of the steel sheet, k_s is thermal conductivity of wool in hot surface conditions and h_f is the convective heat transfer coefficient between the hot gas and furnace walls.

Equations 56 and 57 define the boundary conditions on the hot and cold surfaces of the wool slab, respectively.

$$\left(-k_s\frac{\partial T_s}{\partial x}\right)_{x=0} \approx \left(-k_s\frac{\Delta T_s}{\Delta x}\right)_{x=0} = -k_s\frac{T_1 - T_s}{\Delta x/2} \quad (56)$$

$$\left(k_L\frac{\partial T_L}{\partial x}\right)_{x=L} \approx \left(k_L\frac{\Delta T_L}{\Delta x}\right)_{x=L} = h(T_L - T_0) - \varepsilon_w\sigma(T_L^4 - T_0^4) \quad (57)$$

In the past three equations subscripts s and L denotes properties at hot and cold surfaces of the wool slab, respectively. As the metal sheet and the hot surface of the wool slab are attached to each other, temperatures of both are marked as T_s. Subscript 1 stands for the first grid cell representing wool. Subscript F denotes the furnace walls, whose temperature follows the hot gas temperature T_G with a delay. Subscript w stands for wool. h is the convective heat transfer coefficient between the cold side of the wool slab and ambient air, whose temperature is T_0.

In Equation 55 determining the temperature of metal sheet, the first term in the brackets stands for conduction of heat into the wool slab. As heat is carried away by conduction in wool, thermal conductivity of wool at hot surface temperature k_s is used. The second term describes the radiative exchange between furnace walls and the metal sheet, and the third one describes convective heat transfer between hot gases and the metal sheet. T_G follows the temperature development described by ISO 834-1, except a small delay period during the heat-up.

Equation 56 states that the hot side of the wool slab gains energy just by conduction from the metal sheet. In the computational model, the temperature gradient between T_s and T_1 occur over just half of a grid cell's width. Therefore as a denominator is $\Delta x/2$. Equation 57 determines that the heat conducted through wool slab is released into ambient conditions by convection and radiation.

Explicit method is not unconditionally stable. If the time step size is too large, solution diverges into infinity and no sensible results are obtained. Equation 58 presents the stability criterion with respect to dimensionless time τ, or Fourier number. (Cengel, 2003) It is easily seen that if an unstable solution occurs, time step should be reduced to arrive into a stable solution. If a reduction of time step in a sensible extent is not enough, the computational grid should be made sparser.

$$\tau = \alpha \frac{\Delta t}{\Delta x^2} = \frac{k}{\rho c_p} \frac{\Delta t}{\Delta x^2} \leq 0.5 \qquad (58)$$

where α is thermal diffusivity.

A MATLAB model for heat transfer is built according to Equation 54. Thermal conduction model of the Fire Dynamics Simulator works also by the same principle (McGrattan et al., 2016b, pp. 67-76).

4.5 MATLAB model for heat transfer

Annex A discusses in detail how all of the aforementioned numerical methods and material property correlations are implemented into a single, functional simulation model in MATLAB. The MATLAB model consists of a main file in which wool and simulation parameters are defined and plots the resulting data at the end of the simulation. Heat transfer and thermal property calculations are defined separately in their respective functions which are invoked from the main file or other functions. Also, justifications for some fitted parameters are presented.

4.6 FDS model for heat transfer

Annexes B and C representing one-, and two-dimensional models, respectively, describe the structure of the Fire Dynamics Simulator input file, how input parameters are implemented and how desired outputs are obtained. Annex B1 describes the MATLAB script file FDS_ramp.m, whose purpose is to give thermal conductivity and specific heat capacity ramps in numerical form based on wool material parameters. These annexes include the FDS input files for both models.

One main weakness of the one-dimensional FDS model, the impossibility of assigning different heat transfer coefficients on different sides of the slab is discussed more in detail in Annex B2. Existence of such problem is mentioned also in here since this issue is discussed multiple times in Chapters 5 and 6.

5 Results and discussion

The beginning of this chapter presents the experimental data from thermal analyses and its processing. These include kinetic parameters for each reaction and reaction heats for solid phase reactions within the wool fibers. Afterwards simulation results acquired by both MATLAB and FDS are presented and compared with experimental measurements from actual fire tests. The uncertainty of these simulations is estimated as a part of validation process and the need for further research is discussed.

5.1 Thermogravimetry

An initial plan was to determine thermal decomposition kinetics for both cured binder resin and dust binding oil by performing thermogravimetric analyses with heating rates of 5 and 20 °C/min. However, the TGA thermogram of cured resin (Figure 18) shows that it undergoes very complex decomposition reactions with multiple different phases. Figure 19, which shows the first derivative of 5 °C/min resin TGA curve, is a further proof of complex kinetics. Additionally, the maximum temperature and thus the end of TG analysis is reached before the completion of reaction. This behavior was unexpected and is probably rooted in the TGA sample being a monolithic resin chunk of some tens of milligrams, whereas in wool resin is dispersed as tiny droplets. This may have given rise to oxygen mass-transfer limited reactions in the present TGA.

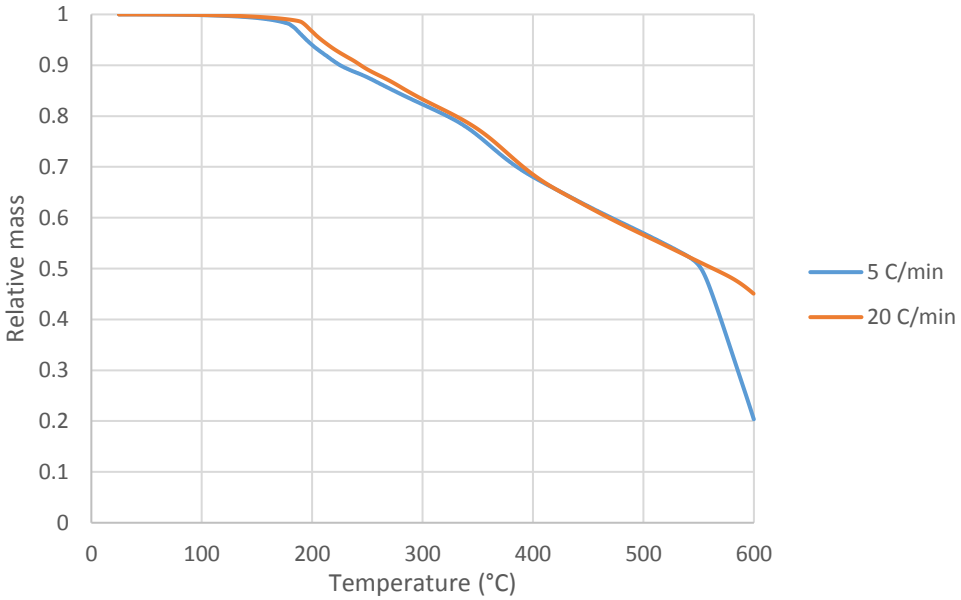

Figure 18. TGA results for cured resin at heating rates of 5 and 20 °C/min.

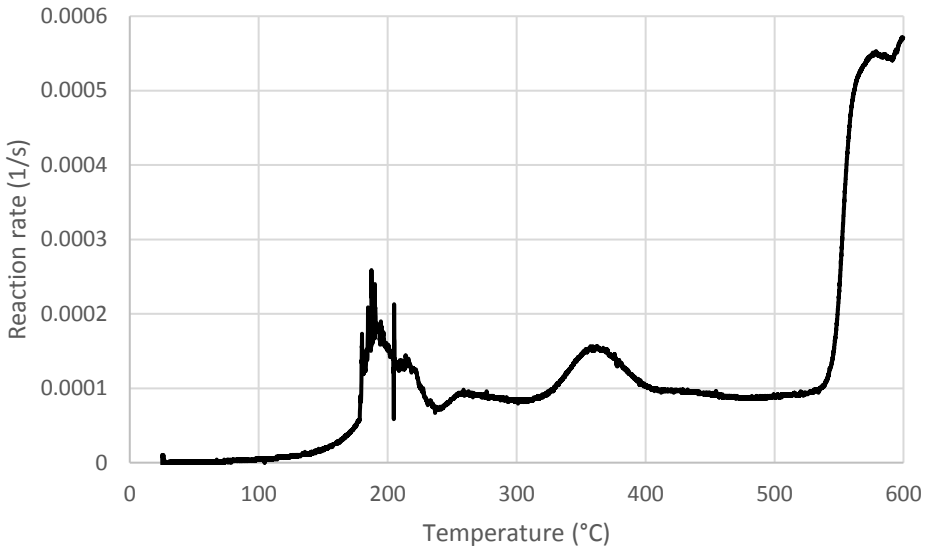

Figure 19. First derivative of cured resin TGA curve at heating rate of 5 °C/min.

TG analyses for oil decomposition were less ambiguous. Analyses are carried out with the same heating rates as for resin. Figure 20 presents the analysis results.

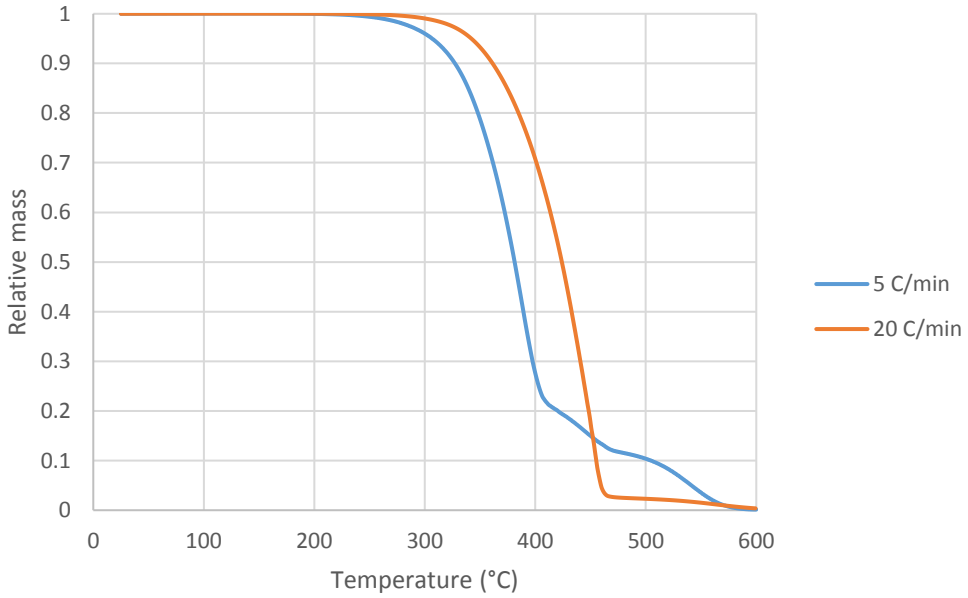

Figure 20. TGA results for oil at heating rates of 5 and 20 °C/min.

As resin TGA results presented herein are of little use, kinetic parameters for resin were defined with the help of an old TG analysis of binder-oil mixture, presented as Figure 21. The figure includes also a DTA curve measured simultaneously. As all

numerical data of the experiment and other information, e.g. heating rate were lost, a reconstruction of the experiment is carried out in Fire Dynamics Simulator. The input file for FDS reconstruction is available in Annex D. During the reconstruction, reference temperature, pyrolysis range and reaction order are iterated so that the best possible correspondence with the TGA curve would be achieved. Since the heating rate during a TGA experiment is instrumental in determination of the kinetic parameters, the rate is solved with the help of oil TGA results presented in Figure 20. By employing the information from the old TGA thermogram and the obtained heating rate, a rudimentary estimation for kinetic parameters of binder decomposition is obtained. The parameters could definitely not be considered precise, especially since the method described by Section 3.4 and employed herein is in principle consistent only for first order reactions.

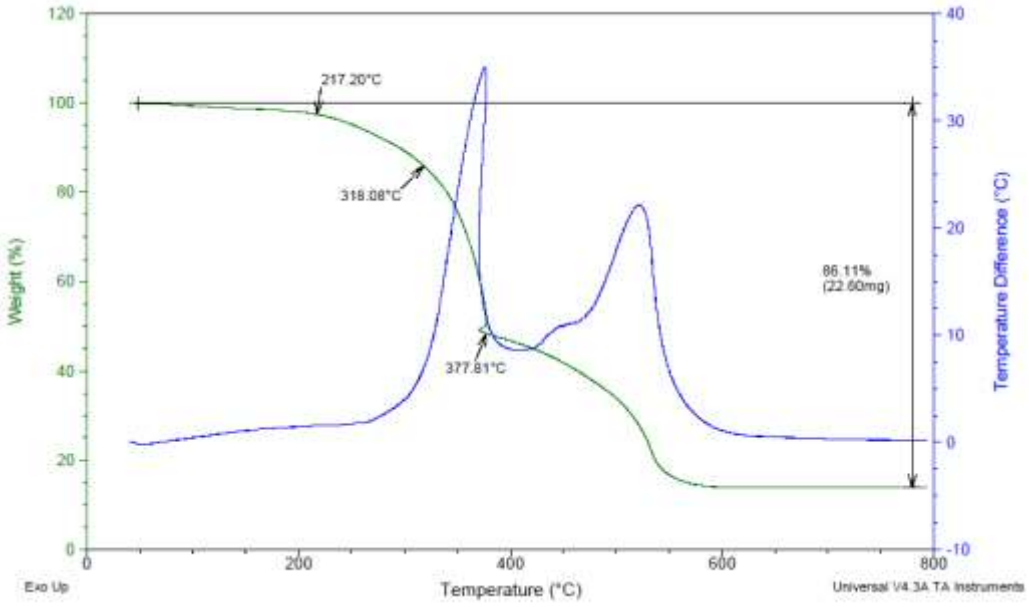

Figure 21. Results of thermogravimetric-, and differential thermal analyses of resin-oil mixture used in determination of resin decomposition kinetics.

The oil TGA results in Figure 20 show that the char yield in oil decomposition is small. For simplicity, it is assumed to be equal to zero, so that resin would be responsible for all of the solid residue produced whose relative amount is visible in Figure 21. Also, as oil mainly reacts before resin, mass fractions were readable from the point where the ending of oil decomposition is visible. Therefore 51 wt-% of the mixture consists of oil and 49 wt-% of resin. As a result 28.35 wt-% of resin ends up as solid residue, denoted as ‘char’ in the FDS input file.

Reconstruction of the TG experiment in FDS begun by inputting some already known parameters such as heats of reaction and those found out by interpreting the TGA-, and DTA curves. These were material mass fractions, reference temperatures and pyrolysis ranges. Initial guesses of reference temperatures were taken from locations of DTA peaks and pyrolysis ranges from regions in TGA curves where mass loss was clearly visible. As both DTA peaks, especially the one for oil, were skewed towards right, initial guesses for reaction orders were below unity. Iteration by hand was carried out by changing these previously mentioned three quantities until satisfactory match between original and simulated graphs was achieved. Figure 22 presents the simulated graph obtained after the iteration overlaid above the measured curve. As a result was obtained $T_p = 370\ ℃ = 643.15$; $\Delta T = 230\ \mathrm{K}$ and $N_S = 0.2$ for oil and $T_p = 525\ ℃ = 798.15$; $\Delta T = 222\ \mathrm{K}$ and $N_S = 0.7$ for resin, respectively. After solving for the heating rate, these reference temperatures and pyrolysis ranges are used in order to determine the activation energy and frequency factor for the decomposition reactions.

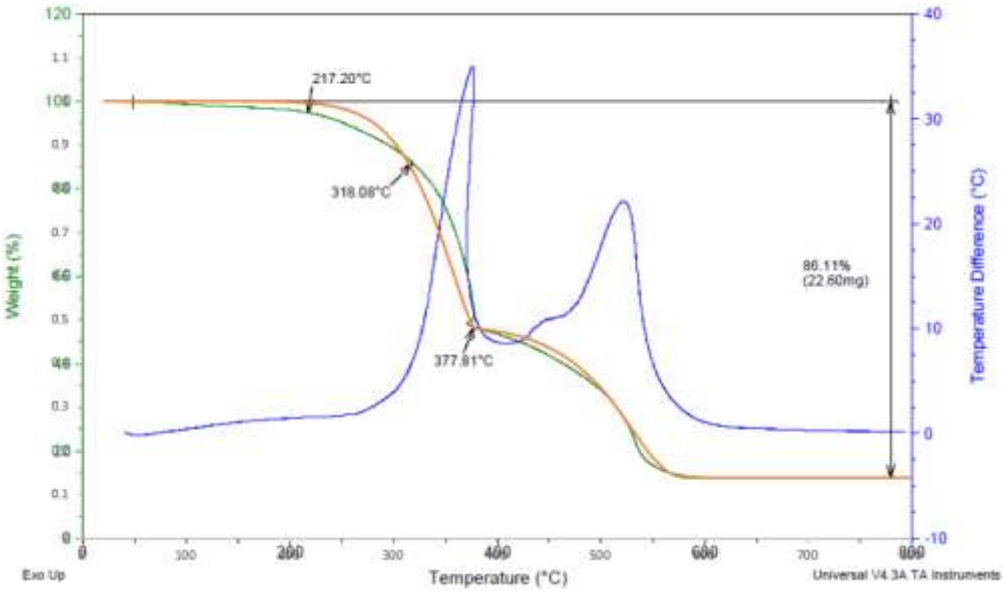

Figure 22. Simulated thermogravimetric experiment compared to original measurement data.

In this phase of reconstruction of the TGA-experiment it is not yet necessary to know the heating rate of the actual experiment. When kinetics are determined by reference temperature and pyrolysis range, the apparent location of the simulated graph is located always in the same position in temperature coordinates irrespective of the heating rate. However, without the heating rate, values of kinetic parameters remain unknown.

To estimate the heating rate in the original resin-oil thermogravimetric analysis, Arrhenius parameters for oil were estimated by the Kissinger method (Kissinger, 1957). Reference temperatures for both experiments are solved from derivatives of the TGA curves presented below in Figure 23.

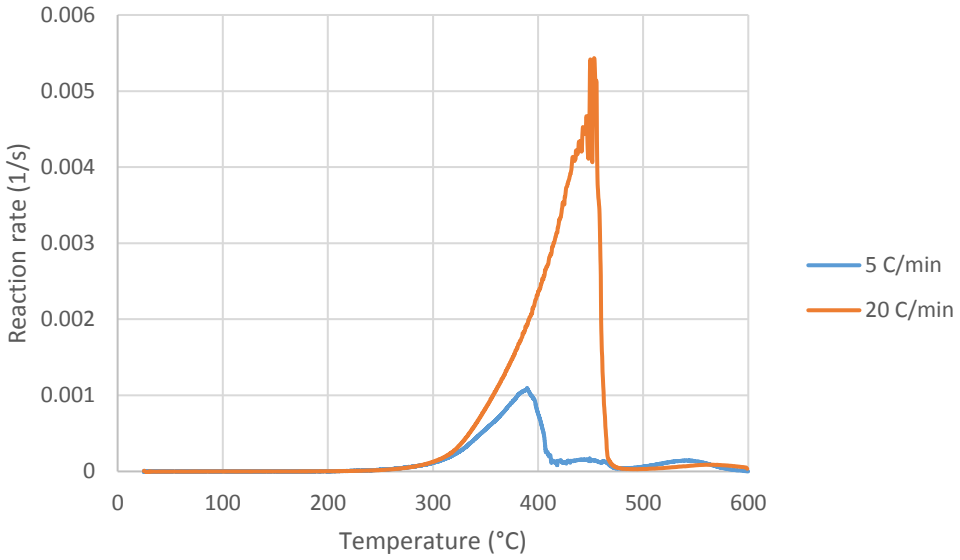

Figure 23. First derivatives of the oil TGA curves.

Figure 23 reveals 390 °C = 663 K and 445 °C = 723 K as reference temperatures for experiments carried out at 5 and 20 °C/min, respectively. Fluctuations in the reaction rate in the 20 °C/min experiment are assumed to be errors so the reference rate was assumed to occur just before them. These results are now linearized according to Equation 32, presented again in here. Figure 24 presents the linearization.

$$ln\frac{\beta}{T_p^2} = ln\frac{AR}{E_a} - \frac{E_a}{RT_p} \quad (32)$$

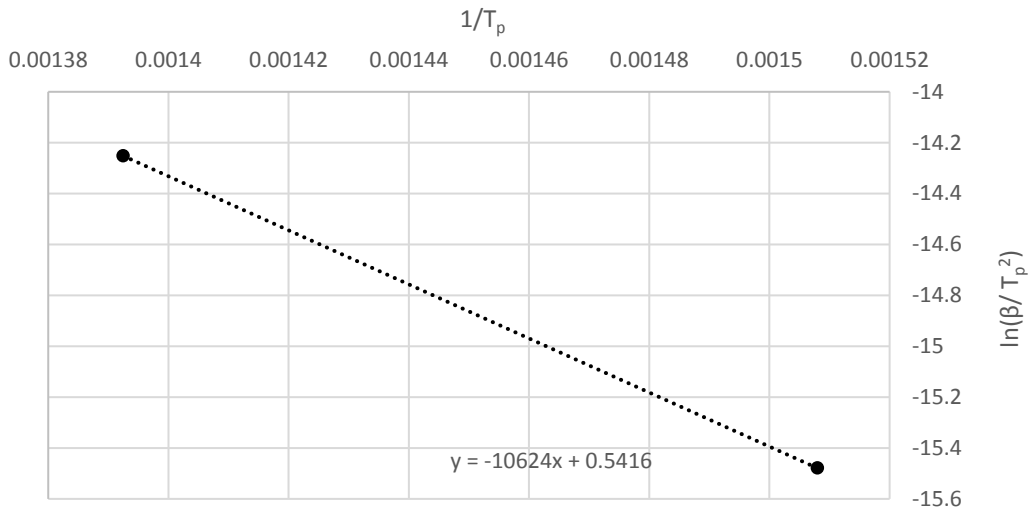

Figure 24. Linearization of oil TGA results according to the Kissinger method.

According to the procedure of Section 3.5, the equation of fitted linearization visible in Figure 24 results into activation energy of $E_a = 88332.3\ \frac{\mathrm{J}}{\mathrm{mol}}$ and frequency factor of $A = 18260.0\ \frac{1}{\mathrm{s}}$. Rearrangement of Equation 31 or 32 yields Equation 59.

$$\beta = \frac{RT_p^2 A e^{-\frac{E_a}{RT_p}}}{E_a} \tag{59}$$

By substituting kinetic parameters obtained above and the iterated reference temperature of 370 °C = 643.15 K for oil, heating rate in the original experiment is solved to be $\beta = 0.047628 \ldots \frac{℃}{\mathrm{s}} = 2.85766 \ldots \frac{℃}{\mathrm{min}} \approx 3\ \frac{℃}{\mathrm{min}}$. Figure 25 presents both experimental oil TGA curves compared to simulations in MATLAB and FDS with the heating rate of 3 °C/min. In both simulations the same kinetic parameters based on reference temperature, pyrolysis range and the previously obtained heating rate were used. In light of this the obtained heating rate seems reasonable as generally TGA curves move from left to right as heating rate is increased.

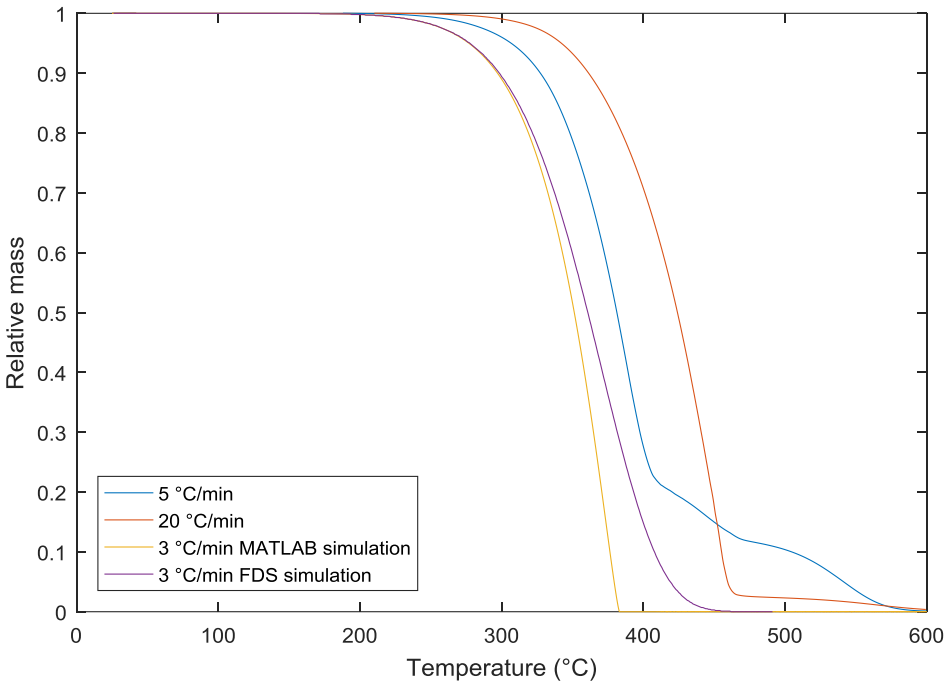

Figure 25. Simulated oil TGA curves compared against experimental ones.

Simulations in both MATLAB and FDS look similar, except closer to the end of the reaction its rate is higher in the MATLAB model than in FDS. Since kinetic parameters are adjusted separately for both models, the effect of this behavior is assumed to be insignificant. Because the difference increases as oil is consumed in decomposition, the reason might be differences between the models in the kinetic term, which includes the amount of available reactant.

Now after obtaining the heating rate of the original resin-oil TGA experiment, it is possible to calculate Arrhenius parameters also for resin. From here on, Arrhenius parameters for oil are based on 5 °C/min TGA, since it is judged to be the most reliable source. Table 4 presents the kinetic parameters solved according to Equations 24 and 25. These parameters could however not be considered precise, since there is a lot of uncertainty in the available data. Precise mass fractions of resin and oil could not be known and it is highly possible that some of the binder reacts simultaneously with oil. In addition, the method employed to determine the kinetic parameters is consistent only for first-order reactions. The obtained kinetic parameters should therefore be considered instead as a starting point for iteration in fitting of the kinetic parameters to reproduce the experimental data.

Table 4. Kinetic parameters for resin and oil decomposition based on thermogravimetric data, along with previously known heats of reaction.

	E_a (J/mol)	A (1/s)	N_S	ΔH_r (MJ/kg)
Resin	93002.8	1071.14	0.7	-25
Oil	99391.6	152697	0.2	-45

5.2 Differential scanning calorimetry and differential thermal analysis

Necessary but lacking model input parameters are the heats of reaction for fiber solid phase reactions, such as crystallization of fiber material and oxidation of various metals in fibers to their respective higher oxides. These heats of reaction are solved from differential scanning calorimetry (DSC) data of inorganic fraction of wool 1. The measurement is carried out in air with a heating rate of 15 °C/min. In the analysis data presented as Figure 26 exothermic peaks at the temperature ranges of 710-850 °C and 850-960 °C are visible. Here the thermogram presents heat flow from the sample, so exothermic reactions are in the positive direction unlike described in Section 3.5. Heats of reaction are calculated by numerical integration over their respective peaks in DSC-thermogram.

However, solid phase reactions of the wool material were necessary to be disabled from the model in order to avoid excessive heat release. It was noticed that the binder degradation alone is enough to reproduce the rapid heat rise observed in experiments. Therefore, solid phase reactions were chosen to be left out of the model due to uncertainties in the measurement data.

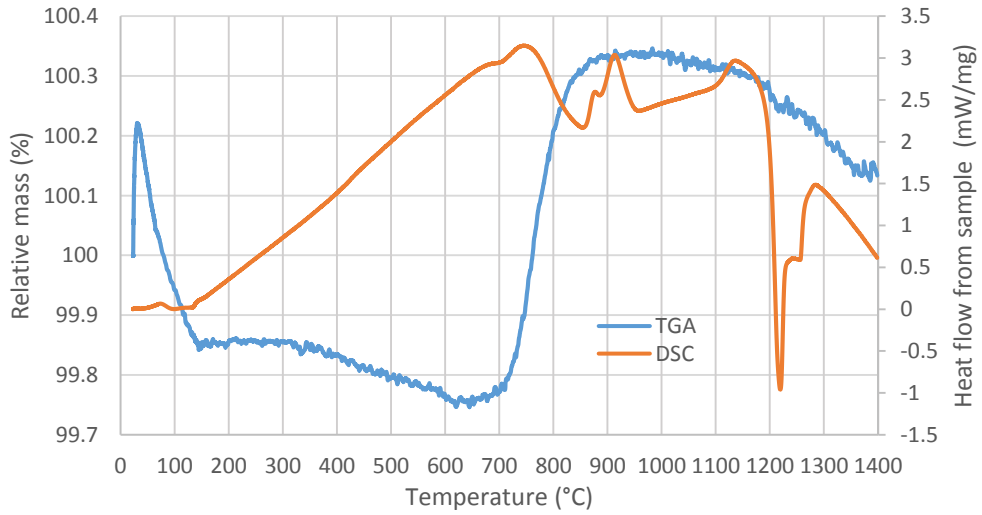

Figure 26. DSC measurement result of wool 1, including TGA.

Naturally, peak areas corresponding to the heats of reaction are calculated with respect to the baseline around the peak. Since in this case the baseline continues at different levels around the peaks, their bases are assumed to be inclined as visible in Figure 27 where the previous DSC-thermogram is presented with respect to specific heat capacity.

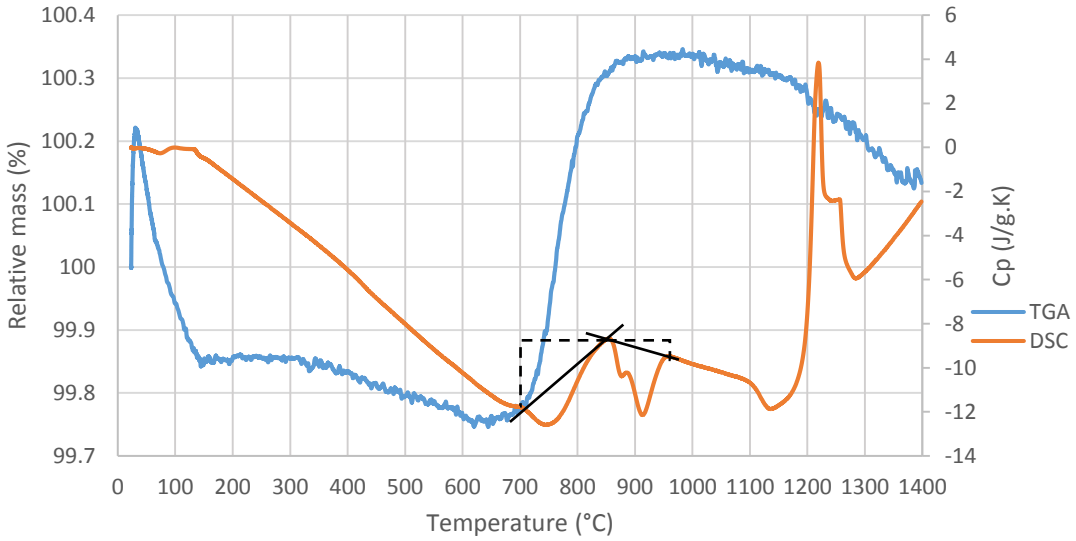

Figure 27. DSC-thermogram with respect to specific heat capacity, and TGA-thermogram of inorganic fraction of wool 1. Baselines for peaks are marked as black lines. As the beginning of the first peak was unclear, its location was judged by comparison with the TGA curve.

The specific heat capacity is calculated from momentary heat flow according to Equation 27 at each measurement point. Areas of the peaks corresponding to the heats of reaction were evaluated by numerical integration by applying the method described in Section 4.3. The baseline for integration is set to the specific heat capacity at 850 °C where the first reaction ends and the second begins. Since the bases of the peaks are inclined, the final values for the heats of reaction were obtained when areas of triangles marked with dashed lines in Figure 27 were subtracted from the results of numerical integration. As the measurement points were densely packed with only 0.3 s intervals, the integral could be considered as precise. Table 5 presents heats of reaction along with their sum. This combined heat of reaction describes the exothermic reactions of solid phase since they are modeled as a single reaction.

Table 5. Heats of reaction for solid phase reactions.

	Reaction 1	Reaction 2	Combined
ΔH_r (kJ/kg)	-115.215	-140.684	-255.899

To complement the original DSC-measurement presented in Figures 26 and 27, carried out with heating rate of 15 °C/min, two differential thermal analyses are performed from the inorganic fraction of wool 27 with rates of 5 and 10 °C/min. As a result of these DTAs, differential temperature and heat flow curves are obtained for both analyses. Associated changes in mass are recorded simultaneously with TGA. However, obtained heat flow curves are incomparable in shape to older thermograms of wool 1, as Figure 28 shows. It presents the heat flow from the sample for experiments with both heating rates. In all following DTA thermograms the exothermic direction is up.

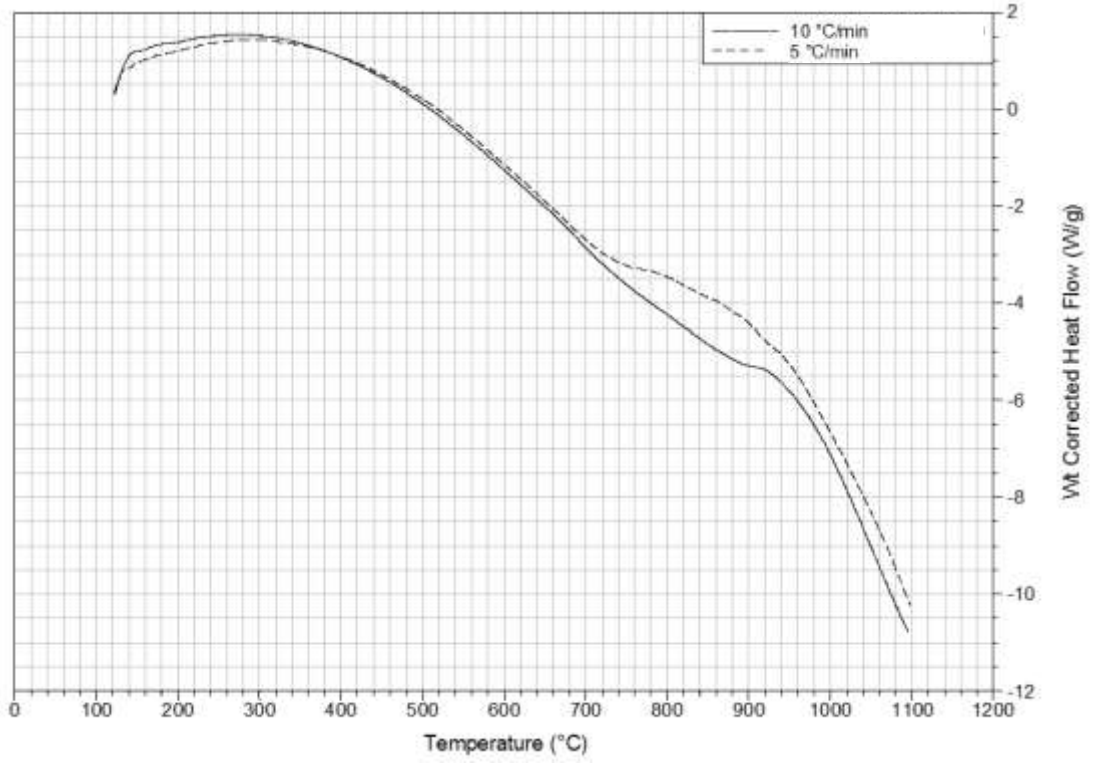

Figure 28. Heat flows during differential thermal analyses of wool 27 as a function of temperature.

In addition to being completely different in shape to the thermogram of wool 1, here only one reaction is visible as a single, wide peak. This is the main reason behind the choice to describe the solid phase reactions as a combined reaction, for

which the kinetic parameters were determined by the Kissinger method (Kissinger, 1957). However, as it is difficult to judge the exact location of the peak from the heat flow curves, DTA curves are used instead to determine the reference temperature. Reaction order is determined according to the shape index method presented in Section 3.5. Figures 29 and 30 present DTA curves for heating rates of 5 and 10 °C/min, respectively, along with their respective TGA curves.

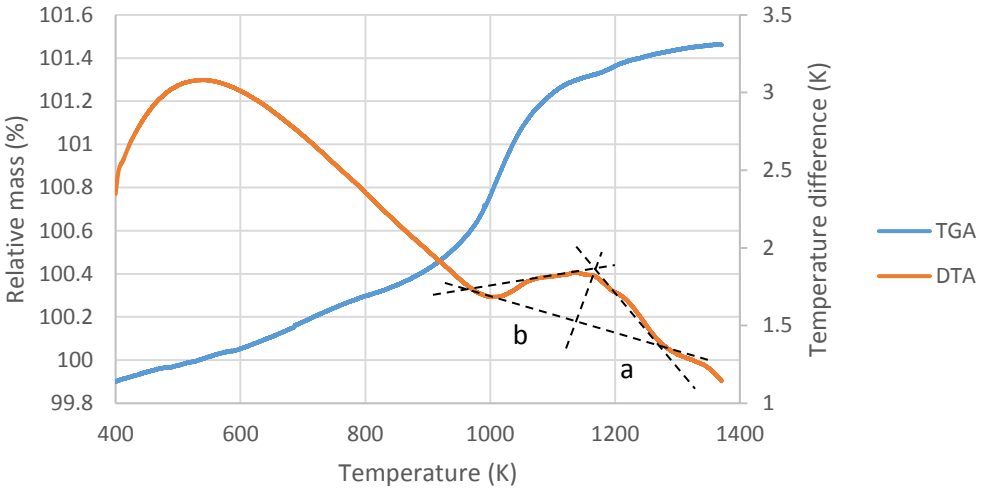

Figure 29. DTA carried out with heating rate of 5 °C/min with the corresponding TGA and determination of the shape index.

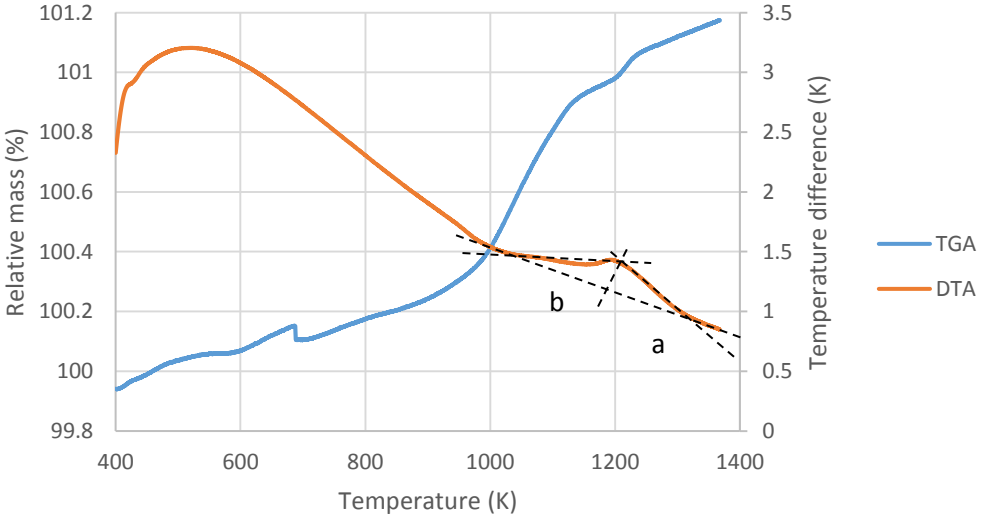

Figure 30. DTA carried out with heating rate of 10 °C/min with the corresponding TGA and determination of the shape index.

Figures 29 and 30 show that the weight gain associated to the first reaction of Figures 26 and 27 begins approximately at the same moment as the DTA peak, so the DTA thermograms could be considered reliable in this respect. This weight gain is most likely caused by oxidation of the fiber material. Table 6 presents reference temperatures, shape indexes and kinetic parameters for solid phase reactions of wool. Arrhenius parameters are solved according to the procedure described in Section 3.5 and as already executed in determination of oil parameters. Figure 31 shows the linearization of DTA reference temperatures and the fitted linearization from which Arrhenius parameters were derived.

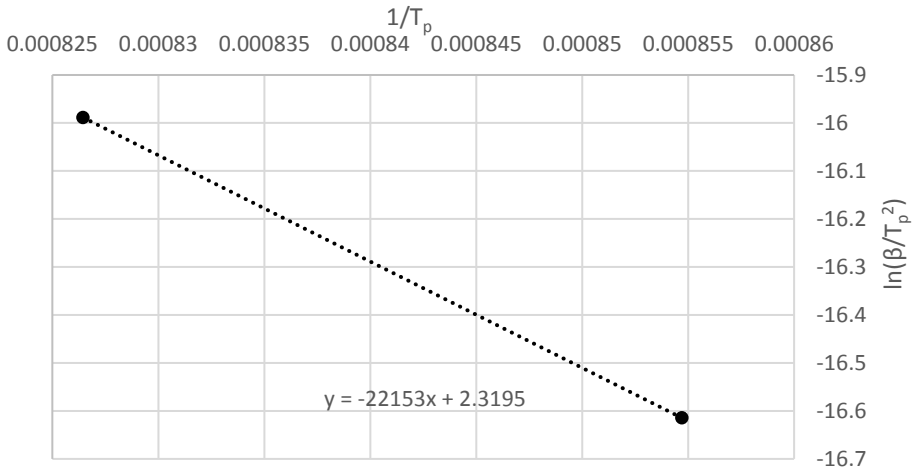

Figure 31. Linearization of reference temperatures according to Equation 32 from differential thermal analyses of inorganic fraction of wool 27.

Table 6. Reference temperatures T_p and shape indexes S from differential thermal analyses and accordingly calculated kinetic parameters for wool solid phase reactions. The table presents also the average of two reaction orders obtained from the experiments, which is the reaction order used for wool reactions in subsequent modelling.

β (°C/min)	T_p (K)	E_a (J/mol)	A (1/s)	$S = \frac{a}{b}$	$N_s = 1.26\sqrt{S}$	N_s, average
5	1170	184189	225309	0.763	1.10	1.16
10	1210			0.929	1.21	

5.3 Validation of the one-dimensional simulation model

Section 1.2 specifies a validation process to consist of three steps: “comparing model predictions with experimental measurements, quantifying the differences in light of uncertainties in both the measurements and model inputs, and deciding if the model is appropriate for the given application”. (McGrattan et al., 2017, pp. 1-3) Annex E compares the simulated temperatures of each wool to the corresponding experimental results. This section also presents some examples to illustrate obtained results and to justify conclusions about the validity of the model. Differences are quantified as the average relative uncertainty of simulation in Subsection 5.3.2. Relative uncertainty of a simulated result with respect to experimental measurement is calculated for each MATLAB and FDS simulation. After the evaluation of uncertainties and the quality of fit, Subsection 5.3.3 discusses whether the model is valid or not. Section 5.4 presents a sensitivity analysis which evaluates the effect of uncertainties in the model inputs and parameters. Table 7 presents a summary of model parameters and the method with which they are obtained.

Table 7. Summary of model parameters.

Parameter		Value		Source
		MATLAB	FDS	
Binder decomposition	E_a (J/mol)	38131	15209	Fitted to simulation model
	A (1/s)	0.6318	0.0068	
	N_s	0.7		Fitted to the reconstructed TGA experiment
	ΔH_r (kJ/kg)	-25000		Materials manufacturer
Oil decomposition	E_a (J/mol)	49696	98992	Fitted to simulation model
	A (1/s)	0.9299	3174700	
	N_s	0.2		Fitted to the reconstructed TGA experiment
	ΔH_r (kJ/kg)	-45000		Materials manufacturer
Wool solid phase reactions	E_a (J/mol)	184189		Experimental
	A (1/s)	225309		

	N_s	1.16		
	ΔH_r (kJ/kg)	-255.899		
Refractive index of fibers		1.2		Fitted to experimental thermal conductivity
Fiber material density (kg/m^3)		2850		Materials manufacturer
Binder density (kg/m^3)		1300		Materials manufacturer
Oil density (kg/m^3)		750		Materials manufacturer
Specific heat capacity of combustible fraction (J/kg·K)		1700		Materials manufacturer
Steel sheet thickness (mm)		1		Experiment reports
Wool, steel and brick emissivities		0.85		Fitted to simulation model
Furnace wall thickness (mm)		13	11	Fitted to simulation model
Time step (s)		0.2	2 (at maximum)	In MATLAB iterated until precise simulation results were obtained in a calculation time of few minutes. FDS can adjust the time step independently so a large maximum value could be set. 1000 is a maximum number of cells per layer in FDS, employed in this model.
Number of discretization nodes in wool layer		44	1000	

5.3.1 Wools abandoned from validation

Wools 12, 18 and 26 were abandoned from the validation process because of their inconsistent experimental fire resistance test results compared to similar wools, causing therefore poor correspondence with simulation. A likely reason are measurement errors on the cold side temperature. Wools 12 and 26 were abandoned since the measured final temperatures were significantly below the simulated one, as Figures 32 and 33 show, respectively. This might be caused by a poor contact of thermocouples with wool. Figure 34 shows that in the experimental temperature of wool 18 is visible a sudden jump a little before 60 minutes. In addition, the peak value of temperature is significantly higher than the recorded

peak of 166 °C on wool 15. This is a contradiction since the higher density and lower loss on ignition of wool 18 should hinder the temperature rise below wool 15.

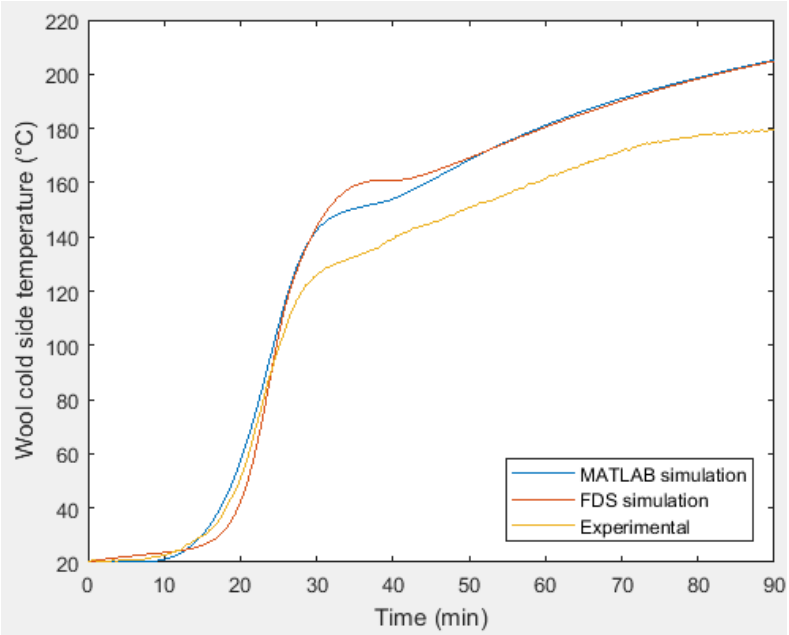

Figure 32. MATLAB and FDS simulations of wool 12 compared to experimental measurement.

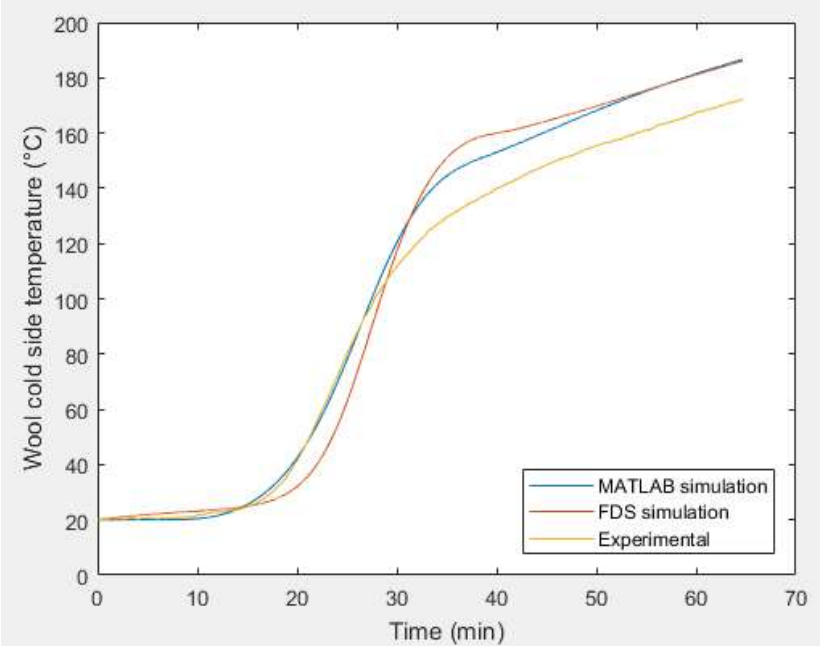

Figure 33. MATLAB and FDS simulations of wool 26 compared to experimental measurement.

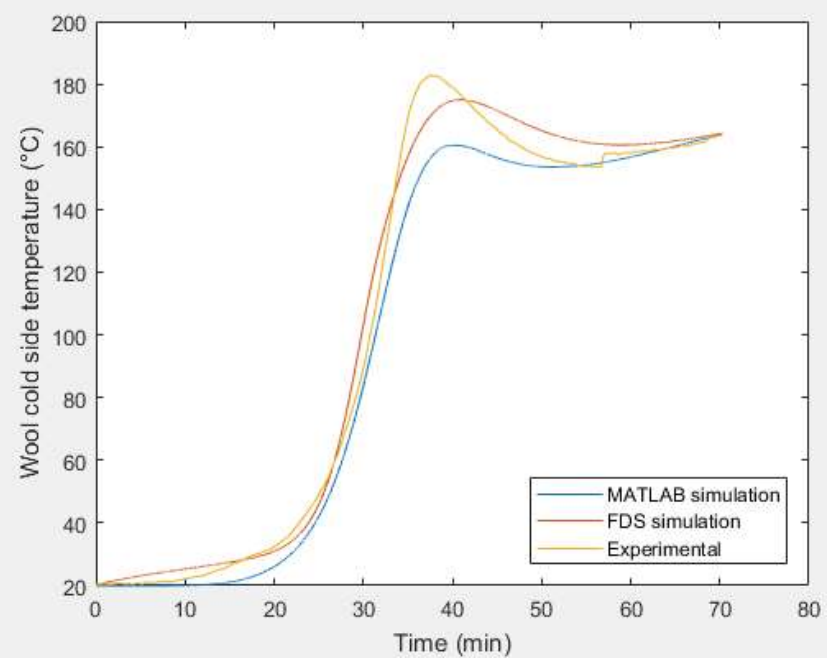

Figure 34. MATLAB and FDS simulations of wool 18 compared to experimental measurement.

5.3.2 Average relative uncertainty of simulations

After execution of simulations it was noticed that density and binder-, and oil contents affect the most on the quality of the fit of the simulation. Therefore wools are divided into four groups: wools with the density up to approximately 100 kg/m^3, wools with the density of approximately 140 kg/m^3, wools the with oil content equal to or higher than 0.25 wt-% and wools with high loss on ignition upwards from approximately 4.7 wt-%. Average relative uncertainty is calculated within each group separately for the MATLAB and FDS simulations.

Validity of the model is evaluated by relative uncertainty, since it is independent of the scale of measured quantity. By definition it is the ratio of measurement error to the measured value. (Baird, 1962; Taylor, 1997) As the uncertainty of simulation is under evaluation, the “measurement error” is here considered to be the difference between simulated and experimental result. To account for differences between simulated and experimental measurements over the whole experiment, the error is interpreted as the area between the simulated and experimental curves, experimental result being the area under experimental curve. Therefore the reported uncertainty is a mean value over the simulation. These areas were solved by the numerical integration method described in Section 4.3. When calculating the area under the simulated curve, the zero level is considered to be equal to the

ambient temperature. Equation 60 gives the relative uncertainty of simulated temperature over an entire simulation $\delta_r T$ as a percentage.

$$\delta_r T = \frac{error}{experimental\ result} \cdot 100\ \% = \frac{\int_0^{t_{max}} |T_{sim}(t) - T_{exp}(t)| dt}{\int_0^{t_{max}} T_{exp}(t) dt} \cdot 100\ \% \quad (60)$$

where t_{max} is the duration of an experiment or simulation, $T_{sim}(t)$ is the measured temperature as a function of time and $T_{exp}(t)$ is the experimental temperature in a fire test as a function of time.

Table 8 presents relative uncertainties for each simulation. It also reports average value, maximum, minimum and standard deviation for relative uncertainties of individual simulations for each group of wools.

Table 8. Relative uncertainties of individual simulations and statistics drawn from the simulation results of different groups of wools.

Group	Wool	Relative uncertainty, simulated by: (%)		Statistics of relative uncertainty within a group		
		MATLAB	FDS		MATLAB	FDS
Low to moderate density = up to 100 kg/m^3	1	5.9	6.3	Average	4.3	5.6
	2	5.4	5.2	Max	6.9	8.4
	3	6.9	7.5	Min	1.6	2.4
	4	3.1	3.9	Standard deviation	1.7	2.0
	5	2.8	2.8			
	6	4.8	5.8			
	7	2.0	2.4			
	11	4.0	6.0			
	13	3.9	6.0			
	14	1.6	4.3			
	16	5.5	8.4			
	20	6.3	3.5			
	25	3.3	8.1			
	27	5.4	7.6			

	Wool	MATLAB	FDS		MATLAB	FDS
Large oil content = more than 0.25 wt-%	8	3.8	4.1	Average	4.0	3.9
	9	2.6	3.2	Max	5.2	4.9
	10	5.2	5.1	Min	2.6	3.2
	17	4.3	4.9	Standard deviation	1.1	0.8
	Wool	MATLAB	FDS		MATLAB	FDS
High density = approx. 140 kg/m^3	15	6.8	12	Average	6.0	11
	19	5.7	11	Max	6.8	12
	21	5.5	9.5	Min	5.5	9.5
				Standard deviation	0.67	1.2
	Wool	MATLAB	FDS		MATLAB	FDS
High loss on ignition = 4.7 wt-% or more	22	51	39	Average	39	26
	23	57	53	Max	567	53
	24	44	30	Min	15	4.5
	28	38	21	Standard deviation	15	18
	29	30	11			
	30	15	4.5			
		MATLAB	FDS			
Statistics for all wools	Average	12	11			
	Max	57	53			
	Min	1.6	2.4			
	Standard deviation	16	12			

5.3.3 Determination of validity

Estimation of experimental uncertainty in a fire resistance test is based on specifications of the standard SFS-EN 1363-1 (Finnish Standards Association, 2000). The standard specifies the temperature measurement uncertainty to be no more than ±15 °C in the furnace and ±4 °C on the cold side, respectively. The simulation of wool 7, which has one of the lowest relative uncertainties at 2.0 % in the MATLAB

model, is chosen as a reference when estimating the magnitude of experimental uncertainty. MATLAB simulations of “worst case scenarios” for wool 7 are carried out, where furnace and cold side temperatures were simultaneously varied by their respective maximum tolerable uncertainty in the same direction. Error between these maximum and minimum values and the original simulation is calculated according to Equation 60. Figure 35 compares both of these simulations to the original one.

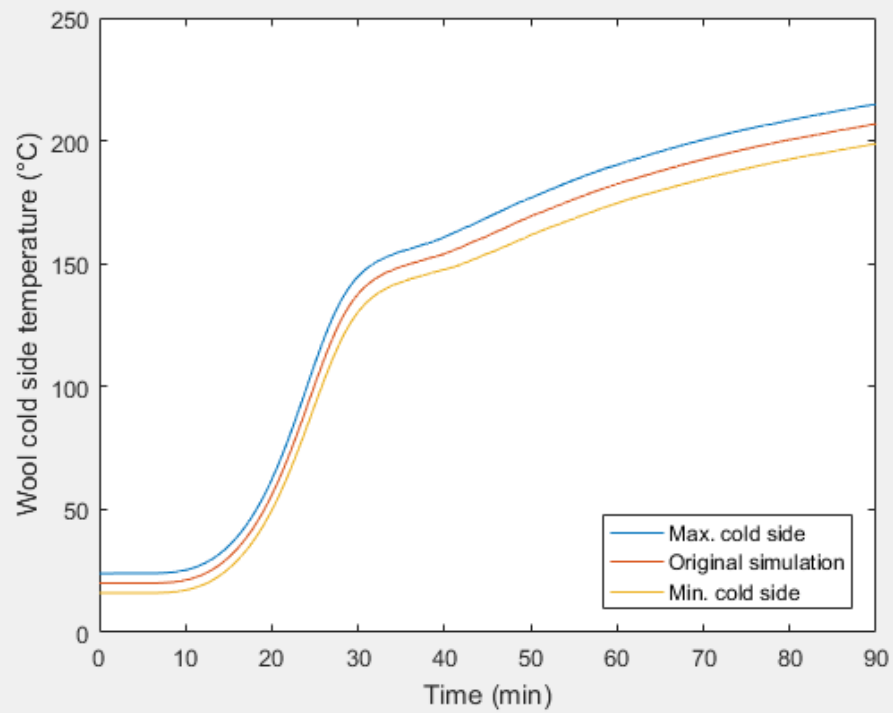

Figure 35. MATLAB simulations of wool 7 when maximum tolerable measurement errors are applied.

The relative uncertainty compared to the original simulation is determined to be 5.2 %, which was assumed to be the experimental uncertainty in a fire resistance test. It was also taken to be the criterion of validity for the models to ensure that they correspond to reality with as good precision as possible. The criterion is acknowledged to be rather strict but nevertheless chosen in order to emphasize the remaining problems in the model. After the kinetic scheme and thermal conductivity model have been revised, re-evaluation of the limit of validity is recommended. If the relative uncertainty of 5.2 % would be distributed evenly along the simulation, in many wools the difference between experimental and simulated final temperatures would be approximately 10 °C, since the temperature rise during a fire resistance test is often in the order of 200 °C.

The uncertainty of the FDS simulation model for wools with the density up to 100 kg/m^3 at 5.6 % is slightly over the 5.2 % criterion. However, the average relative uncertainty of MATLAB simulations at 4.3 % fall under the criterion. Student's t-test is used to evaluate whether the average relative uncertainty could be considered to be under 5.2 % with adequate statistical significance. Null and alternative hypotheses H_0 and H_1 were constructed as described in Equations 61 and 62, respectively.

$$H_0: \delta_{r,a}T > 5.2\ \% \quad (61)$$

$$H_1: \delta_{r,a}T \leq 5.2\ \% \quad (62)$$

where $\delta_{r,a}T$ is average relative uncertainty for simulation within a group of wools.

If the null hypothesis is rejected in a t-test, it could be said with confidence determined by the chosen significance level that the average relative uncertainty in all simulations is below 5.2 %. A customary value of 0.05 is chosen as the significance level, meaning 95 % probability of average relative uncertainty lying below 5.2 % if the null hypothesis is rejected (Mellin, 2006). The test quantity t for t-test is constructed according to Equation 63 (Mellin, 2006).

$$t = \frac{\delta_{r,a}T - \delta_{r,a}T_0}{s/\sqrt{n}} \quad (63)$$

where $\delta_{r,a}T_0$ is the objective value of 5.2 % for the average relative uncertainty, s is the standard deviation of relative uncertainty within a group of wools and n is the sample size, or the amount of wools in a group.

Table 8 tells that for the low density wools the standard deviation of relative uncertainty of MATLAB simulations is $s = 1.65$ and the amount of these wools is $n = 14$. Therefore, it is assumed that the test quantity t follows the Student's t-distribution with degrees of freedom $n - 1 = 13$ (Mellin, 2006) and the test quantity t obtains a value of -1.96. The form of the alternative hypothesis determines the test in question to be left-tailed, meaning that the null hypothesis is rejected if the test quantity t is lower than the critical value corresponding to the chosen level of significance $t_{0.05}$, i.e. $t < t_{0.05}$ (Mellin, 2006). For the lower-tailed t-test with 13 degrees of freedom applies $t_{0.05} = -1.771$ (Ellison et al., 2009). Therefore, the condition $t < t_{0.05}$ is satisfied since $-1.96 < -1.771$, and so the null hypothesis is rejected. Therefore, it could be said with at least 95 % confidence that the average relative uncertainty is less than 5.2 % for the group of low density wools. One should still bear in mind that the FDS model is still able to capture fire

test behavior of these wools with good precision, as its average relative uncertainty is only very slightly above the decided 5.2 % limit.

It is judged that neither of the MATLAB or FDS models are valid for wools with high oil content, density or loss on ignition. For the latter two groups average relative uncertainties are for MATLAB and FDS simulations 5.98 and 10.81, and 39.10 and 26.40, respectively, which are over the 5.2 % criterion. Average relative uncertainties for the wools with high oil content are below this criterion. However, on both MATLAB and FDS simulations the temperature peak caused by oil decomposition reactions resulted into an unacceptably large local deviation from the experimental temperature time series. Figures 36, 37 and 38 show representative examples for wools with high oil content, density and loss on ignition, respectively. On the other hand, the average relative uncertainty of MATLAB simulations of dense wools at 5.98 is close to the 5.2 % threshold, but however judged to be not valid to emphasize observed problems with thermal conductivity. Subsection 5.5.3 discusses uncertainties on thermal conductivity compromising the fit of simulation on dense wools, which result into an overprediction of temperature, as Figure 37 shows.

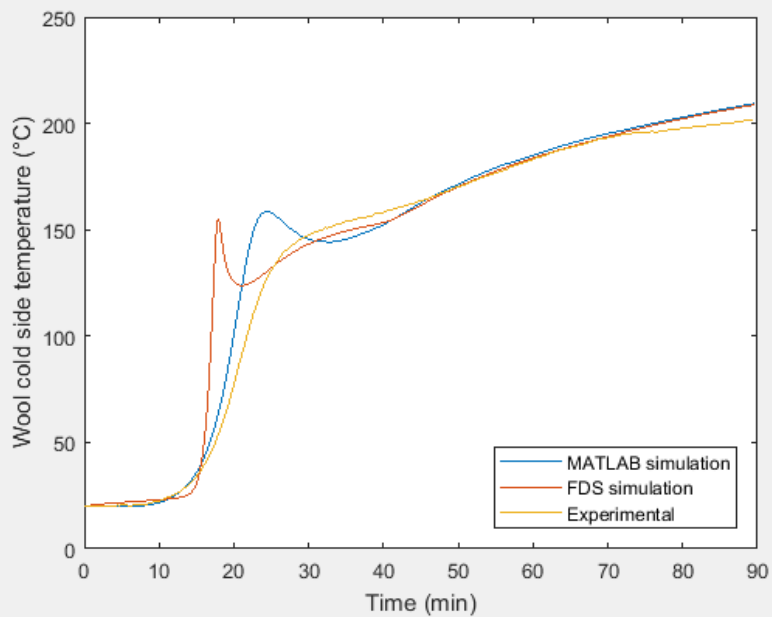

Figure 36. MATLAB and FDS simulations compared to experimental measurement for wool 10, the wool with the highest oil content of 0.46 wt-%.

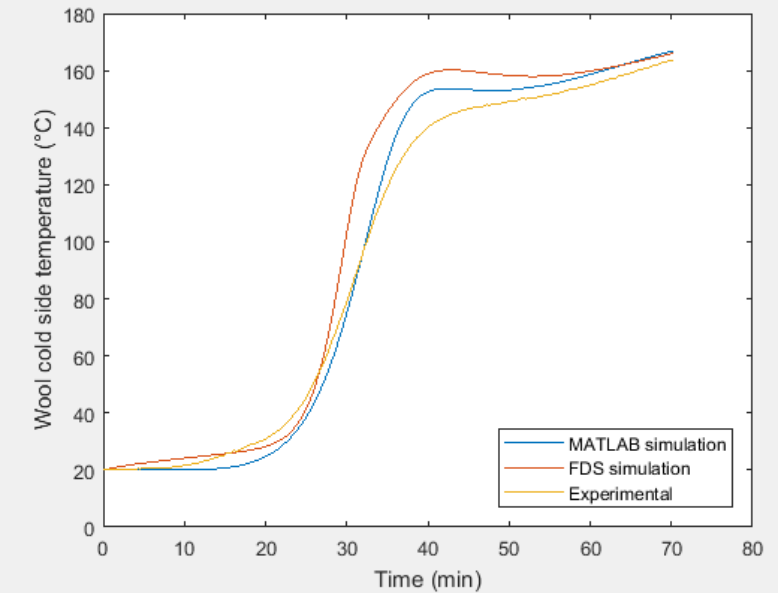

Figure 37. MATLAB and FDS simulations compared to experimental measurement for wool 19, the wool with the highest density of 147.7 kg/m^3.

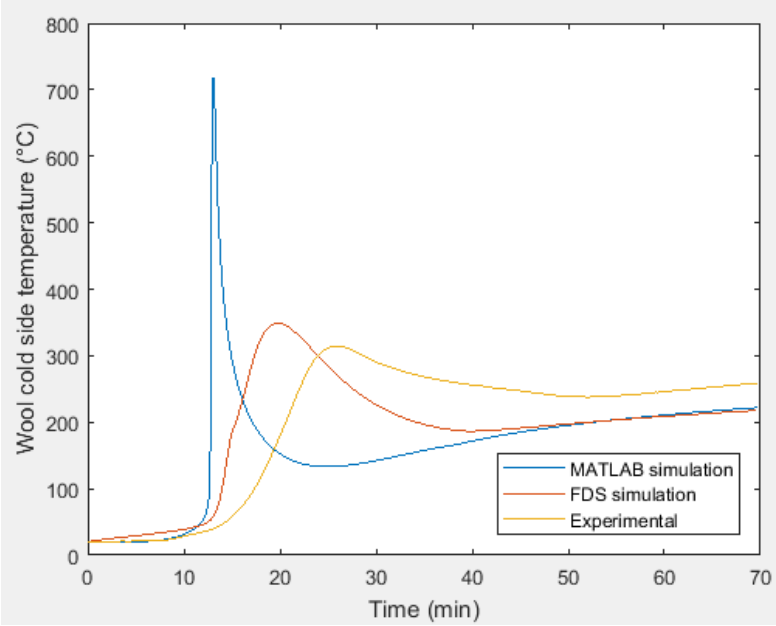

Figure 38. MATLAB and FDS simulations compared to experimental measurement for wool 24, the wool with the highest loss of ignition of 9.8 %.

5.4 Sensitivity analysis of model inputs

Effect of uncertainties in model inputs is evaluated by a sensitivity analysis. Investigated model inputs are density, loss on ignition, oil content, fiber content, fiber thickness, fiber angle of orientation, emissivity, convective heat transfer coefficient and kinetic parameters. In addition, the effect of variation in the effective values of thermal conductivity and specific heat capacity are investigated in the analysis. The sensitivity analysis is decided to be carried out for wool 7, whose investigated input parameters are density 99.6 kg/m^3, loss on ignition 1.1 wt-%, oil content 0.19 wt-%, fiber content 62 %, fiber thickness 3.7 µm and fiber angle of orientation 29.9°. The justification is that neither its density, loss on ignition nor oil content were on region where the quality of the fit would be poor. Also, its relatively high angle of orientation highlights its effect in the sensitivity analysis. Further, as Table 8 shows, it has one of the lowest relative uncertainties at 2.0 % or 2.4 % in MATLAB or FDS, respectively. Figure 39 presents MATLAB and FDS simulations of wool 7 compared to experimental measurement as a reference.

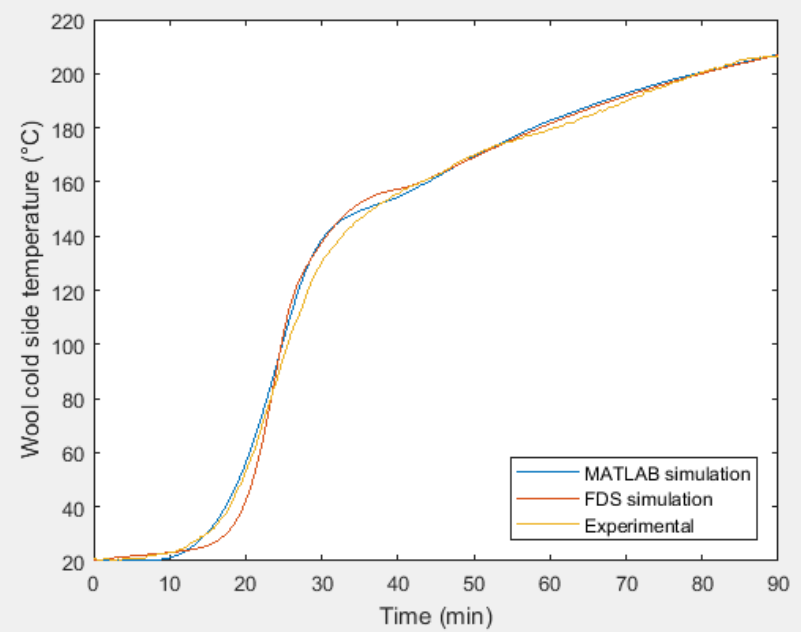

Figure 39. MATLAB and FDS simulations of wool 7 compared to experimental temperature measurement.

5.4.1 Sensitivity analysis of effective thermal conductivity

Variation in thermal conductivity results into changes in the final temperature. Input quantities affecting conductivity are density, fiber content, fiber thickness and fiber angle of orientation. Figure 40 presents as a spider graph a quick sensitivity

analysis on the effect of variation in these quantities, where the final temperature of simulation is presented as a function of variation in a quantity. Since effective thermal conductivity is largely dependent on refractive index and extinction coefficient, whose exact values are unknown, the effective thermal conductivity itself is included also in this sensitivity analysis. The sensitivity analysis presented herein is carried out in MATLAB. A corresponding analysis for the FDS model is not presented since the results are practically identical.

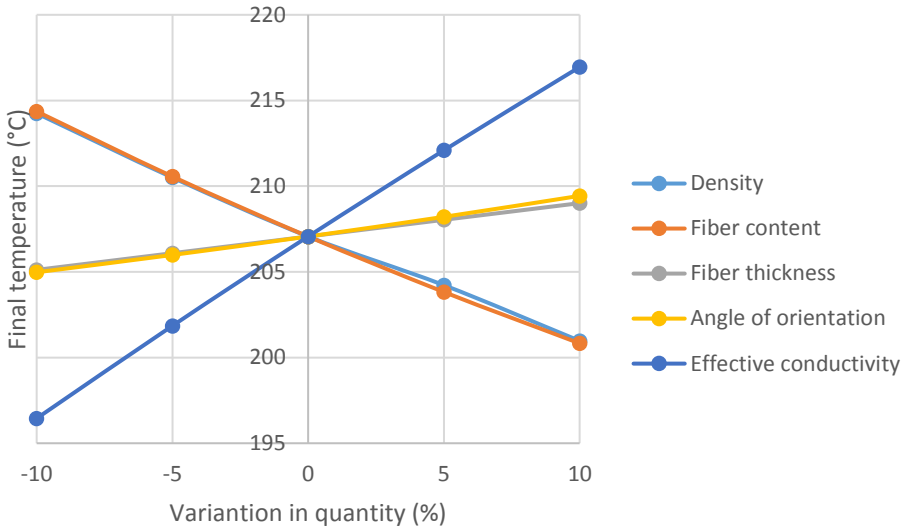

Figure 40. Sensitivity analysis of quantities affecting the effective thermal conductivity presented as the final temperature of simulation as a function of variation in a quantity.

It is visible that variations in density and fiber content have the greatest effect on the final temperature and thus on the effective thermal conductivity. Their analysis results however are considered as “precise” so participation of measurement errors in these quantities into model uncertainty could be considered small. Measured thickness and orientation angle of individual fibers are more uncertain, since they are not discrete values but instead form a distribution. This work reports their measured average values. Additionally, orientation is measured from the side of a wool slab so it does not necessarily correspond to actual orientation angles inside the slab. However, the sensitivity analysis shows that their effect on thermal conductivity is small. The average fiber thickness lies within $\pm$10 % of the declared value with 95 % confidence according to several laboratory reports. In many wools the average angle of orientation is close to zero, compared to 29.9° of wool 7. Therefore, the effect of relative measurement uncertainty of orientation angle

becomes even more insignificant. As a result, refractive index and extinction coefficient emerge as the major causes for uncertainty in thermal conductivity.

Variation in the effective thermal conductivity itself was studied more in detail to obtain insight into possible differences in behavior of MATLAB and FDS simulation models. Figure 41 presents the MATLAB and FDS simulations of wool 7 when its effective thermal conductivity is varied by 40 percent.

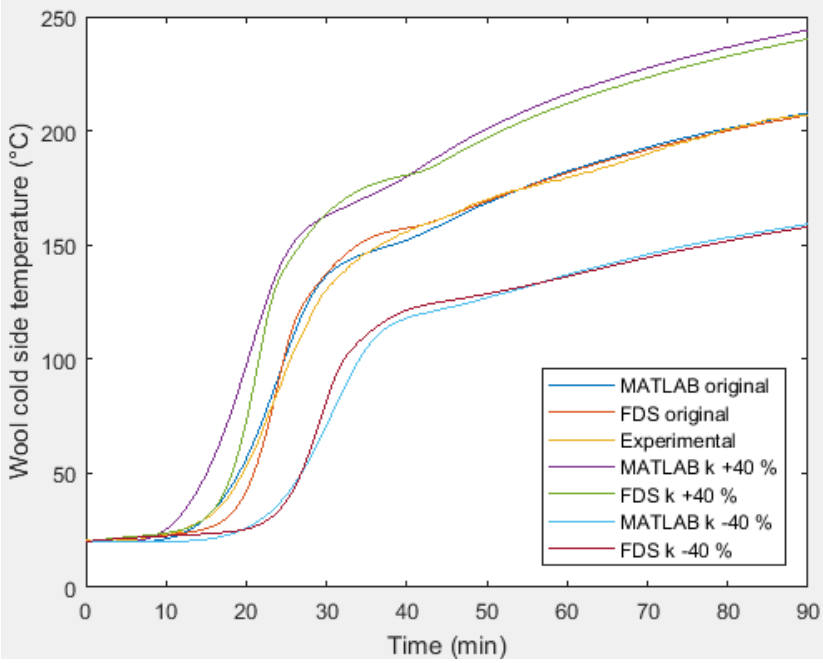

Figure 41. MATLAB and FDS simulations of wool 7 with effective thermal conductivity varied by 40 % compared to experimental temperature measurement.

Figure 41 shows that the FDS model is less sensitive to variations in thermal conductivity as the simulated curve obtained by varied thermal conductivity is in both cases closer to the original value than MATLAB simulations. Meaning, in the wools with low thermal conductivity the heat transfer from the cold side is not as efficient as in MATLAB during the phase of rapid temperature increase. Since high density is a major contributor to low thermal conductivity, Figure 42 presents MATLAB and FDS simulations of wool 7 in hypothetical case where its density is increased by 40 % into 140 kg/m^3 and additionally simulations where both density and loss on ignition are increased by 40 %. The fiber content has a similarly large effect on simulation result as density according to Figure 40. However, it is not noticed to correlate with the quality of the fit of simulation.

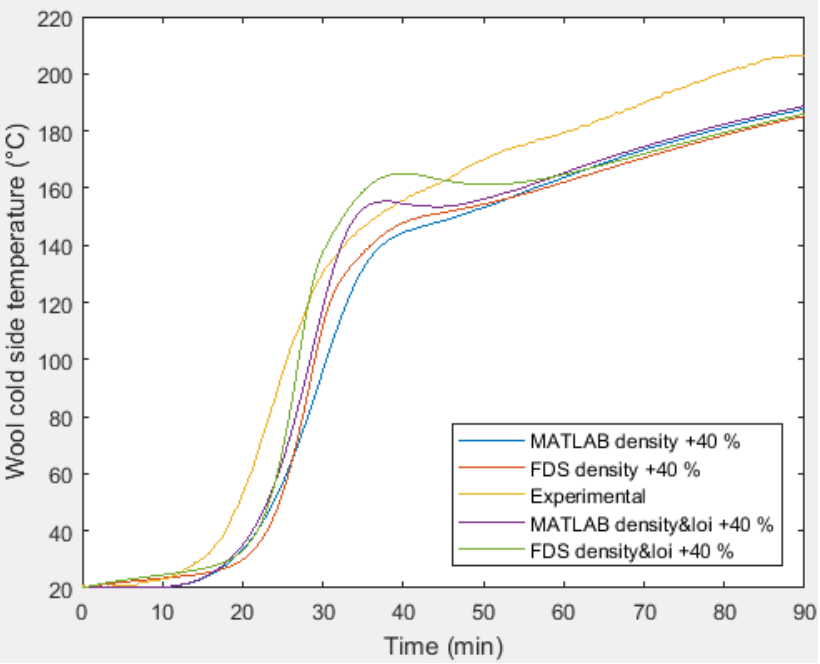

Figure 42. MATLAB and FDS simulations of wool 7 with first density and then density and loss on ignition increased by 40 % compared to experimental temperature measurement.

The figure clearly shows that an increase in density has similar effects on results of MATLAB and FDS simulations as does a decrease in thermal conductivity. Therefore, when thermal conductivity is low and the heat transfer is weaker in FDS compared to MATLAB, this naturally leads to the FDS model being more sensitive to increase in loss on ignition. Figure 42 proves this, which shows the simulation of wool 7 with increased density further modified by increasing loss on ignition by 40 %. The peak resulting from this is noticeably higher and wider in FDS even though the final temperatures are the same. This behavior explains the poorer quality of fit for dense wools simulated with FDS but under the time restrictions of this thesis, the root cause of this difference remains unknown.

5.4.2 Sensitivity analysis of heat transfer on the cold side

Figures 43 and 44 present sensitivity analyses of convective heat transfer coefficient on the cold side and wool emissivity, respectively, which are the parameters that determine the heat release into the ambient conditions at the cold side. Convective heat transfer coefficient is varied by 40 % to make its effect more visible, whereas emissivity is varied by 10 % from its initial value of 0.85. The figures show that both of the models react in a similar manner to variations in these quantities, and only the temperature after the phase of rapid temperature rise is affected in a significant

amount. Therefore, even though the exact value of neither quantity is known, they could be used to adjust the final temperature into its desired level after more precisely known inputs are implemented into the model. As a conclusion, neither convective heat transfer coefficient on the cold side nor wool emissivity are considered as major sources of uncertainty.

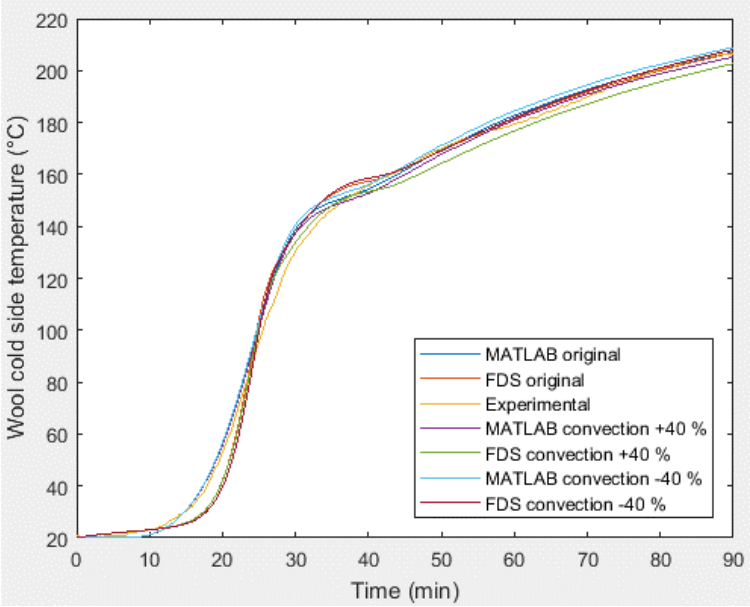

Figure 43. MATLAB and FDS simulations of wool 7 with convective heat transfer coefficient varied by 40 % compared to experimental temperature measurement.

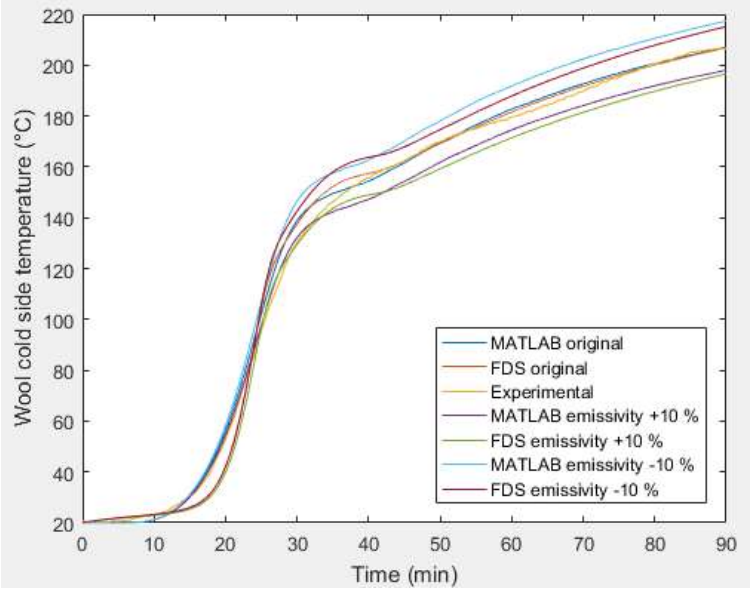

Figure 44. MATLAB and FDS simulations of wool 7 with wool emissivity varied by 10 % compared to experimental temperature measurement.

5.4.3 Sensitivity analysis of specific heat capacity and reaction parameters

Figure 45 presents a sensitivity analysis of specific heat capacity by varying its effective value by 10 % in both of the MATLAB and FDS models. The figure shows that specific heat capacity has a larger effect on the thermal penetration time than on the final temperature. The effect of variation in specific heat capacity is small and Subsection 3.7.4 proves that the computational specific heat capacity of wool material is close to the measured value. Notwithstanding the lowest temperature range, the difference between computational and measured specific heat capacity is equal to or less than 10 %. Therefore, errors in specific heat capacity are not a major contributor to model uncertainty.

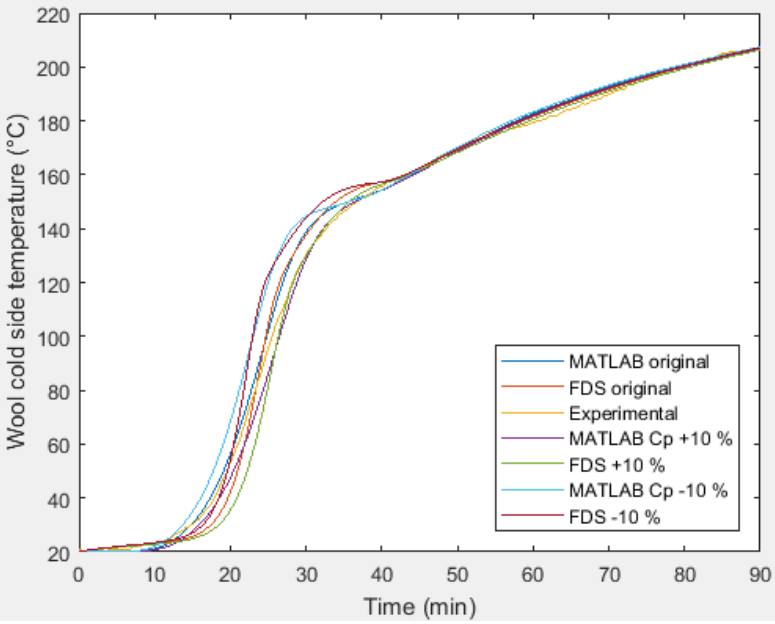

Figure 45. MATLAB and FDS simulations of wool 7 with effective specific heat capacity varied by 10 % compared to experimental temperature measurement.

Figure 46 presents a sensitivity analysis, which investigates possible differences in sensitivities of MATLAB and FDS models to specific heat capacity. The analysis shows that both models respond even to large variations in a similar manner, so it is concluded that the poor fit of FDS simulations of dense wools is caused by different sensitivities of the models to thermal conductivity.

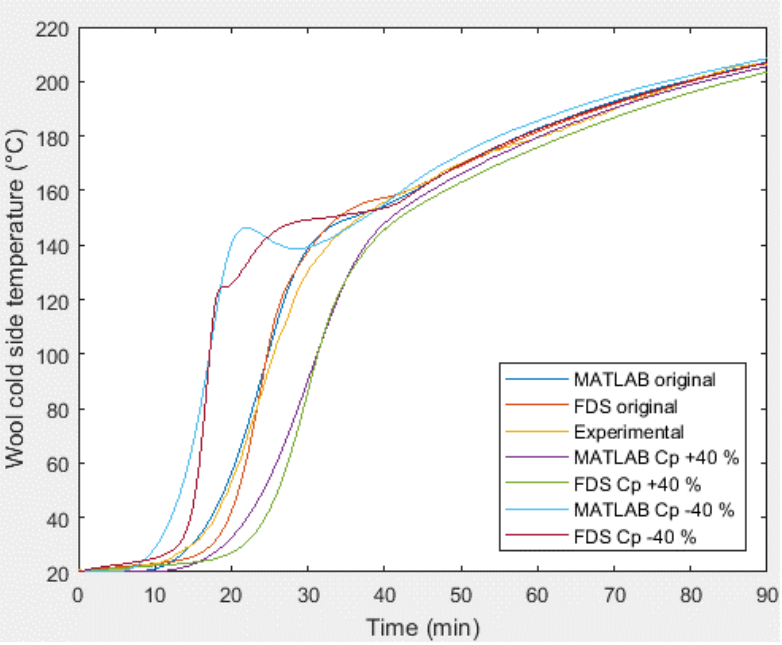

Figure 46. MATLAB and FDS simulations of wool 7 with effective specific heat capacity varied by 40 % compared to experimental temperature measurement.

Arrhenius parameters and additionally loss on ignition are considered here as the reaction parameters. Effect of variation in oil content is not examined since its effect is small in many wools and its degradation kinetics is already judged to be erroneous in Section 5.3. Figures 47 and 48 present sensitivity analyses for activation energy and frequency factor, respectively. Both are varied by 50 % to highlight their effect. Additionally, a large variation is justifiable by uncertainty in their values due to scarce and partially uncertain thermoanalytic data used in kinetic parameters determination.

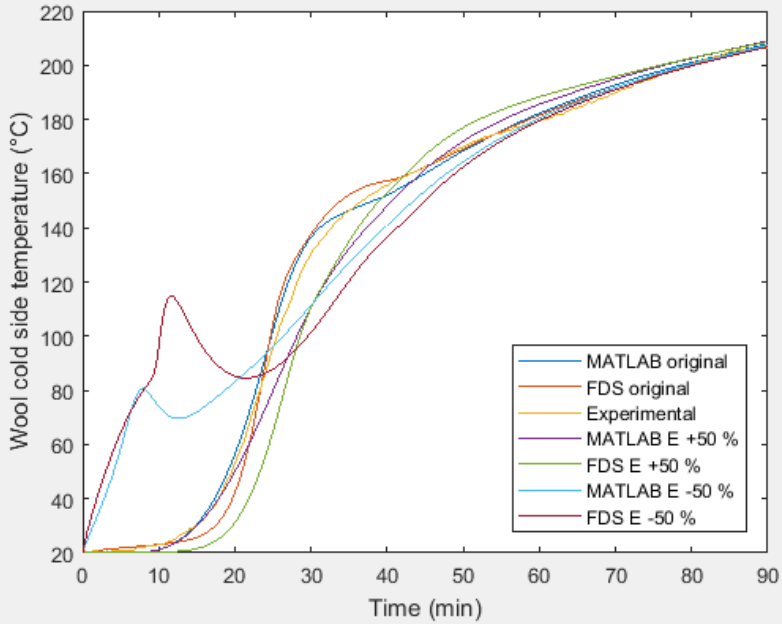

Figure 47. MATLAB and FDS simulations of wool 7 with activation energy of binder degradation varied by 50 % compared to experimental temperature measurement.

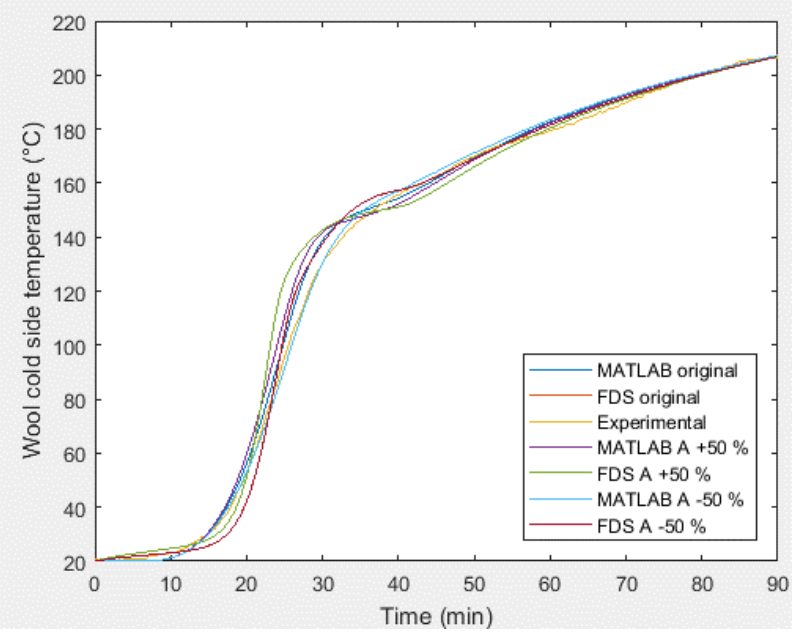

Figure 48. MATLAB and FDS simulations of wool 7 with frequency factor of binder degradation varied by 50 % compared to experimental temperature measurement.

The analysis shows that the effect of frequency factor is negligible compared to activation energy, reason being that activation energy affects the reaction rate exponentially unlike frequency factor. Figure 47 shows that responses to variation

in activation energy differ slightly in the models. This is most likely explained by the fitted kinetic parameters being different to each other in the MATLAB and FDS models. Table 9 compares these parameters to the experimental ones.

Table 9. Fitted kinetic parameters in the MATLAB and FDS models.

	MATLAB		FDS		Experimental	
	Binder	Oil	Binder	Oil	Binder	Oil
E_a (J/mol)	38131	49696	15209	98992	93003	99392
A (1/s)	0.6318	0.9299	0.0068	3174700	1071	152697

Large differences between the fitted kinetic parameters in separate models is explained by aforementioned lesser sensitivity of the FDS model to variations in thermal conductivity. This required implementation of slow binder decomposition kinetics into the FDS model to spread the reactions over a wider interval, thus preventing formation of an unwanted temperature peak. Therefore, different kinetic parameters were required to obtain the best possible fit for each simulated wool type. In addition, differences in the reaction models indicated by Figure 25 in Section 5.1 have at least a minor effect. Values of kinetic parameters are considered as a major participant in model uncertainty due to poor correspondence between fitted and experimental values and uncertain measurement data. Unknown heating rate and binder to oil ratio of the sample are the main source of uncertainty in the thermogravimetric data used in determination of decomposition kinetics.

Figure 49 shows the effect of variation in loss on ignition on simulation results. The figure shows that variation in loss on ignition causes not significant effects on wools with moderate binder content, such as wool 7. Also, responses of the MATLAB and FDS models are similar. However, as Subsection 5.4.1 describes, denser wools are more sensitive to variations in loss on ignition.

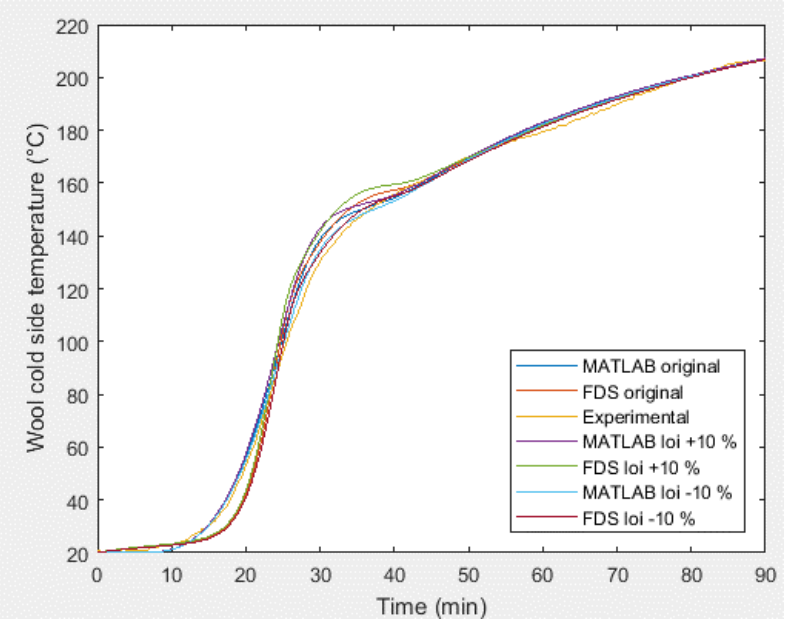

Figure 49. MATLAB and FDS simulations of wool 7 with loss on ignition varied by 10 % compared to experimental temperature measurement.

A sensitivity analysis with larger 40 % variation in loss on ignition is carried out to examine possible different sensitivities of the models also on wools with lower density, i.e. higher thermal conductivity. Figure 50 presents the result of analysis.

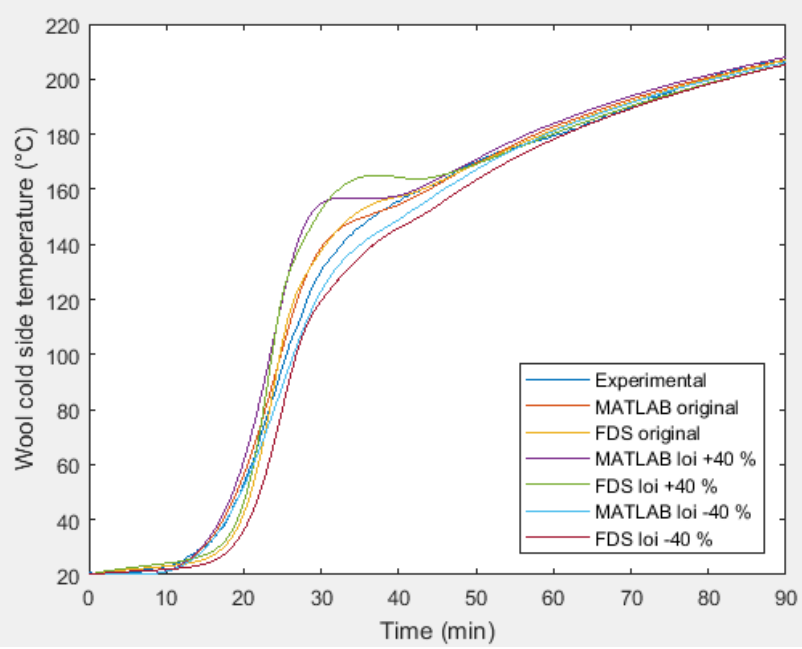

Figure 50. MATLAB and FDS simulations of wool 7 with loss on ignition varied by 40 % compared to experimental temperature measurement.

The analysis presented as Figure 50 shows that also on less dense wools the FDS model is more sensitive to changes in loss on ignition. The effect is however not as pronounced as with dense wools with low thermal conductivity.

5.5 Discussion of results

This section analyzes the results presented above, draws conclusions from them and estimates the need for further research if uncertainties prevail. This section also discusses the two-dimensional model for which the validation process is not executed due to shortcomings of the three-dimensional temperature solver of FDS. The three-dimensional solver is in the beta testing phase at the time of writing.

5.5.1 Kinetic parameters of decomposition of organic fraction

As already discussed in Section 5.1, thermoanalytic results for determination of kinetic parameters are not considered reliable. Thermogravimetric analyses of cured binder were of little use due to surprisingly complex degradation occurring in multiple sequential reactions. Therefore, an older analysis of binder-oil mixture had to be employed instead. A simplifying assumption of completely independently occurring reactions is made based on relatively separate DTA peaks and observation from TGA on mass loss to occur on two steps. This assumption is necessary to obtain tangible results. However, temperature ranges of these two reactions are likely to overlap, so pyrolysis ranges read from the TG-thermogram might not correspond to the truth. Also, as the accurate mass fractions of binder and oil in the sample were unknown, they were read from TGA at the point where the first decomposition step ended and another begun. However, in the case of overlapping reactions, obtained mass fractions are only coarse estimates. Another major cause of uncertainty is the heating rate, which is an elemental quantity in determination of kinetic parameters from TGA results. It was however unknown for the employed thermogravimetric analysis. Therefore, it had to be evaluated from comparison with thermogravimetric measurements of oil. The obtained rate of 3 °C/min is in the sensible range but its calculation is based on kinetic parameters of oil, which are uncertain with only two TGA runs carried out on independent heating rates. One should also bear in mind that in principle the employed method is not consistent for non-first order decomposition reactions.

Also, it remains as a matter of suspicion if the same kinetic parameters apply for all types of wools throughout the whole experiment. The work is carried out under an assumption that internal convection inside the wool slab supplies adequate amount

of oxygen for oxidative decomposition of organic fraction. The need for externally supplied air is further proved here by examining wool 20. It has the lowest density of 38.3 kg/m^3, the lowest loss on ignition of 0.7 wt-%, and a calculated porosity of 0.9864. Therefore one cubic meter of this wool contains 0.9864 m^3 of air and 268.1 g of combustible fraction. If the whole combustible fraction is assumed to follow the molecular formula of $C_8H_6O_2$ of the repeating unit of phenol-formaldehyde resin (National Center for Biotechnology Information, 2005), this translates to 1.999 moles of repeating units. Equation 64 presents the reaction scheme of resin oxidation, according to which the oxidation of one mole of resin requires 8.5 moles of oxygen.

$$C_8H_6O_2 + 8.5O_2 \rightarrow 8CO_2 + 3H_2O \quad (64)$$

Since the molar volume of ideal gas is 0.0224 m^3/mol (Keskinen, 1989) and the oxygen content of air is 21 %, one cubic meter of this wool contains approximately 9.2 moles of oxygen. This is significantly lower than 17 moles of oxygen required to oxidize the approximately two moles of repeating units of resin. Therefore, externally supplied air is indeed necessary for the complete combustion of organic fraction, if air contained by the wool itself is not enough even in the wool with the lowest absolute binder content.

Comparison of simulations with high and low losses on ignition gives reason to question the assumption on plentiful air for oxidation supplied by internal convection. Figure 51, which presents simulations of wool 15 with a LOI of 2.1 wt-%, shows that temperature rise on the cold side precedes experimental result in both simulations. On the contrary, in many wools with lesser loss on ignition, such as wool 6 with a LOI of 1.1 wt-% presented in Figure 52, temperature rise lags behind the experimental measurement.

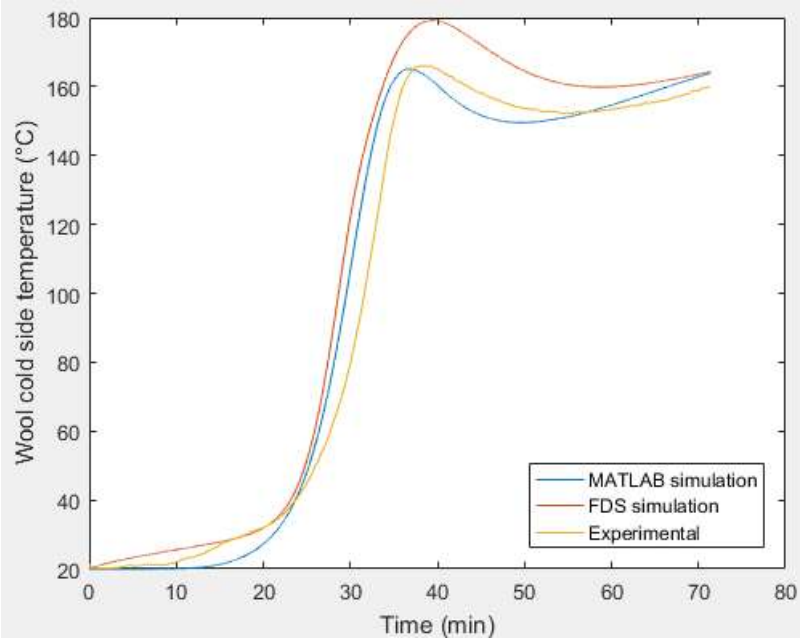

Figure 51. MATLAB and FDS simulations of wool 15 compared to experimental temperature measurement.

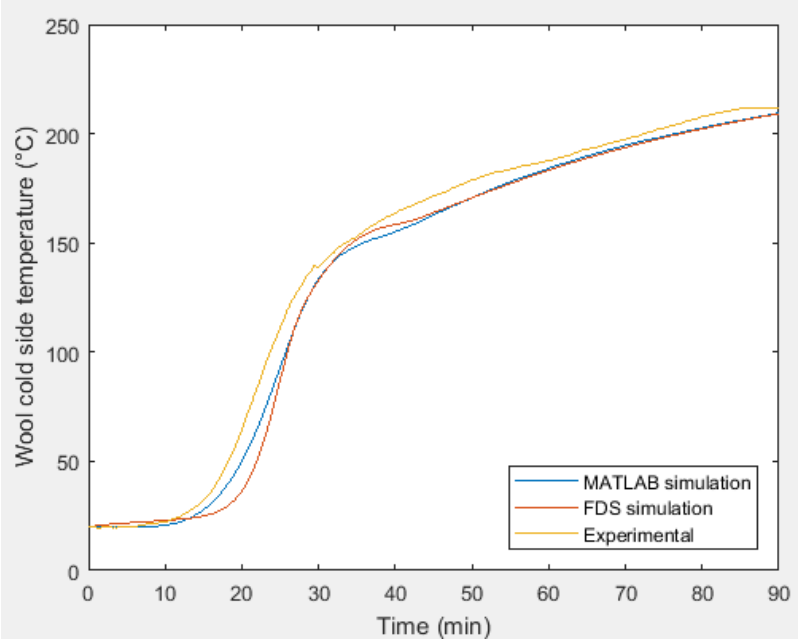

Figure 52. MATLAB and FDS simulations of wool 6 compared to experimental temperature measurement.

Since the kinetic parameters are fitted so that the average fit of a simulation would be as good as possible, this indicates that reactions occur too quickly on wools with high and too slowly with low loss on ignitions. Therefore it is concluded that the

current Arrhenius kinetics do not describe degradation of organic fraction precisely. Instead, a new oxygen mass transfer limited kinetic scheme should be developed to account for the air shortage and to hinder unrealistically high simulated reaction rate in wools with high loss on ignition. Behavior of wools with very high binder content in the current model further emphasizes the need for an updated kinetic scheme. For example, Figure 53 shows that in the simulations of wool 23 with LOI of 9 wt-%, unlimited reactions lead to premature and excessively high temperature peak. Oxygen depletion inside wool is therefore a significant issue with almost absolute certainty.

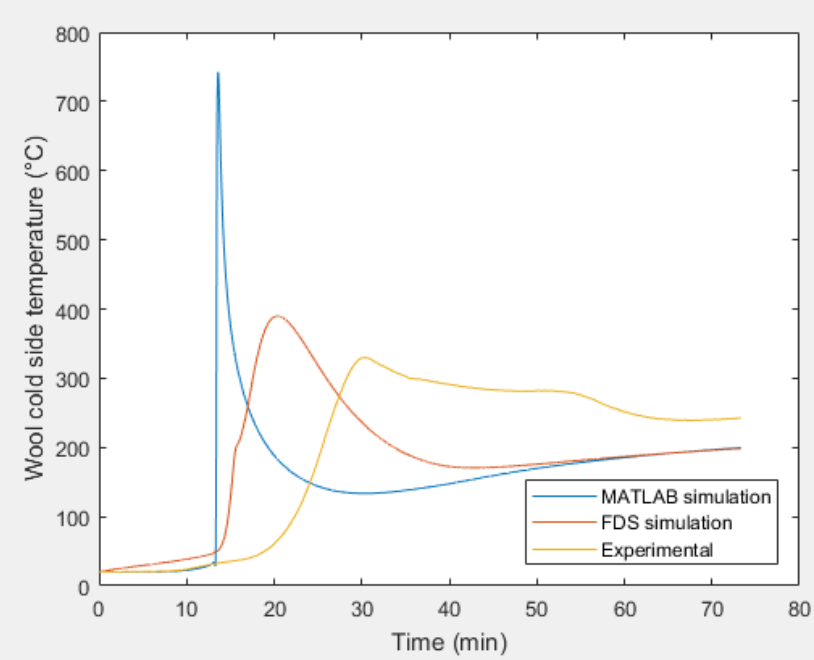

Figure 53. MATLAB and FDS simulations of wool 23 compared to experimental temperature measurement.

The recommended action to obtain valid kinetic parameters is to carry out thermogravimetric analyses to determine them on samples of wool impregnated with binder. Therefore, analysis would occur in the most realistic conditions possible with respect to mass transfer, since in wool binder is dispersed as small droplets. TGA results of binder presented in Section 5.1 could not be utilized because the sample was a single relatively large chunk. Therefore, mass transfer of oxygen inside the particle became soon the limiting factor of the reaction and observed degradation process was not comparable to reactions inside wool. Since the oil content is low in many wools, the most sensible option would be to perform further TGA's on oil from pure samples instead of wool impregnated with oil. Both

analyses should be carried out on more heating rates than just two as in this work. Correlating obtained results with several heating rates for example by Kissinger's method is considered as the most reliable method of evaluating kinetic parameters.

One possible way to compare between different wools the ease of convection inside the slab, determined to be instrumental in providing oxygen for combustion, would be to measure air permeability along the plane of fiber orientation. Now permeability is measured routinely only in direction perpendicular to this. Current experimental apparatus would require installation of multiple slab slices next to each other to measure permeability in this direction. This leads in difficulties in determining which part of air has actually penetrated the wool and which has just passed between the slab slices. Another option to investigate the effect of internal convection is to compare results obtained by the small scale set-up described in Section 3.3 to results from experiments on horizontally set wool slab. Such experiments with a horizontal set-up are carried out on the premises of Danish Institute of Fire and Security Technology.

5.5.2 Heat of reaction and kinetic parameters of solid phase

Uncertainties in the kinetic parameters and the heat of reaction for solid phase reactions do not affect the current model since they had to be switched off to avoid excessively large temperature rise. This is another proof of incorrectness of current kinetic scheme not limited by oxygen mass transfer. However, after the problems in combustion kinetics are addressed to, it is necessary to evaluate implementation of solid phase reactions back into the model.

Section 5.2 describes the calculation of heat of reaction from the DSC-thermogram of inorganic fraction of wool 1. Exothermic peaks corresponding to different solid phase reactions are distinguishable, but baseline not parallel to x-axis results into uncertainties in peak areas which are proportional to heats of reaction. Therefore, if wool solid phase reactions are desired to be determined more accurately, the recommended action is to carry out DSC measurements with an apparatus calibrated so that the baseline is horizontal. Likewise as with decomposition kinetics, it is necessary to carry out DSC or DTA analyses with several heating rates to evaluate kinetic parameters with more accuracy. One should remember that also the oxidation of wool material is a reaction limited by oxygen mass transfer.

5.5.3 One-dimensional model

Table 10 presents as a summary the average relative uncertainties of the one-dimensional models for each group of wools.

Table 10. Average relative uncertainties for simulations of each group of wools.

Group	Average relative uncertainty (%), simulated by:	
	MATLAB	FDS
Low to moderate density = up to 100 kg/m^3	4.3	5.6
Large oil content = more than 0.25 wt-%	4.0	3.9
High density = approx. 140 kg/m^3	6.0	11
High loss on ignition = 4.7 wt-% or more	39	26
Average, all wools	12	11

Kinetic parameters are a major factor affecting the results of one-dimensional simulations, as discussed in Subsection 5.5.1. Another point related to heat release and reaction kinetics is the initial misinterpretation of char yield of the binder. The binder amount is defined in the model as a loss on ignition subtracted by oil content. Binder reactions are suppressed after its content reaches the char yield obtained from TGA results. However, since the loss on ignition analysis recognizes only the volatile fraction of binder, char yield in the model should instead be equal to zero. Char yield was however kept in the model as a simple measure to counter excessive heat release with the current kinetic scheme. Setting the binder char yield to zero would have adverse effects on quality of the fit already on wools with only moderately high losses on ignition, such as wool 15 at 2.1 wt-%. Figure 54 presents its MATLAB simulation with the binder char yield set to zero, compared with the original simulation with the char yield of 28.3 %.

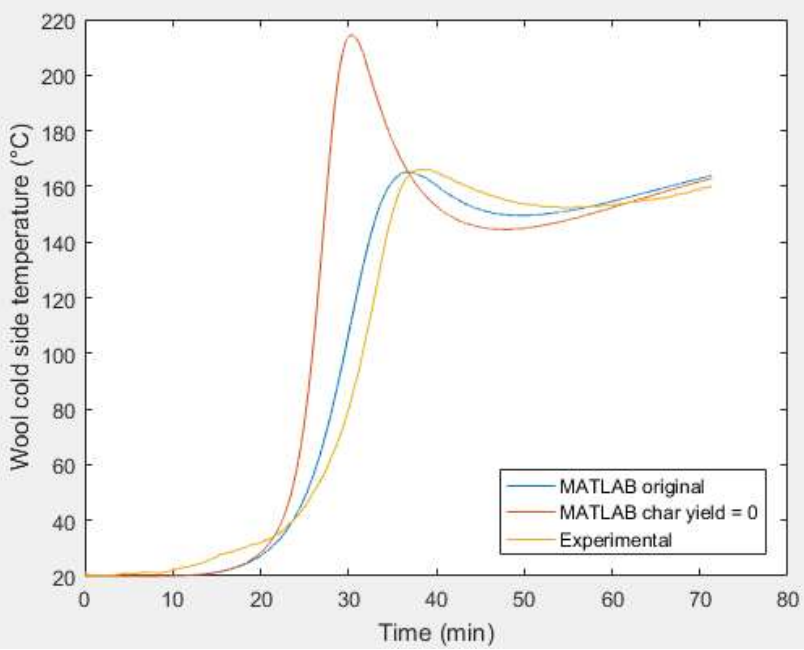

Figure 54. MATLAB simulation of wool 15 with char yield set to zero and the original simulation with a yield of 28.3 %.

Section 5.3 tells that the wools that have neither high oil or binder content nor high density, have generally satisfactory fit. This was the case especially in the MATLAB model where the average relative error was below the rather strict 5.2 % threshold. The FDS simulations for this group have slightly higher average relative uncertainty at 5.6 % due to the sensitivity issues with respect to MATLAB model in thermal conductivity and loss on ignition.

The sensitivity analysis recognized different sensitivity to variation in thermal conductivity to be the main cause of different outputs between MATLAB and FDS models. In addition, experimental results of the wools with density of around 140 kg/m^3 show that the final temperature of simulation is constantly above the experimental. By employing the initial correlation for specific extinction coefficient developed by Partek Oy Ab, this difference was even more significant. Modifying the correlation to return higher values for extinction coefficient lowered the final simulated temperature for dense wools while not affecting others that much. Reason is that resistance to radiative heat transfer described by extinction coefficient is greatest on dense wools. However, the remaining difference in final temperatures tells that some error still persists in the correlation modified by iteration by hand.

Refractive index of fibers are another uncertain parameter affecting the radiative component of thermal conductivity. Refractive index determines largely the magnitude of the radiative component of thermal conductivity, as it affects via its second power according to Equation 19, represented below.

$$k_{rad} = \frac{16n^2\sigma T^3}{3\beta} \quad (19)$$

Equation 19 shows that the radiative component is strongly dependent of absolute temperature as it increases proportional to its third power. Since available thermal conductivity measurements by the guarded hot plate method cover temperature ranges extending at highest to 660 °C, a not well-defined refractive index causes uncertainty in effective conductivity beyond this region.

To enlighten this issue, Figure 55 presents experimentally measured thermal conductivity up to 400 °C of a wool with density of 70 kg/m^3 along with two hypothetical thermal conductivities as a function of temperature. Both of these conductivities are obtained for a hypothetical wool with a similar density of 70 kg/m^3 but another one with a refractive index of 1.1 and another with 1.35. Other structural parameters of the wool are adjusted within realistic limits so that conductivities with both refractive indexes correspond to experimental measurement. At higher temperatures, differing indexes of refraction cause difference in thermal conductivities towards increasing temperatures.

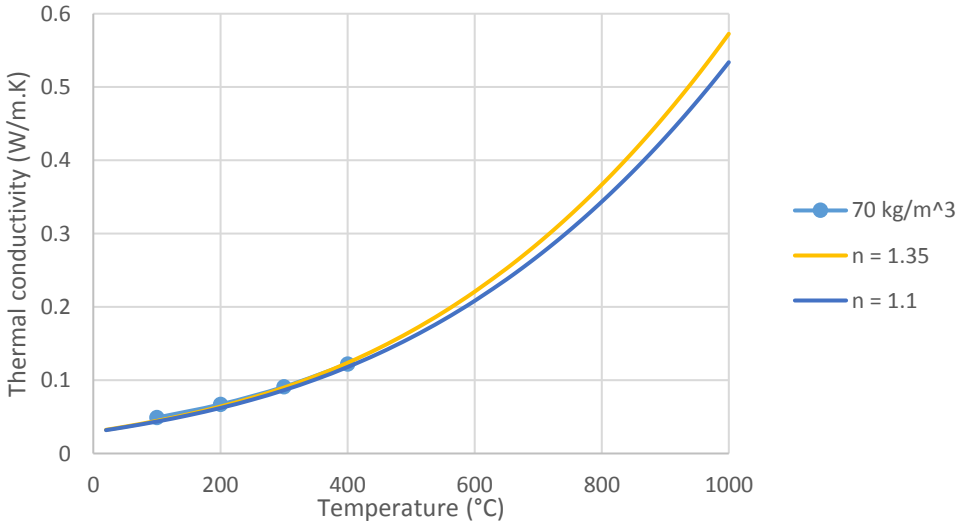

Figure 55. Experimentally measured thermal conductivity of a 70 kg/m^3 wool and two hypothetical conductivities with refractive indexes of 1.35 and 1.1 as a function of temperature.

To obtain a valid model for effective thermal conductivity, the recommended action is to experimentally measure thermal conductivity of a wool with well-known structural parameters and to update the correlation for specific extinction coefficient. When the effect of other constituents into effective thermal conductivity is well defined, refractive index could be iterated so that conductivity predicted by the model corresponds to experimental measurements.

Section 4.6 mentions and Annex B2 further discusses that one of the main weaknesses of the FDS model is its disability to assign different convective heat transfer coefficients into different sides of the slab. In the MATLAB model convective heat transfer coefficient on the hot side is set to 25 $\frac{\mathrm{W}}{\mathrm{m^2K}}$ according to Eurocode 1 (European Committee for Standardization, 2002). In the FDS model the hot side follows the same correlation for convective heat transfer coefficient as the cold side. This leads to weakened convective heat transfer between the steel sheet and furnace and to lowered temperatures in the beginning of the simulation before radiative heat transfer becomes the dominant mechanism. Figure 56 shows steel sheet temperatures during a MATLAB and FDS simulation. The figure contains the furnace gas temperature as a reference.

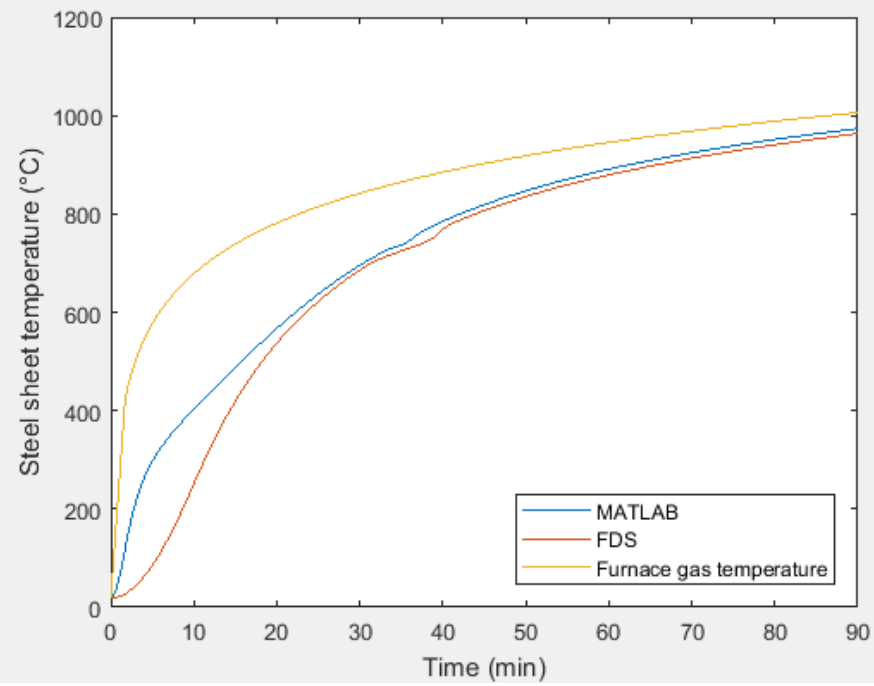

Figure 56. Steel sheet temperatures in a MATLAB and FDS simulation as a function of time compared to gas temperature inside the furnace.

In many wools the heat released by decomposition reactions is adequate to cause the temperature rise to occur simultaneously in FDS and MATLAB models. Larger differences are noted only on wools with low losses on ignition, wool 20 with a loss on ignition of only 0.7 wt-% acting as an example. Figure 57 presents its MATLAB and FDS simulations compared to the experimental measurement. The figure contains additionally a MATLAB simulation where the steel sheet and cold surface are set to follow identical correlations for convective heat transfer coefficient, as in FDS. The simulation results prove that the observed difference between MATLAB and FDS simulations in the starting points of temperature rise on the cold side is caused by different determination of convection on the hot side. After modifying the convection on the hot side in the MATLAB model, simulations are in significantly better agreement.

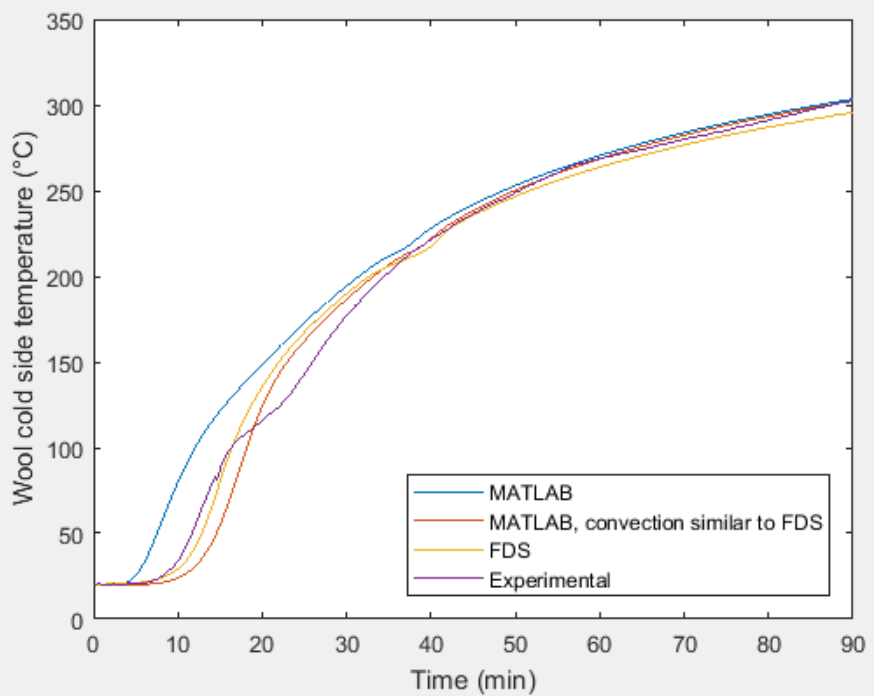

Figure 57. MATLAB and FDS simulations of wool 20 compared to experimental measurement along with a MATLAB simulation where the convection on steel sheet is determined according to the same correlation as on the cold side.

Even though the MATLAB simulation fits now better to the experimental measurement, the higher convective heat transfer coefficient of 25 $\frac{\mathrm{W}}{\mathrm{m^2K}}$ is still considered to correspond better to reality. The gas space of furnace could be assumed very turbulent, thus increasing convection. Therefore, coefficient returned by a correlation describing natural convection is clearly an underestimation.

Another clear difference between the models is FDS systematically predicting better the wools with very high loss on ignition, albeit with still poor accuracy as Table 8 shows. For example, Figure 53 shows that the MATLAB model releases all of the heat in a very tall and sharp peak whereas the behavior of the FDS model is slightly more moderate. The same applies for all other wools in the same category. One suspected reason was the much larger grid cell count in FDS, its value being 1000 compared to computationally sensible level of just some tens in the MATLAB model. Therefore, its cell spacing was reduced to same level as in the MATLAB model to test whether the better spatial resolution of FDS would be the cause of the difference. However, no difference is noted with respect to simulations with the original spacing. Therefore, the exact reason for this behavior remains unknown under the time restrictions of this thesis, although faster kinetics in the MATLAB model proven by Figure 25 would be a likely cause. Lower steel sheet temperature in the beginning of a simulation is proven not to be enough to cause this effect.

Determination or even estimation of the possible location of the limits of validity for each wool parameter is impossible based on the current group of examined wools. Fit of simulations of dense wools might be improved if issues in thermal conductivity are addressed to, and same applies with wools with high binder and oil contents on reaction kinetics. It is probable that at least the fit of wool 15 with a loss on ignition of 2.1 wt-% is possible to be made precise by implementation of an oxygen mass transfer limited kinetic scheme. However, wool 28 has the next-highest LOI of 4.7 wt-% in the experimental data set, which is already enough to cause unstable behavior. In addition, there are no wools with densities between 100 and 140 kg/m^3. It is impossible to judge if the limits of validity for both of these quantities lie within these ranges, due to wools lacking inside them. The limit of validity for oil content is considered to be at 0.25 wt-% in the current kinetic scheme. Wool 8 has this content and low relative uncertainties of 3.8 % and 4.1 % in MATLAB and in FDS models, respectively, and follows well experimental measurements. Local deviations of simulated temperature from experimental measurements become already too large in wool 17 whose oil content is 0.27 wt-%.

Even with the revised kinetic scheme, wools with high binder contents will remain outside the limits of validity by a great certainty because of extensive shrinkage of the slab thickness during a fire test. In high-binder wools the shrinkage could be even 40 % from the initial thickness, as the case is for example with wools 23 and 24, which both have a LOI in the order of 10 wt-%. Shrinkage extends from the surface of the wool slab that is attached to the metal sheet. Figure 58, a photograph of wool 24 after a fire test, illustrates this.

Figure 58. A photograph of wool 24 after a fire test.

The most notable effect of extensive shrinkage is that when temperature is stabilized after the heat release peak, simulated temperature stays below experimental by a notable amount. Loss on ignition of 4.7 wt-% on wool 28 is already enough to give rise to this effect, as Figure 59 shows. The figure depicts simulations of wool 28 compared against experimental temperature measurement.

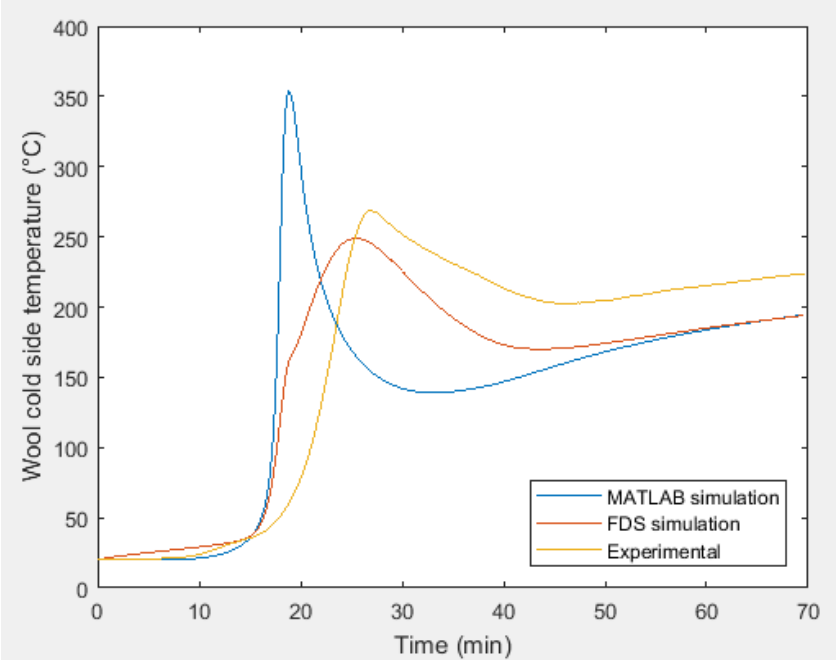

Figure 59. MATLAB and FDS simulations of wool 28 compared to experimental measurement.

As a conclusion, loss on ignition at least upwards from the order of 5 wt-% renders the fire test behavior of a wool nearly impossible to predict accurately by any practical model. Extent of shrinkage is hard to predict, since in wool 30 with similar LOI of 4.8 wt-% this effect is not observable. Taking shrinkage into account would require modelling of convection inside the increasing gap between the metal sheet and wool slab. Effect of shrinkage is negligible for other wools as it is generally in order of few percents.

5.5.4 Two-dimensional model

A validation process is not carried out for the two-dimensional model, since only two series of experimental data for large scale fire tests are available. Additionally, the employed three-dimensional temperature solver of FDS in beta phase has some limitations. The pyrolysis model to describe exothermic reactions is not yet connected to the three-dimensional solver. Therefore, evaluation of the effect of organic fraction decomposition is impossible. Since convection inside a wool slab is assumed to be different in small and large scale fire tests, apparent kinetic parameters for these two set-ups will probably be different.

Figures 60 and 61 present experimentally measured average temperatures in a large scale fire test for wools 25 and 27, respectively. Both figures include the corresponding computational surface temperature from a two-dimensional simulation as a function of time.

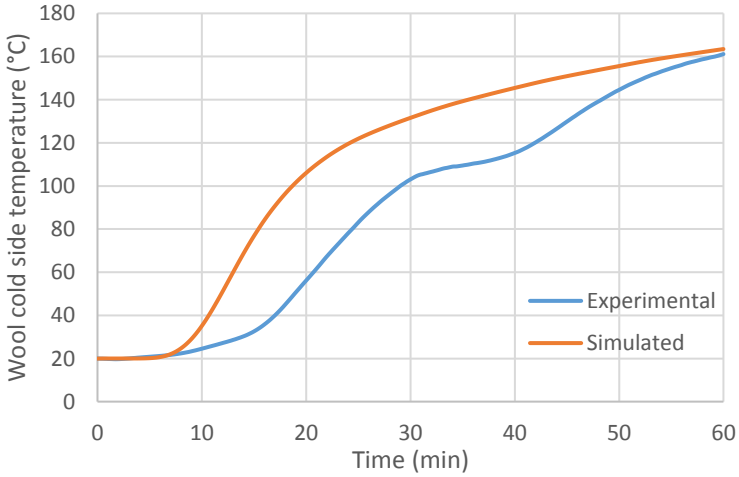

Figure 60. Measured average cold side temperature in a large scale fire test of wool 25 compared to simulated temperature as functions of time.

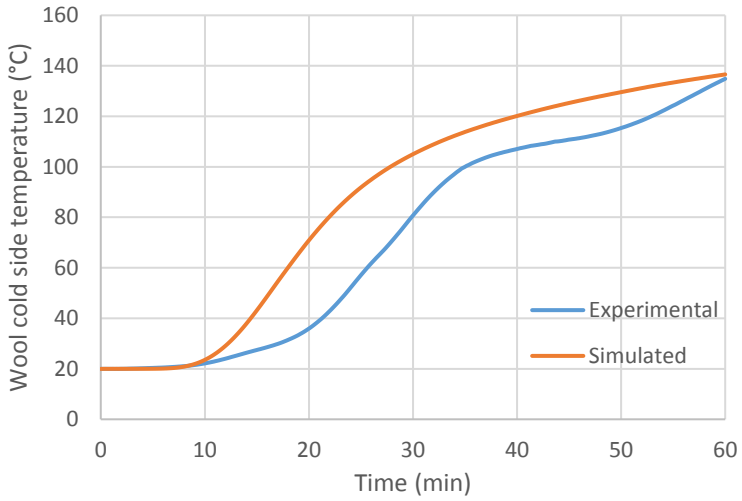

Figure 61. Measured average cold side temperature in a large scale fire test of wool 27 compared to simulated temperature as functions of time.

The previous figures reveal that simulated temperature starts rising too early and does not meet the experimental temperature until the end of a simulation. Too sharp temperature rise leads to suspect that the assumption on hot surface of the steel sheet directly following the ISO 834-1 fire curve is not realistic. Large scale furnaces are controlled by plate thermoelements whose average measurement results correspond to the fire curve with good precision, even from the beginning of the experiment. Delay before the ISO 834-1 curve is approached is in order of one minute or even less in the experimental data of the wools above. Measurement points of these elements are attached to the sheet, but it seems likely that instead they measure temperature of gas phase close to the sheet. Therefore, surface temperature of the steel sheet itself would be notably below the fire curve in the beginning of an experiment. To obtain realistic simulation results, a similar simulated furnace should be implemented also into the two-dimensional model as in the one-dimensional model. However, after several trials it was concluded that heat transfer from gaseous to solid phase is not yet possible in the current version of three-dimensional solver, making implementation of such furnace impossible. Heat transfer does however work the other way around, by adjusting the convective heat transfer coefficient it is possible to match simulated and experimental final temperatures of both experiments.

Both experimental cold side temperature measurements show a dip in temperature development approximately at 40 minutes. Its cause was previously unknown but results from one-dimensional simulations lead to suspect the reason to be a sudden momentary increase in specific heat capacity of carbon steel, the material of steel sheet. This increase occurs at a bit over 700 °C according to Figure 62, which presents specific heat capacity of carbon steel as a function of temperature.

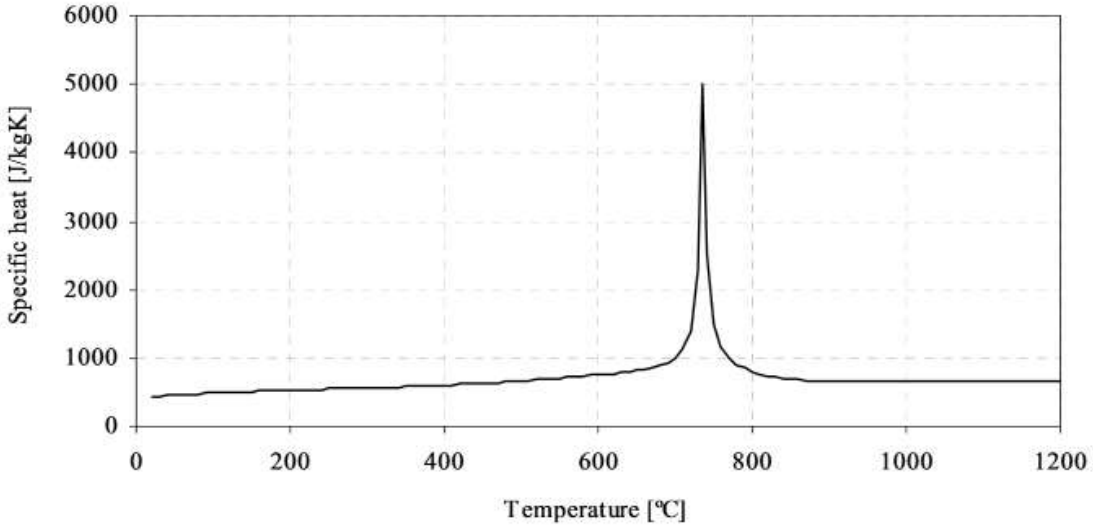

Figure 62. Specific heat capacity of carbon steel as a function of temperature (Franssen and Real, 2010).

As this sudden increase in specific heat capacity hinders temperature rise in wool, in many one-dimensional simulations is visible a tiny momentary drop in cold side temperature approximately at this aforementioned 40 minutes. The FDS model is observed to be slightly more sensitive to this effect. For example, in Figure 63 presenting the one-dimensional simulations of wool 25 with 1 mm sheet, temperature drop is larger in FDS than in MATLAB where it is barely visible. One-dimensional simulations of wool 25 were repeated by increasing the steel sheet thickness to 4.5 mm, corresponding to the large scale fire test. Figure 63 presents also these simulations. The figure shows that an increase in the steel sheet thickness to 4.5 mm causes the temperature drop to be much larger, thus supporting the hypothesis on rise in the specific heat capacity of steel causing the observed temperature drop. Further examination is however needed to prove this hypothesis, and would require at least a validated simulation model of a large scale fire test.

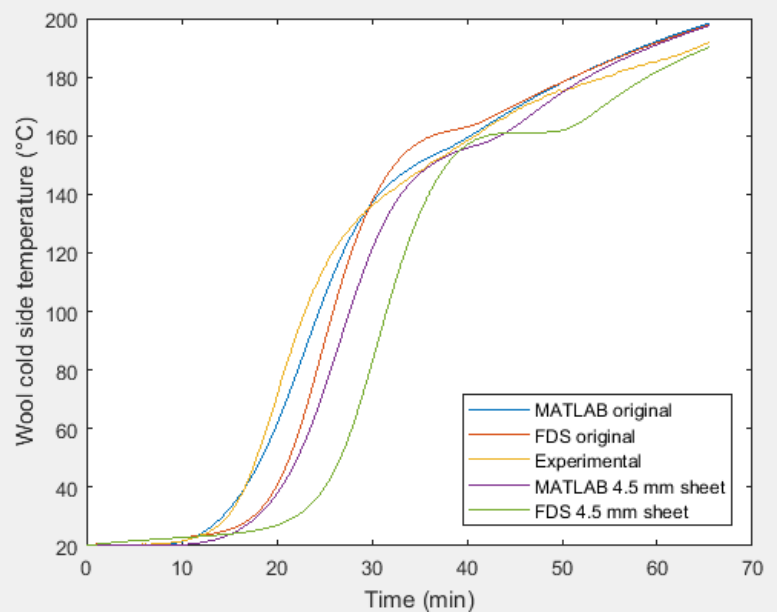

Figure 63. MATLAB and FDS simulations of wool 25 with experimental measurement, along with simulations carried out with 4.5 mm thick steel sheet.

Observed higher sensitivity of the FDS model to thickening of the steel sheet is caused by the steel sheet temperature being lower in FDS than in MATLAB model over the whole simulation, as proved by Figure 64. Differences between the models in convective heat transfer discussed in Subsection 5.5.3 explain this behavior.

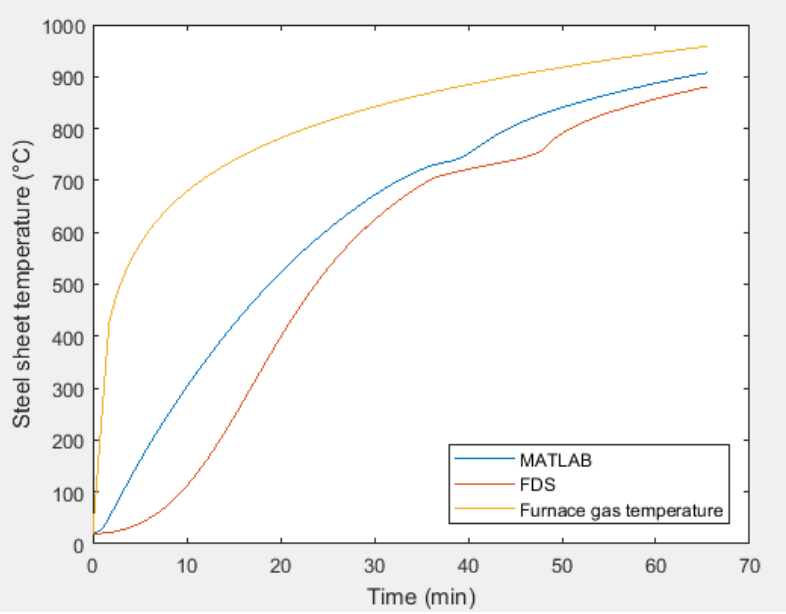

Figure 64. Steel sheet temperatures as a function of time in MATLAB and FDS simulations with steel sheet thickness of 4.5 mm.

6 Conclusions

The goal of this thesis was to build a validated numerical simulation model to predict behavior of stone wool in fire resistance tests. To reach this goal, kinetic and physical parameters were either found out experimentally or from literature. Initial values of kinetic parameters were solved thermoanalytically and then fitted iteratively to experimental data. Thermal conductivity and specific heat capacity for each material found in literature were compared to possible experimental measurements. The radiative component of thermal conductivity was fitted to the measured thermal conductivity. Finally, the convective heat transfer coefficient was fitted so that simulated and experimental final temperatures agreed.

A validation process was carried out for the models with implemented decomposition reaction schemes created in this work. Validation revealed that average relative uncertainties were low for one dimensional MATLAB and FDS models on low density wools with small combustible fractions, 4.3 % and 5.6 %, respectively. Problems arose when binder or oil contents or density were increased. Average relative uncertainties of simulations of wools rich in oil were not high, less than 4 % in the both models. However, the overall quality of fit was considered poor due to excessively high momentary temperature peaks. High binder content caused similar problems, but now also the average relative uncertainty increased into the order of tens of percents in the both models. The uncertainty for dense wools in the FDS model was noticeably larger at 11 % compared to the MATLAB model at 6.0 %. The limit of validity with respect to the oil content could be considered to be 0.25 wt-% for the current model. Such limit is however impossible to define for binder content or density based on the experimental data set at hand.

A hypothetical reason for observed uncertainties associated with large combustible fractions is the erroneous assumption on plentifully available air for combustion, supplied by internal convection inside the wool. Therefore, the kinetic scheme does not take into account the availability of oxygen, which is certainly a limiting factor in combustion reactions inside the wool. This leads into unrealistically rapid and excessive temperature rise especially in the wools with large loss on ignition.

Another major source of uncertainty in the model is the radiative component of thermal conductivity. Its uncertainty is most pronounced in dense wools. The systematic overprediction of final temperatures on these wools hints that errors remain in the modified specific extinction coefficient correlation.

The most important part of future work is the formulation of an oxygen mass transfer –limited kinetic scheme for organic fraction decomposition. A good starting point for redefining the kinetic scheme would be thermoanalytical measurements of wools impregnated with binder. Thus, mass transfer conditions on a binder particle in the measured sample would correspond to real wool as well as possible. Afterwards a term describing oxygen depletion and migration should be implemented, or even a different kinetic equation altogether if necessary. Also, wool solid phase reactions are still not well known. The most significant of them are suspected to be oxidation and crystallization. To obtain their heats of reaction and kinetic parameters, analyses of inorganic fraction of a wool with a well-calibrated DSC-apparatus with several heating rates is necessary. After this, implementation of solid phase reactions back into the model should be considered.

Reaction kinetics under oxygen-free conditions could be one possible point of future research. For example, inside a ship fire barrier the amount of air is limited (Nurmi, 2016). Therefore, if the model is applied in simulation of such structures, reactions inside wool in an oxygen-free atmosphere could become a relevant research problem.

To obtain a more precise effective thermal conductivity model, high temperature thermal conductivity of wools with known material parameters should be measured. This is ongoing at the moment of finishing of this thesis. After these measurements and the formulation of a new correlation for specific extinction coefficient, the refractive index of fibers could be fitted so that the computational conductivity corresponds to experimentally measured.

Sensitivity analysis revealed that the main cause behind the observed differences between MATLAB and FDS models are their different sensitivities to changes in thermal conductivity. This results directly to different sensitivities to amount of combustible content, the main reason behind the observed differences between the MATLAB and FDS models. After kinetic and thermal conductivity models are updated, it might be possible to judge which model corresponds better to reality.

Figure 25 in Section 5.1 proves that some differences exist between the reaction models built in MATLAB and FDS. The observed difference could be corrected by adjusting reaction parameters separately for each model. However, other possible undetected differences in the reaction models could explain differences in fitted kinetic parameters and in responses to increases in combustible fraction. To

compare progress of reactions between the models, a device output to measure mass concentration of a component inside a solid would be a helpful addition into FDS.

As a need for further improvement in the solid heat transfer module of FDS arose the need for determination of different convective heat transfer coefficients for inner and outer surfaces of a mesh boundary. This restricts the versatility of the program in constructing different scenarios where it would be desired to use a certain constant convective heat transfer coefficient, such as the one suggested by Eurocode 1, on one side and a correlation for natural convection on another.

In the current FDS version, binder and oil combustion could be described just in terms of their mass concentration and Arrhenius parameters. Taking oxygen mass transfer limitations into account inside a solid phase in FDS during combustion would require implementing a model for porous materials and air permeability.

At the moment it is impossible to make a valid two-dimensional model of large scale fire tests utilizing the three-dimensional thermal conductivity solver of FDS. Development of the simulation model is now hindered by the beta-phase issues, which do not allow for neither solid phase reactions nor convective transfer from gaseous to solid phase.

References

American Society of Heating, Refrigerating and Air-Conditioning Engineers, 2013. Physical Properties of Materials. *2013 ASHRAE Handbook - Fundamentals (SI Edition).* Atlanta: American Society of Heating, Refrigerating and Air-Conditioning Engineers, Inc., pp. 33.1-33.4.

Andersen, F.M.B. and Dyrbøl, S., 1998. MODELLING RADIATIVE HEAT TRANSFER IN FIBROUS MATERIALS: THE USE OF PLANCK MEAN PROPERTIES COMPARED TO SPECTRAL AND FLUX-WEIGHTED PROPERTIES. *Journal of Quantitative Spectroscopy and Radiative Transfer,* **60**(4), pp. 593-603.

Asllanaj, F., Milandri, A., Jeandel, G. and Roche, J.R., 2002. A finite difference solution of non-linear systems of radiative-conductive heat transfer equations. *International Journal for Numerical Methods in Engineering,* **54**(11), pp. 1649-1668.

Baird, D.C., 1962. The Propagation of Uncertainties. *Experimentation: An Introduction to Measurement Theory and Design.* Englewood Cliffs: Prentice-Hall, pp. 48-74.

Bankvall, C.G, 1972. *Heat transfer in fibrous materials.* Stockholm: National Swedish Building Research.

Buratti, C., Moretti, E., Belloni, E. and Agosti, F., 2014. Development of innovative aerogel based plasters: Preliminary thermal and acoustic performance evaluation. *Sustainability,* **6**(9), pp. 5839-5852.

Buska, A. and Mačiulaitis, R., 2007. The compressive strength properties of mineral wool slabs: Influence of structure anisotropy and methodical factors. *Journal of Civil Engineering and Management,* **13**(2), pp. 97-106.

Buska, A., Mačiulaitis, R. and Rudžionis, Ž., 2015. New method for determination of mineral wool products macrostructure. *Medziagotyra,* **21**(2), pp. 303-308.

Cengel, Y.A., 2003. Numerical Methods In Heat Conduction. *Heat Transfer - A Practical Approach.* 2nd edn. New York: McGraw-Hill, pp. 265-331.

Chapelle, L., Brøndsted, P., Kusano, Y. and Foldschack, M.R., 2014. Microstructural characterization of stone wool fibre network, *16th European Conference on Composite Materials, ECCM 2014*, 22-26.6.2014.

Danish Institute of Fire and Security Technology, EN 1363-1, [Online]. Available: http://www.dbi-net.dk/media/en%201363-1%20general%20requirements.pdf, obtained 23.2.2017.

Das, A.K., 2014. Fire Science for the Built Environment. *Principles of Fire Safety Engineering: Understanding Fire and Fire Protection.* Delhi: PHI Learning, pp. 67-84.

Dixon, J.C., 2007. Appendix B: Properties of Air. *The Shock Absorber Handbook.* 2nd edn. Chichester: John Wiley & Sons, Ltd, pp. 375-378.

Drysdale, D., 2011. Heat Transfer. *An Introduction to Fire Dynamics.* 3rd edn. Chichester: John Wiley & Sons, Ltd, pp. 35-82.

Ellison, S.L.R., Barwick, V.J. and Farrant, T.J.D., 2009. Appendix A: Statistical Tables. *Practical Statistics for the Analytical Scientist.* 2nd edn. Cambridge: The Royal Society of Chemistry, pp. 205-215.

European Committee for Standardization, 2002. *EN 1991-1-2: Eurocode 1: Actions on structures - Part 1-2: General actions - Actions on structures exposed to fire.* Brussels: European Committee for Standardization.

Finnish Standards Association, 2000. *SFS-EN 1363-1: Fire resistance tests. Part 1: General requirements*. Helsinki: Finnish Standards Association.

Franssen, J. and Real, P.V., 2010. Annex A: Thermal Data for Carbon Steel and Stainless Steel Sections. *Fire Design of Steel Structures.* Brussels: European Convention for Constructional Steelwork, pp. 319-345.

Futschik, M.W. and Witte, L.,C, 1993. Models of Conductive Heat Transfer. *Technical Report: Analysis of Effective Thermal Conductivity of Fibrous Materials.* NASA, pp. 4-22.

Grinchuk, P.S., 2014. Contact heat conductivity under conditions of high-temperature heat transfer in fibrous heat-insulating materials. *Journal of Engineering Physics and Thermophysics,* **87**(2), pp. 481-488.

Hahn, B.H and Valentine, D.T., 2017. Introduction. *Essential MATLAB for Engineers and Scientists.* 6th edn. Cambridge: Elsevier, pp. 3-31.

Hofmeister, A.M., Sehlke, A., Avard, G., Bollasina, A.J., Robert, G. and Whittington, A.G., 2016. Transport properties of glassy and molten lavas as a function of temperature and composition. *Journal of Volcanology and Geothermal Research,* **327**, pp. 330-348.

Hu, X.F, Lie, T.T., Polomark, G.M. and MacLaurin, J.W., 1993. Figure 5. Specific Heat of Fire Brick as a Function of Temperature. *Thermal Properties of Building Materials at Elevated Temperatures.* Ottawa: National Research Council Canada, p. 11.

Imakoma, H., Sang, K. and Okazaki, M., 1990. Effective thermal conductivity of fibrous insulations. *International chemical engineering,* **30**(4), pp. 738-746.

Jensen, C. and Raspet, R., 2010. Thermoacoustic properties of fibrous materials. *Journal of the Acoustical Society of America,* **127**(6), pp. 3470-3484.
Jørgensen, O., Bye, E., Sahle, W. and Tossavainen, A., 1994. *Fibre Alternatives to Asbestos in the Nordic Countries.* Copenhagen: Nordic Council of Ministers, p. 22.

Karamanos, A., Papadopoulos, A. and Anastaselos, D., 2004. Heat transfer phenomena in fibrous insulating materials, *IASME / WSEAS International Conference on Heat and Mass Transfer*, 17-19.8.2004.

Keskinen, K.I., 1989. *Kemian laitetekniikan taulukoita ja piirroksia (in Finnish).* Espoo: Otatieto.

Kissinger, H.E., 1957. Reaction Kinetics in Differential Thermal Analysis. *Analytical Chemistry,* **29**(11), pp. 1702-1706.

Lee, S.C., 1989. Effect of fiber orientation on thermal radiation in fibrous media. *International Journal of Heat and Mass Transfer,* **32**(2), pp. 311-319.

Linford, R.M.F., Schmitt, R.J. and Hughes, T.A., 1974. Radiative Contribution to the Thermal Conductivity of Fibrous Insulations. *Heat Transmission Measurements in Thermal Insulations.* Ed. Tye, R.P., Philadelphia: American Society for Testing and Materials, pp. 68-84.

Livkiss, K., Andres, B., Johansson, N. and van Hees, P., 2017. Uncertainties in modelling heat transfer in fire resistance tests: A case study of stone wool sandwich panels. *Fire and Materials*, article in press.

Lyon, R.E., Safronava, N. and Oztekin, E., 2011. A Simple Method for Determining Kinetic Parameters for Materials in Fire Models. *Fire Safety Science,* **10**, pp. 765-777.

McGrattan, K., McDermott, R., Mell, W., Forney, G., Floyd, J., Hostikka, S. and Matala, A., 2010. Modeling the burning of complicated objects using lagrangian particles, *Interflam 2010*, 5-7.7.2010, pp. 743-753.

McGrattan, K., McDermott, R., Floyd, J., Hostikka, S., Forney, G. and Baum, H., 2012. Computational fluid dynamics modelling of fire. *International Journal of Computational Fluid Dynamics,* **26**(6-8), pp. 349-361.

McGrattan, K., Hostikka, S., McDermott, R., Floyd, J., Weinschenk, C. and Overholt, K., 2016. *Fire Dynamics Simulator User's Guide.* 6th edn. Gaithersburg and Espoo: National Institute of Standards and Technology and VTT Technical Research Centre of Finland.

McGrattan, K., Hostikka, S., McDermott, R., Floyd, J., Weinschenk, C. and Overholt, K., 2016b. Solid Phase. *Fire Dynamics Simulator Technical Reference Guide Volume 1: Mathematical Model.* Gaithersburg and Espoo: National Institute of Standards and Technology and VTT Technical Research Centre of Finland.

McGrattan, K., McDermott, R., Hostikka, S., Floyd, J. and Overholt, K., 2017. *Fire Dynamics Simulator Technical Reference Guide Volume 3: Validation.* Gaithersburg and Espoo: National Institute of Standards and Technology and VTT Technical Research Centre of Finland.

Mellin, I., 2006. Tilastollinen testaus. *Tilastolliset menetelmät (in Finnish).* Espoo: Helsinki University of Technology, pp. 129-151.

Mettler Toledo, 2010, Thermal Analysis Application No. UC 71: Measuring Specific Heat Capacity, [Online]. Available: http://www.mt.com/dam/nonindexed/po/ana/ta-applications/UC71_2016.pdf, obtained 15.3.2017.

Modest, M.F., 2013. Approximate Solution Methods for One-Dimensional Media. *Radiative Heat Transfer.* 3rd edn. Boston: Academic Press, pp. 480-494.

Mordfin, L., 2002. Table 1.5B Density of carbon steels at normal temperatures. *Handbook of Reference Data for Nondestructive Testing.* West Conshohocken: ASTM International, p. 14.

National Center for Biotechnology information, 2005, Phenol-formaldehyde resin, [Online]. Available: https://pubchem.ncbi.nlm.nih.gov/compound/24754#section=Top, obtained 25.7.2017.

Nurmi, J., 2016. *Master's thesis: Probability of fire spreading through fire barriers on a passenger ship.* Espoo: Aalto University.

Persaud, M.A., Shirvill, L.C., Gosse, A. and Evans, J.A., 1994. Emissivity Measurements of Steel Exposed to a Jet Fire, *Eurotherm Seminar on Heat Transfer in Radiating and Combusting Systems*, 5.-7.10.1994.

Peyrega, C. and Jeulin, D., 2013. Estimation of acoustic properties and of the representative volume element of random fibrous media. *Journal of Applied Physics,* **113**(10), Article no. 104901.

Pico, D., Wilms, C., Seide, G., Gries, T., Kleinholz, R. and Tiesler, H., 2012. Fibers, 12. Glass Fibers. *Ullmann's Encyclopedia of Industrial Chemistry.* Eds. Bellussi, G., Bohnet, M., Bus, J. et al., Weinheim: Wiley-VCH Verlag GmbH & Co. KGaA.

Pitkäranta, J., 2005. Numeerinen integrointi. *TKK:n Laaja matematiikka 2 (in Finnish).* Helsinki: Edita Prima, pp. 581-590.

Purkiss, J.A. and Li, L.-Y., 2014. Design of steel elements. *Fire Safety Engineering Design of Structures.* 3rd edn. Boca Raton: CRC Press, pp. 211-260.

Sadiq, H., Wong, M.B., Tashan, J., Al-Mahaidi, R. and Zhao, X.-L., 2013. Determination of steel emissivity for the temperature prediction of structural steel members in fire. *Journal of Materials in Civil Engineering,* **25**(2), pp. 167-173.

Spinnler, M.R.F., Winter, E., Viskanta, R. and Sattelmayer, T., 2004. Theoretical studies of high-temperature multilayer thermal insulations using radiation scaling. *Journal of Quantitative Spectroscopy and Radiative Transfer,* **84**(4), pp. 477-491.

Staggs, J.E.J. and Phylaktou, H.N., 2008. The effects of emissivity on the performance of steel in furnace tests. *Fire Safety Journal,* **43**(1), pp. 1-10.

Stankevičius, V., Paukštys, V., Bliudžius, R., Šadauskiene, J., Turskis, Z. and Samajauskas, R., 2013. Convection in mineral wool used as insulation for buildings. *Journal of Civil Engineering and Management,* **19**(2), pp. 296-304.

Steel Construcion Instiute, 2014. Section 1: Determination of fire load. *Design Guidance for Hydrocarbon Fires (FABIG Technical Note 13).* Ascot: Steel Construction Institute, pp. 69-75.

Stephan, K. and Laesecke, A., 1985. The Thermal Conductivity of Fluid Air. *Journal of Physical and Chemical Reference Data,* **14**, pp. 227-234.

Steponaitis, L., Vejelis, S. and Vaitkus, S., 2012. Analysis of structure and deformation mechanisms of mineral wool slabs under compression. *Medziagotyra,* **18**(2), pp. 192-196.

Sutton, I., 2015. Safety in Design. *Plant Design and Operations.* Oxford: Elsevier, pp. 194-216.

Taylor, J.R., 1997. How to Report and Use Uncertainties. *An Introduction to Error Analysis: The Study of Uncertainties in Physical Measurements.* 2nd edn. Sausalito: University Science Books, pp. 13-43.

Tleoubaev, A., 1998, Conductive and Radiative Heat Transfer in Insulators, [Online]. Available: http://www.tainstruments.com/pdf/literature/Conductive%20and%20Radiative%20Heat%20Transfer%20in%20Insulators.pdf, obtained 8.2.2017.

Tsilingiris, P.T., 2008. Thermophysical and transport properties of humid air at temperature range between 0 and 100 °C. *Energy Conversion and Management,* **49**(5), pp. 1098-1110.

Veiseh, S. and Hakkaki-Fard, A., 2009. Numerical modeling of combined radiation and conduction heat transfer in mineral wool insulations. *Heat Transfer Engineering,* **30**(6), pp. 477-486.

Warrington, S.B. and Höhne, G.W.H., 2008. Thermal Analysis and Calorimetry. *Ullmann's Encyclopedia of Industrial Chemistry.* Eds. Bellussi, G., Bohnet, M., Bus, J. et al., Weinheim: Wiley-VCH Verlag GmbH & Co. KGaA.

Williams, M., McClure, P.R., McDougal, A. and Citra, M.J., Physical and Chemical Properties. *Toxicological Profile for Synthetic Vitreous Fibers.* Atlanta: Agency for Toxic Substances and Disease Registry, pp. 165-170.

Yuen, W.W., Takara, E. and Cunnington, G., 2003. Combined Conductive/Radiative Heat Transfer in High Porosity Fibrous Insulation Materials: Theory and Experiment, *The 6th ASME-JSME Thermal Engineering Joint Conference*, 16-20.3.2003.

Zhao, J.-J., Duan, Y.-Y., Wang, X.-D. and Wang, B.-X., 2012. An analytical model for combined radiative and conductive heat transfer in fiber-loaded silica aerogels. *Journal of Non-Crystalline Solids,* **358**(10), pp. 1303-1312.

Zhao, D., Qian, X., Gu, X., Jajja, S.A. and Yang, R., 2016. Measurement Techniques for Thermal Conductivity and Interfacial Thermal Conductance of Bulk and Thin Film Materials. *Journal of Electronic Packaging, Transactions of the ASME,* **138**(4), Article no. 040802.

Annex A. MATLAB model

A1. OneD_solver_main.m

The main program file “OneD_solver_main.m” contains as a first set of variables the definitions for all wool material parameters that are measured experimentally as a routine procedure and which affect the heat transfer and release. These are the same parameters as listed in Table 1 in Section 3.1.

Simulation parameters determined in the second set include the conditions on how the simulation is run, which are the total run time, amount of discretization nodes and time step length. These include also the ambient temperature, which is 20 °C by default, thickness of the steel sheet and the height of the wool slab. No significant changes were observable in simulation output after the number of discretization nodes is set to 45, while the computational time is still kept sensible at maximum few minutes. For almost every wool the time step size of 0.2 s was adequate to result into numerically stable solution. Both time step and node count however had to be reduced for wools with very high loss on ignition or thermal conductivity, since otherwise a stable solution would not have been acquired over a reasonable time. For example, when keeping the discretization node count in its default value of 45 for highly conductive wool 20, a stable solution was obtained with a time step of 0.02 s, resulting into a computational time of approximately four hours.

Constants, such as Stefan-Boltzmann constant and universal gas constant are defined as a third set of variables. Also, some other material properties that could be assumed to be almost constant, are defined here. These include emissivities of metal and wool, char yields from binder and oil decomposition and continuous phase densities of each component present within the wool structure. Table 11 lists each parameter in these three categories.

Additionally, some unit transformations and calculation of porosity and extinction coefficient is carried out after these input parameters. Transformations are to SI-units, from mass percentages to mass fractions or from degrees to radians.

Table 11. Input parameters defined in the file OneD_solver_main.m. Global variables are marked with highlighted rows.

Parameter	Symbol in thesis nomenclature	Name in MATLAB	Input unit
Wool slab parameters			
Thickness	None	`slabthick_mm`	mm
Wool density	ρ_w	`rhowool`	kg/m^3
Loss on igniton (mass fraction of combustible organics)	None	`loi_p`	%
Oil mass fraction	x for mass fraction in general	`oilfract_p`	%
Fiber fraction	ξ	`fibrousfract_p`	%
Fiber mean diameter	D_f	`diamfiber`	µm
Fiber angle of orientation	ϕ	`fibor`	deg
Simulation parameters			
Total simulation time	None	`tmax`	min
Ambient temperature	T_0	`T0`	K
Number of discretization nodes	None	`N`	Dimensionless
Time step size	Δt	`dt`	s
Height of the wool slab	l	`l`	m
Thickness of the steel sheet	x_{sheet}	`thicksteel`	m
Constants			
Stefan-Boltzmann constant	σ	`stefbol`	$5.670367 \cdot 10^{-8}\ \frac{\mathrm{W}}{\mathrm{m^2K^4}}$
Universal gas constant	R	`R`	$8.31441\ \frac{\mathrm{J}}{\mathrm{K \cdot mol}}$

Emissivity of metal	ε_{steel}	`eps_met`	Dimensionless
Emissivity of wool	ε_{w}	`eps_wool`	Dimensionless
Binder decomposition char yield	ν_s in general	`bindchar`	Dimensionless
Oil decomposition char yield		`oilchar`	Dimensionless
Continuous phase density for fiber material	ρ_s	`rhofib`	kg/m^3
for binder	None	`rhobind`	kg/m^3
for oil	None	`rhooil`	kg/m^3
for steel	ρ_{steel}	`rhosteel`	kg/m^3

Subsequently after the parameter definitions, the main file invokes the temperature solver function stored as the file temp_solver.m. After the calculation is finished, the main file orders plotting of the selected data. They include simulated and experimental temperatures of the cold side as a function of time, temperatures of furnace gas space, furnace walls and steel sheet as a function of time, effective thermal conductivity as a function of temperature and wool temperature as a function of location and time, presented as a three-dimensional plot.

A2. temp_solver.m, eff_cond.m, heatcapa.m, steel_heatcapa.m and convcoeff.m

In addition to the temperature solver function temp_solver.m, effective thermal conductivity, specific heat capacity of wool and steel, and convective heat transfer coefficient functions eff_cond.m, heatcapa.m, steel_heatcapa and convcoeff.m are described here, as they are invoked from the temp_solver.m function.

The numerical calculation of grid cell temperatures at each time instant according to a method described in Section 4.4 is carried out in function temp_solver.m. The function takes ambient temperature, wool slab thickness, number of grid cells, time step magnitude and total simulation time as inputs. Outputs are the matrix of temperatures in each location at every time step, time and length vectors which contain elapsed simulation time at every time step and locations of disctretization nodes, respectively, and vectors of temperatures of furnace gas space, furnace walls, metal sheet and the cold side.

In the very beginning of the file, simulation time is transformed into seconds and time and length vectors are initialized according to total simulation time and wool slab thickness. Arrhenius parameters are returned by invoking function arr_param.m. As described in Section 3.3, the temperature of the gas phase in furnace increases linearly for the first 1.73 minutes of an experiment and then meets the ISO 834-1 standard curve. The slope of this region of temperature rise is defined also in initialization.

As the numerical method in this work is explicit, i.e. the desired value for the next time step is based on values of the previous time step, definition of initial conditions for the first time step is necessary. Initially, temperature is set to ambient throughout the wool slab, relative amounts of binder and oil are set to 1 and conversion of wool reactions to 0. Also, heat released by reactions for the first step is calculated in these ambient conditions by invoking the function reactheat.m, although the reaction rate is infinitesimally small in these conditions. Development over time of each quantity set in definition of initial conditions is tracked in each location within the slab with a two-coordinate system where the ordinal of the time step is denoted by i and the ordinal of grid cell counting from the hot side by n. For example, temperature at the i:th time step in the n:th cell is stated as T(i,n).

Onwards from the point marked with “EXPLICIT TIME INTEGRATION”, the explicit numerical method for calculation of temperature in each grid cell is carried out for each time step until the defined total simulation time is met. This point is identified when the for-loop inside which the implicit numerical scheme is carried out, has gone through all the time instances from 2nd time step to the final one whose ordinal is denoted as Nt. Nt is defined in the initialization phase and it equals to the length of the time vector.

Since the one millimeter thick steel sheet is obviously a thermally thin object, it is modeled as the first grid cell. Function steel_heatcapa.m determines its specific heat capacity, which is a direct implementation of the correlation presented in Subsection 3.7.7. As stated in Section 4.4, the sheet gains energy by radiation and convection from the furnace. Already at a rather early phase of the work it was noticed that the metal sheet cannot follow directly the ISO 834-1 curve, to avoid premature temperature rise on the cold side. Convective heat transfer coefficient between furnace gas space and its surroundings is set to 25 $\frac{\mathrm{W}}{\mathrm{m^2K}}$ as described in Subsection 3.7.9. Steel and furnace wall emissivities were iterated by hand, keeping in mind the range of literature values mentioned in the same subsection. The final

point of iteration was a physically sensible situation where the temperatures of both gaseous phase and furnace walls ought to be approximately the same when closing to the end of the experiment. Simultaneously, effective thickness of the furnace brick layer was iterated to give the furnace wall layer a thermal mass that results in correct shape, slope and location of the initial temperature rise in the cold side. This was achieved when emissivities of both brick and steel were 0.85 and the brick layer was 1.3 cm thick. Temperature developments of gas phase and both surfaces with aforementioned parameters are presented in Figure 65.

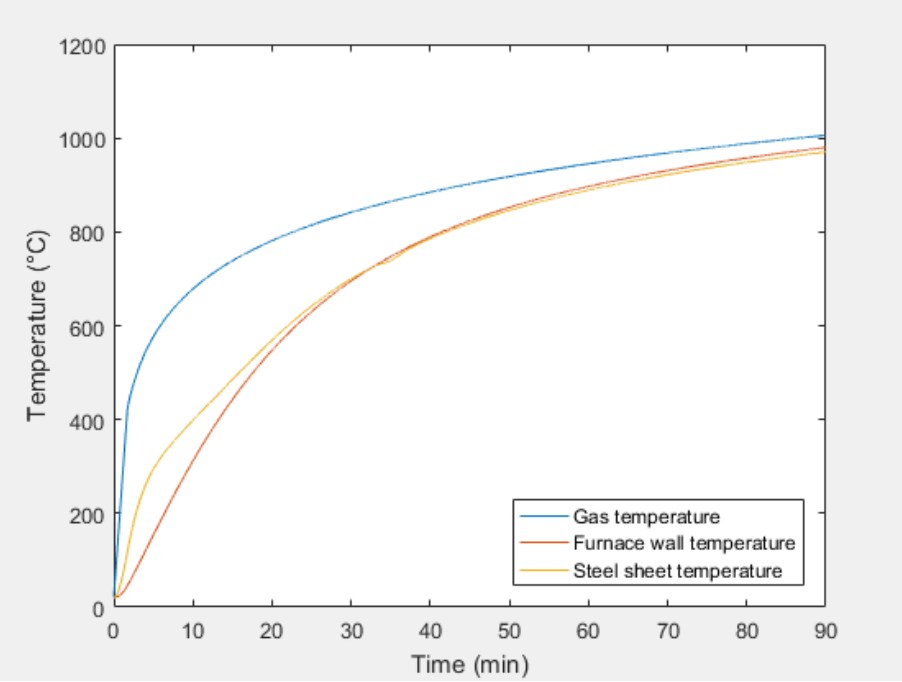

Figure 65. Temperatures of gas phase, furnace wall and separating steel sheet during a simulated fire test. Faster initial heat-up of steel sheet is explained by its specific heat capacity being lower in low temperatures.

Function eff_cond.m determines the effective thermal conductivity at cell boundaries, and specific heat capacity of wool inside the cell is defined by function heatcapa.m. Function eff_cond.m follows the procedure described in Subsection 3.7.5 and heatcapa.m the procedure described in Subsections 3.7.2, 3.7.4 and 3.7.6. Calculation of thermal conductivity at the boundary is based on average temperature of neighboring cells. As the calculation proceeds inside a for-loop from the hot to the cold side, thermal conductivity calculated for the cold side boundary of a grid cell is stored as hot side boundary thermal conductivity for the neighboring cell in the cold direction.

The expression for the final grid cell at the cold side boundary of the slab includes implementation of cold side boundary conditions which describe heat release by radiation and convection. These heat transfer mechanisms occur from cold side surface temperature which is extrapolated from the last two grid cells. Radiative heat transfer is modelled simply by the Stefan-Boltzmann law assuming a constant emissivity on 0.85 for wool. Function convcoeff.m determines convective heat transfer coefficient according to the method described in Subsection 3.7.9. Temperature of the cold boundary is largely dependent on the magnitude of convective heat transfer coefficient, so adjustment of the final temperature of the simulation is possible by modifying the defining correlation.

After the loop “for i = 2:Nt” has calculated temperatures for all grid cells for a certain time step, it checks whether binder, oil or wool reactions have reached their completion. If not, it gives relative amount or conversion for the next time step based on the previous value and reaction rate. These updated relative amounts and conversions act as inputs along with temperatures of current time step to arrive into heat release and reaction rates for the next time step by invoking function reactheat.m.

After this procedure is completed for all time steps, the function compiles determined output quantities as vectors for plotting of outputs. Finally the function carries out desired unit transformations to arrive into better suited output format.

A3. arr_param.m and reactheat.m

Arrhenius parameter and reaction heat functions arr_param.m and reactheat.m are both described here since the latter utilizes directly the first.

The function arr_param.m does not take any input arguments. Its task is only to return activation energy and pre-exponential factor for binder and oil decomposition and wool reactions when it is invoked from temp_solver.m during the initialization phase. The method to calculate kinetic parameters according to Section 3.4 is left as comments for possible future use, since it is consistent only for first order reactions. Now it only returns directly the numerical values of Arrhenius parameters which have been fitted to the experimental data.

These Arrhenius parameters act as input arguments along with temperature, relative amounts of binder and oil and conversion of wool reactions for function

reactheat.m. It returns heat release by reactions and reaction rates of each component as output arguments. The function calculates reaction rates with the well-known Arrhenius equation, presented here as Equation 65.

$$r = Ae^{-\frac{E_a}{RT}} \cdot [(1 - C)x_0]^{N_s} \quad (65)$$

where C is degree of conversion and x_0 is the initial mass fraction of binder or oil. The degree of conversion is calculated according to Equation 66.

$$C = \frac{1 - X_p}{1 - \nu_s} \quad (66)$$

where X_p is relative amount of a component (initially equal to 1) and ν_s its yield of solid residue.

This method is applied in order to suppress any reactions after X_p reaches the yield of solid residue, or C reaches unity. Decomposition rate of binder and oil are afterwards transformed to relative mass coordinates for calculation of heat released by reaction and degree of conversion for the next time step.

Rate of wool solid phase reactions follows similar expression to Equation 65, except the reaction rate is calculated entirely with respect to conversion. Therefore Equation 67 defines reaction rate of wool solid phase reactions.

$$r = Ae^{-\frac{E_a}{RT}} \cdot (1 - C_w)^{N_s} \quad (67)$$

where C_w is degree of conversion for wool solid phase reactions.

Equation 68 is employed to calculate volumetric heat release rate $\dot{Q}'''$ (HRRPUV) separately for binder, oil and wool, respectively.

$$\dot{Q}''' = \rho_w \Delta H_r x_0 r \quad (68)$$

where ρ_w is wool density and ΔH_r is the heat of reaction. It should be noted that reaction rate is here in relative mass coordinates.

Finally, the function combines HRRPUVs from all three reactions into a single value as a sum. In the current model, the fiber solid phase reactions are disabled to avoid excessive heat rise. This effective $\dot{Q}'''$ for each grid cell is the output argument of the function and acts as the source term of heat release in Equation 54.

Annex B. One-dimensional FDS model

B1. MATLAB script FDS_ramp.m

If some quantity is desired to undergo a change as a function of time or temperature in FDS, it must be implemented as a linear ramp or as a combination of them. Obviously, this applies for example for thermal conductivity and specific heat capacity. Each separate RAMP line in the input file describes a ramp turnpoint. At least two RAMP lines are required to form a functional ramp but there is no upper limit. Three RAMP lines for effective thermal conductivity from a FDS input file are presented below as an example.

&RAMP ID = 'K_RAMP', T = 20., F = 0.032655 /
&RAMP ID = 'K_RAMP', T = 100., F = 0.041708 /
&RAMP ID = 'K_RAMP', T =200., F = 0.05481 /

The ID = 'K_RAMP' identifies the ramp in question. Following two parameters T = 20. and F = 0.032655 determines that thermal conductivity of a wool equals to 0.032655 $\frac{\mathrm{W}}{\mathrm{m \cdot K}}$ at the temperature of 20 °C. The next line states that conductivity increases linearly as a function of temperature to 0.041708 $\frac{\mathrm{W}}{\mathrm{m \cdot K}}$ at 100 °C. Likewise, from there it increases linearly to 0.05481 $\frac{\mathrm{W}}{\mathrm{m \cdot K}}$ at 200 °C, and so forth.

The MATLAB script FDS_ramp.m is written to generate appropriate combination of RAMP lines for each different wool. Structural parameters of wool act as inputs in the script in a similar manner as in file OneD_solver_main.m, except quantities that are not necessary in the calculation of thermal conductivity or specific heat capacity are left out.

After the definition of necessary quantities, the script generates a vector whose elements are temperatures of ramp turnpoints. The temperatures are 20 °C, 100 °C and after that every 100 °C until 1000 °C is reached. The turnpoint temperature vector is converted to Kelvins. Then the functions eff_cond.m and heatcapa.m of the one-dimensional model are invoked, the turnpoint temperature vector acting as an input argument. These functions give effective thermal conductivity and specific heat capacity vectors whose elements correspond to those in the turnpoint temperature vector as output arguments. When the calculation is finished, the script prints the ramp turnpoint temperatures and values of thermal properties in

the MATLAB command window. According to the input format of FDS, the script converts temperatures back into degrees Celsius and specific heat capacity into units of $\frac{\mathrm{kJ}}{\mathrm{kg \cdot K}}$. The output in the MATLAB command window after running the script looks as shown below.

```
>> FDS_ramp

Thermal quantities of stone wool

          T (°C)    k (W/m.K)      Cp (kJ/kg.K)
ans =
           20       0.033616       0.99339
           100      0.042695       1.0057
           200      0.055891       1.0212
```

And so forth until 1000 °C is reached. In addition, the script calculates wool, binder and oil contents in mass fractions from percentage values, which act as inputs in the definition of wool slab. These mass fractions are available in the same command window output below the table of thermal properties.

B2. FDS input file for one-dimensional model

Different input quantities, simulation parameters and conditions, geometry of a simulation, simulation parameters and outputs are defined in a FDS input file by their respective namelist groups. The lines that are desired to be read by the program start with “&” and end with “/”. The program reads nothing that is not between these two symbols. Therefore, lines of an input file intended to be comments, are simply written without them. Deactivation of parts of an input file while not removing the part in question is possible by inserting or removing these symbols appropriately. This is particularly useful in troubleshooting.

The namelist group HEAD contains the parameter CHID which determines the name of output files. For example, if determined that CHID = ‘1d_model’, then the Smokeview output file would be “1d_model.smv” and the device output file would be “1d_model_devc.csv”.

In the namelist group TIME the parameter T_END defines the total simulation time in seconds. Setting the WALL_INCREMENT to unity enforces FDS to update temperature profile within solid objects each time step, which does not happen by default (McGrattan et al., 2016, p. 77). Also, time step is set to two seconds by defining DT = 2. to reduce simulation time. The step is noticeably longer than the 0.2 s step used generally in the MATLAB model. If necessary, FDS is able to reduce time step from this value independently during a simulation to avoid numerical instability (McGrattan et al., 2016, p. 34).

The namelist group DUMP determines by parameters DT_DEVC and DT_PROF the interval how often profile and device outputs, respectively, are updated. They both are defined to record values only every 10 seconds to keep the amount of raw output data sensible.

When calculating uncertainty against experimental results, both DT and DT_DEVC should be set to 0.6. This is the precision of time measurement in data files of fire test measurements.

The namelist group MISC contains global miscellaneous parameters that do not fit logically into other categories (McGrattan et al., 2016, p. 42). In this group setting the parameter SOLID_PHASE_ONLY to .TRUE. switches off the gas phase calculation. Gas phase calculation is not necessary here as heat transfer in the solid phase is the point of interest. Switching off the gas phase also results into significant decreases in computational time. By setting the ambient oxygen volume fraction Y_O2_INFTY to 0.01 and SUPPRESSION = .TRUE. it is ensured that FDS models no gaseous phase combustion reactions. Therefore, only reactions taking place are the ones within the solid phase specified below. The parameter ASSUMED_GAS_TEMPERATURE specifies temperature of the gaseous phase within the computational domain. Convective heat transfer from gaseous phase to furnace surfaces occurs from this temperature. Here it is set to 1006 °C, which is the temperature that the ISO 834-1 fire curve reaches at 90 minutes. Setting ASSUMED_GAS_TEMPERATURE_RAMP = ‘ISO 834-1’ defines that the gas phase temperature rises to 1006 °C following the ramp named ISO 834-1, which is specified in the bottom of the input file.

The namelist group REAC specifies the fuel for gaseous phase combustion reaction by the parameter FUEL. Here it is defined to be ‘PYROLYZATE’, which is the decomposition product of wool organic fraction. A soot yield of 0.01 is assigned for

its combustion. However, this is just a customary addition as combustion in gaseous phase is turned off as specified above.

The namelist group MESH contains parameters to define the geometry of a computational domain. Here, the geometry is defined by the computational mesh named simply 'MESH', set by its respective ID parameter. The parameter IJK defines into how many grid cells the mesh is divided in x-, y-, and z-directions, respectively. Herein a triplet of 3,1,4 is assigned as its value. Therefore, there are three cells in the x-direction, one in the y-direction and four in the z-direction. Setting the amount of grid cells in the y-direction as unity enforces FDS to carry out the calculation in only two spatial dimensions. This is one additional possible action to reduce computational time. Sextuplet XB defines the size and location of a domain. Its first and second, third and fourth and fifth and sixth elements define the start and ending points of mesh geometry in x-, y-, and z-directions in metres, respectively.

The MATL namelist group contains parameters for definition of material properties. Each material, its physical properties and reactions it undergoes should be defined separately by its respective MATL line. Material properties could be defined as constants, as is done for binder, oil and wool except for thermal conductivity and specific heat capacity. These two quantities are defined as functions of temperature according to ramps named 'K_RAMP' and 'CP_RAMP', respectively. These ramps are obtained by inserting wool material parameters into the MATLAB script FDS_ramp.m, described by Annex B1. Parameter N_REACTIONS defines the number of reactions the material undergoes, which is here equal to unity for all materials. Parameter N_S defines the reaction order. Arrhenius parameters, i.e. frequency factor and activation energy could be either defined directly by setting A(1) and E(1), respectively, where 1 is the ordinal of a reaction, or by defining REFERENCE_TEMPERATURE and PYROLYSIS_RANGE according to a method described in Section 3.4. In the FDS model the latter method is not recommended since it is consistent only for first order reactions. Kinetic parameters fitted into the MATLAB could not be imported directly to FDS but required some further adjustment. Heat of reaction is in the units of kJ/kg, the minus sign standing for exothermic reaction. Product yields are defined by parameters NU_MATL or NU_SPEC. NU_MATL defines the yield of solid residue whereas NU_SPEC correspondingly for gaseous product. Names of these products are defined by MATL_ID or SPEC_ID, respectively, and they must be defined by their respective MATL or REAC group.

An input file of one-dimensional FDS model defines thermal conductivity for both steel and brick, even though in MATLAB model they are not necessary. FDS requires it to be determined if other thermal properties are assigned as well.

Materials defined as described above, are assigned to surfaces with certain thermal boundary conditions by parameters in the SURF namelist group. Material layer thickness is also determined by SURF namelist group parameters. Here thermal boundary conditions for the outer boundary of the mesh are defined to be 'INSULATED' for the furnace wall brick layer, meaning that no heat is lost into backing, and 'VOID' for the wool slab, which means that the cold side of the slab faces always into ambient conditions. If emissivities are not defined on a SURF line, they are carried down from materials assigned for them.

Parameter HEAT_TRANSFER_COEFFICIENT determines directly a convective heat transfer coefficient. Optionally, the constant coefficient in a correlation for convective heat transfer coefficient could be modified by setting a specified value for C_HORIZONTAL or C_VERTICAL, depending on the orientation of surface. As the wool slab is here vertically oriented, the parameter C_VERTICAL is modified to 0.15. Default values are 1.52 and 1.31 for horizontal and vertical orientations, respectively (McGrattan et al., 2016, p. 70). Equation 69 presents the correlation to determine convective heat transfer coefficient in FDS.

$$h = C\left|T_g - T_w\right|^{\frac{1}{3}} \tag{69}$$

where C equals either to C_HORIZONTAL or C_VERTICAL and T_g and T_w are gas and surface temperatures, respectively.

Figure 66 shows values of convective heat transfer coefficient at the cold side as a function of wool slab cold boundary temperature in MATLAB and FDS models, returned by their respective correlations after necessary modifications. Values are obtained by assuming a gas temperature equal to the ambient value of 20 °C.

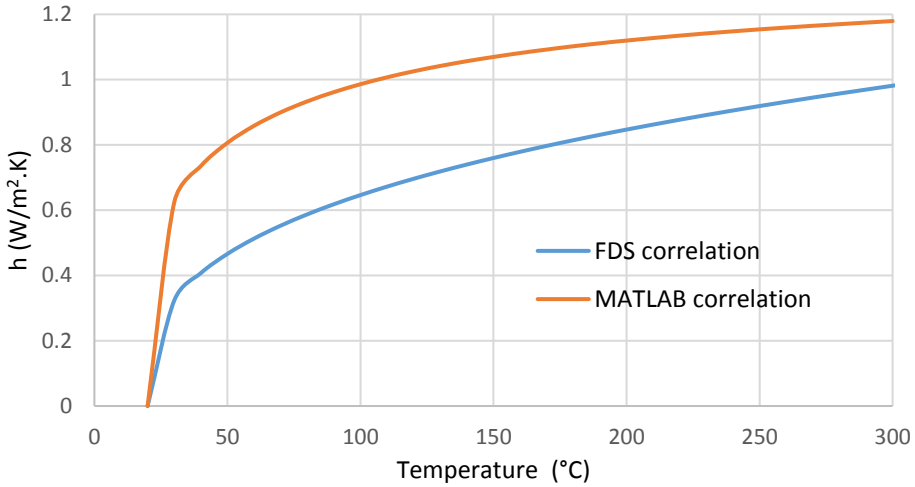

Figure 66. Values of convective heat transfer coefficient as a function of temperature in MATLAB and FDS models.

One of the main weaknesses of the FDS model is the impossibility to assign different convective heat transfer coefficient for different faces of a certain surface. This prevented application of the convective heat transfer coefficient of 25 $\frac{\mathrm{W}}{\mathrm{m^2K}}$ for the hot side of the slab, while simultaneously determining the cold side convection by Equation 69. However, as radiation becomes the dominant heat transfer mechanism in high temperatures, this difference to the MATLAB model is rather insignificant in many wools, as is discussed in Subsection 5.5.3. Differences in determination of furnace geometry and convective heat transfer on opposing sides of the slab explain different values of cold side convective heat transfer coefficient in FDS.

Material layer thickness of 0.011 m is deemed suitable for the brick layer after iteration. It differs slightly from the value of 0.013 m in the MATLAB model. The exact reason for this difference remains unknown, but its suspected causes are aforementioned differences in heat transfer and the furnace having a defined geometry in FDS, unlike in MATLAB. It is possible to assign multiple material layers for a certain surface, as is done here in the definition of the wool slab. The separating metal sheet is assigned as the first material layer in the wool slab by defining MATL_ID(1,1) = 'metal'. Likewise, the wool slab itself is determined as the second material layer as a homogenous mixture of its components by MATL_ID(2,1:3) = 'wool', 'binder', 'oil'. The properties of a slab are a weighted average obtained from mass fractions of components, determined by parameter MATL_MASS_FRACTION(2,1:3). The input for this parameter is a triplet of mass fractions of wool, binder and oil, respectively. Parameter THICKNESS defines

thicknesses of these layers. Input for this parameter is a duplet whose elements are metal sheet and wool slab thicknesses, respectively. Furthermore, in the SURF line determining the wool slab is defined STRETCH_FACTOR(2) = 2. This determines for the second material layer representing the wool slab itself the computational grid to be nonuniform in a such manner that the grid is denser towards boundaries of the slab. Also, the length scale of convection is set to 0.6 m according to the height of the slab in real experiments.

Surfaces are assigned into boundaries of the mesh geometry by parameters in the VENT namelist group. Vents could be attached either to boundaries of an obstruction or mesh. Since obstructions are not defined here, mesh boundaries remain the only possibility. The first VENT line assigns the location of the wool slab into the furnace into location defined by the sextuplet XB. Its first and second, third and fourth and fifth and sixth elements define the starting and finishing points in x-, y-, and z-directions, respectively, similarly with the mesh geometry. The brick layer is assigned to all other boundaries by the parameter MB. This parameter assigns a vent at once to a whole mesh boundary, as is done for example by determining MB = 'XMIN' which assigns it to the whole x = 0 boundary. It is noteworthy that should any vents overlap, ones defined earlier in the input file override all of the latter ones in same location. Hence, VENT defining the slab remains in place on the x = 0 boundary even though the same boundary is later on defined with another VENT to consist of brick wall by MB = 'XMIN'. Figure 67 presents the simulated geometry.

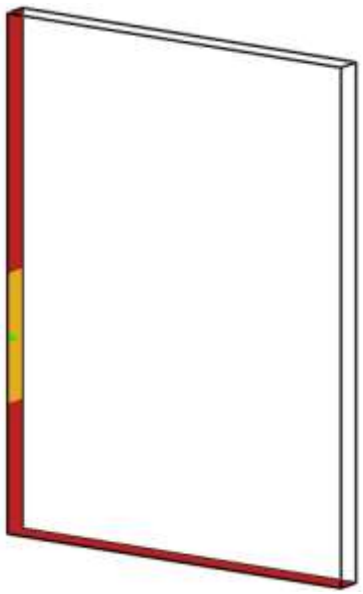

Figure 67. The geometry simulated in FDS as visualized in Smokeview. The yellow area represents the wool slab and the red area the brick layer. The green dot is the location of measurement devices.

Namelist groups BNDF, PROF and DEVC contain parameters, which define collection and visualization of simulation results. The BNDF namelist group purely contains parameters for visualization of results in the Smokeview program. Setting QUANTITY = 'WALL TEMPERATURE' on a BNDF line enables viewing of solid boundary temperatures at each time instant of simulation in Smokeview. Data recorded as defined by PROF or DEVC namelist group parameters is collected in numerical form in .csv files. In the parameters of both namelist groups the location of a measurement point is defined as a triplet of x-, y-, and z-coordinates, here assigned to the middle of the wool slab. Parameter QUANTITY defines what is being measured, IOR defines the spatial orientation of the measurement point and ID the name of the data series it produces. IOR = 1 defines the measurement point to be on a wall facing in positive x-direction, IOR = -1 in negative x-direction, and conversely for 2 and 3 in y-, and z-directions, respectively (McGrattan et al., 2016, p. 183). The PROF line in the input file determines recording of a temperature profile throughout the slab on each time instant of the simulation, whereas a DEVC line defines a point measurement that gives only one desired quantity as a function of time. Temperature profiles are located in its independent file named CHID_prof_01.csv while all of the DEVC measurements will be collected into a single file named CHID_devc.csv.

Finally, the input file determines gas temperature to follow the ISO 834-1 curve and thermal properties as a function of temperature as ramps. When defined as a ramp, a quantity changes linearly when in between of two ramp turnponts, each of which is defined by an individual RAMP line. To distinguish between separate ramps, a specific ID parameter is assigned for RAMP lines describing them. Quantities defined with ramps may change either as a function of time or temperature. Of the quantities present in this input file, the assumed gas temperature increases as a function of time according to the ISO 834-1 curve. Therefore the RAMP parameter T defines the time in seconds and F the fraction of the ramp-defined quantity from its final value, here defined as TMP_FRONT in MISC namelist group. When defined by a ramp, temperature $T(t)$ changes depending on the value of F according to Equation 70 (McGrattan et al., 2016, p. 128).

$$T(t) = T_0 + F(t)(TMP\_FRONT - T_0) \quad (70)$$

where t is time and T_0 is the initial or ambient temperature.

Thermal conductivity and specific heat capacity are instead temperature-dependent functions. Therefore on the ramps describing them T stands for temperature and F is the corresponding value in this temperature. F is in units of $\frac{\mathrm{W}}{\mathrm{m \cdot K}}$ for thermal conductivity and in $\frac{\mathrm{kJ}}{\mathrm{kg \cdot K}}$ for specific heat capacity. Ramps for thermal properties of carbon steel are from FDS input files presented in annexes of the master's thesis of Nurmi (2016). Comparison with correlations presented in Subsection 3.7.7 confirmed their truthfulness.

Generally, ramp lines should be listed with monotonically increasing values of T. If outside the specified range of the RAMP, FDS assumes the last specified value as the constant material property (McGrattan et al., 2016, pp. 127-129).

On the final row of the input file reads "&TAIL /". This has no other purpose than ensuring that FDS reads the whole file from HEAD to TAIL and enforcing the end of reading the file. It is not absolutely necessary and FDS does not even look for it. It is however advisable to attach "&TAIL /" into the end of the file as otherwise with some text editors FDS often does not read the last line due to an "end of file" character. (McGrattan et al., 2016, p. 30)

Example values in the file are from wool 7.

```
== Lines where user-defined input is required are distinguished
== with instruction "INSERT" and further information on what
== parameters should be modified.

== As a result this FDS simulation will give the temperature
== profile through the wool slab on each time instant and point
== measurement values. These outputs will be found in output
== files CHID_prof_01.csv and CHID_devc.csv.

== INSERT the desired name of output files in CHID.

&HEAD CHID = '1d_model'/


== INSERT total simulation time in seconds at T_END.
== Some common simulation times: 90 min = 5400 s, 70 min = 4200 s.

== Determines total simulation time, temperature profile update
== rate and time step magnitude.
```

```
== When calculating uncertainty against experimental measurements,
== INSERT DT = 0.6 so that the time step is equal to the precision of
== time measurement (0.01 min) in data files of experimental fire
== tests.


&TIME T_END = 5400.,
WALL_INCREMENT = 1,
DT = 2./


== Determines measurement device and profile output update interval

== When calculating uncertainty against experimental measurements,
== INSERT DT_DEVC = 0.6 so that simulation data output interval is
== equal to the precision of time measurement in data files of
== experimental fire tests.

&DUMP DT_DEVC = 10., DT_PROF = 10. /


== Defines that simulation takes place in the solid phase only and
== all gas phase combustion reactions are suppressed. Defines the
== gas phase temperature to follow the ISO 834-1 curve with initial
== temperature lag as defined in the RAMP below.

&MISC SOLID_PHASE_ONLY =.TRUE.
Y_O2_INFTY = 0.01
SUPPRESSION = .TRUE.
ASSUMED_GAS_TEMPERATURE = 1006.,
ASSUMED_GAS_TEMPERATURE_RAMP = 'ISO 834-1'/

== Defines the pyrolysis product.

&REAC FUEL = 'PYROLYZATE', C=6, H=10, O=5, SOOT_YIELD = 0.01/


== Defines the computational domain.

&MESH ID = 'MESH', IJK = 3,1,4, XB = 0.0,1.5,0,0.1,0,2 /


== INSERT wool density in kg/m^3 at DENSITY.
== NOTE THAT THE SAME WOOL DENSITY SHOULD BE APPLIED FOR BOTH
== INITIAL AND CONVERTED WOOL IF SOLID PHASE REACTION ENABLED.

== Defines properties of wool as inserted here or according to
== RAMPs below. Also determination of reaction parameters in solid
== phase. Determination of converted wool just below. Currently
== disabled since otherwise the amount of released heat would have
== been too large.
```

```
&MATL ID = 'wool',
DENSITY =  99.6,
EMISSIVITY = 0.85,
CONDUCTIVITY_RAMP = 'K_RAMP'
SPECIFIC_HEAT_RAMP = 'CP_RAMP',/ WOOL REACTIONS DISABLED
N_REACTIONS = 1,
N_S = 1.16,
A(1) = 225309,
E(1) = 184189.,
HEAT_OF_REACTION = -255.899,
NU_MATL = 1.,
MATL_ID = 'converted wool'/

MATL ID = 'converted wool',
DENSITY = INSERT SAME AS 'wool',
EMISSIVITY = 0.85,
CONDUCTIVITY_RAMP = 'K_RAMP'
SPECIFIC_HEAT_RAMP = 'CP_RAMP',/


== Determination of material properties and reaction parameters for
== organic fraction i.e. binder resin and oil.

&MATL ID = 'binder',
EMISSIVITY = 0.85,
DENSITY = 1300.,
CONDUCTIVITY = 0.2,
SPECIFIC_HEAT = 1.7
N_REACTIONS = 1,
N_S = 0.7,
E(1)=15209.,
A(1)=0.0068.,
NU_SPEC = 0.717,
SPEC_ID = 'PYROLYZATE',
NU_MATL = 0.283,
MATL_ID = 'char',
HEAT_OF_REACTION = -25000.,
ALLOW_SHRINKING = .FALSE./

&MATL ID = 'oil',
EMISSIVITY = 0.85,
CONDUCTIVITY = 0.2,
SPECIFIC_HEAT = 1.7,
DENSITY =  750.,
N_REACTIONS = 1,
N_S = 0.2,
E(1)=98992.,
A(1)=3174700.,
HEAT_OF_REACTION = -45000.,
NU_SPEC = 1.,
SPEC_ID = 'PYROLYZATE'
ALLOW_SHRINKING = .FALSE./
```

```
== Properties of solid residue 'char' of decomposition of organics.

&MATL ID = 'char',
EMISSIVITY = 1.0,
DENSITY = 120.,
CONDUCTIVITY = 0.1,
SPECIFIC_HEAT = 1.0 /

== Determination of properties for additional materials, which are
== 'metal' for metal sheet separating wool slab from furnace and
== 'brick' for the material of furnace walls.

&MATL ID = 'metal',
EMISSIVITY = 0.85,
CONDUCTIVITY_RAMP = 'KM_RAMP',
SPECIFIC_HEAT_RAMP = 'CPM_RAMP',
DENSITY = 7850./

&MATL ID = 'brick',
EMISSIVITY = 0.85,
CONDUCTIVITY = 1.,
SPECIFIC_HEAT = 0.829,
DENSITY = 1790./


== INSERT wool, binder and oil contents as mass fractions in
== MATL_MASS_FRACTION obtained with help of MATLAB script
== FDS_ramp.m. The sum of binder and oil fractions should be equal
== to measured loi and wool fraction is equal to 1-loi.

== INSERT wool slab thickness as the second number at THICKNESS,
== the first one being the metal sheet thickness.

== Determination of furnace wall and wool slab surface properties
== and their assignment accordingly into mesh boundaries as VENTs.

&SURF ID = 'WALL',
MATL_ID = 'brick',
COLOR='FIREBRICK'
HEAT_TRANSFER_COEFFICIENT = 25.,
BACKING = 'INSULATED',
THICKNESS = 0.011 /

&SURF ID = 'slab',
COLOR = 'GOLDENROD',
MATL_ID(1,1) = 'metal',
MATL_ID(2,1:3) = 'wool', 'binder', 'oil'
MATL_MASS_FRACTION(2,1:3) = 0.9887, 0.0094, 0.0019,
THICKNESS = 0.001, 0.06,
BACKING = 'VOID',
STRETCH_FACTOR(2) = 2.
CONVECTION_LENGTH_SCALE = 0.6,
C_VERTICAL = 0.15/
```

```
&VENT SURF_ID = 'slab', XB = 0.0,0.0,0.0,0.05,0.5,1. /
&VENT SURF_ID = 'WALL', MB = 'XMIN'/
&VENT SURF_ID = 'WALL', MB = 'XMAX'/
&VENT SURF_ID = 'WALL', MB = 'ZMIN'/
&VENT SURF_ID = 'WALL', MB = 'ZMAX'/


== Measurement devices to record various quantities to obtain
== results and to follow proper functionality of model. Outputs are
== available at file 1d_model.csv, except profile in its separate
== file.

Wall temperature for visualization in Smokeview.
&BNDF QUANTITY = 'WALL TEMPERATURE'/

Temperature profile through the slab during a simulation.
&PROF XYZ = 0.0,0.025,0.75, QUANTITY='TEMPERATURE', ID='temp. profile', IOR=1/

Net-, incident-, and convective heat flux and wall temperature recording on wool slab.
&DEVC XYZ = 0.0,0.025,0.75, QUANTITY = 'NET HEAT FLUX', IOR = 1, ID = 'netflux'/
&DEVC XYZ = 0.0,0.025,0.75, QUANTITY = 'INCIDENT HEAT FLUX', IOR = 1, ID='radflux'/
&DEVC XYZ = 0.0,0.025,0.75, QUANTITY = 'CONVECTIVE HEAT FLUX', IOR = 1, ID='convflux'/
&DEVC XYZ = 0.0,0.025,0.75, QUANTITY = 'WALL TEMPERATURE', IOR = 1, ID='wall temp'/
&DEVC XYZ = 0.0,0.025,0.75, QUANTITY = 'BACK WALL TEMPERATURE', IOR = 1, ID='back wall temp'/

== INSERT thermal conductivity and specific heat capacity of stone
== wool as a function of temperature into their respective RAMPs
== as obtained with the help of MATLAB script FDS_ramp.m.

== Determination of temperature development in the gas phase
== according to ISO 834-1 curve and temperature-dependent thermal
== properties as RAMPs.


== ISO 834-1 fire curve with linear initial heat-up according to experiments.
&RAMP ID = 'ISO 834-1', T = 0., F = 0. /                0 minutes
&RAMP ID = 'ISO 834-1', T = 103.8, F = 0.4099 /         1.73
&RAMP ID = 'ISO 834-1', T = 240., F = 0.5313 /          4
&RAMP ID = 'ISO 834-1', T = 360., F = 0.5914 /          6
&RAMP ID = 'ISO 834-1', T = 480., F = 0.6343 /          8
&RAMP ID = 'ISO 834-1', T = 600., F = 0.6678 /          10
&RAMP ID = 'ISO 834-1', T = 720., F = 0.6952 /          12
&RAMP ID = 'ISO 834-1', T = 960., F = 0.7385 /          16
&RAMP ID = 'ISO 834-1', T = 1200., F = 0.7722 /         20
&RAMP ID = 'ISO 834-1', T = 1800., F = 0.8335 /         30
&RAMP ID = 'ISO 834-1', T = 2400., F = 0.877 /          40
&RAMP ID = 'ISO 834-1', T = 3000., F = 0.9108 /         50
&RAMP ID = 'ISO 834-1', T = 4200., F = 0.9619 /         70
&RAMP ID = 'ISO 834-1', T = 5400., F = 1. /             90 minutes
```

```
== Stone wool thermal conductivity ramp.
&RAMP ID = 'K_RAMP', T = 20., F = 0.038716 /
&RAMP ID = 'K_RAMP', T = 100., F = 0.048121 /
&RAMP ID = 'K_RAMP', T = 200., F = 0.063025 /
&RAMP ID = 'K_RAMP', T = 300., F = 0.082456 /
&RAMP ID = 'K_RAMP', T = 400., F = 0.10751 /
&RAMP ID = 'K_RAMP', T = 500., F = 0.13923 /
&RAMP ID = 'K_RAMP', T = 600., F = 0.17864 /
&RAMP ID = 'K_RAMP', T = 700., F = 0.22671 /
&RAMP ID = 'K_RAMP', T = 800., F = 0.28441 /
&RAMP ID = 'K_RAMP', T = 900., F = 0.35268 /
&RAMP ID = 'K_RAMP', T = 1000., F = 0.43247 /
== Stone wool specific heat capacity ramp.
&RAMP ID = 'CP_RAMP', T = 20., F = 0.99453 /
&RAMP ID = 'CP_RAMP', T = 100., F = 1.0069 /
&RAMP ID = 'CP_RAMP', T = 200., F = 1.0224 /
&RAMP ID = 'CP_RAMP', T = 300., F = 1.0379 /
&RAMP ID = 'CP_RAMP', T = 400., F = 1.0535 /
&RAMP ID = 'CP_RAMP', T = 500., F = 1.069 /
&RAMP ID = 'CP_RAMP', T = 600., F = 1.0845 /
&RAMP ID = 'CP_RAMP', T = 700., F = 1.1001 /
&RAMP ID = 'CP_RAMP', T = 800., F = 1.1156 /
&RAMP ID = 'CP_RAMP', T = 900., F = 1.1311 /
&RAMP ID = 'CP_RAMP', T = 1000., F = 1.1466 /

== Metal thermal conductivity ramp.
&RAMP ID = 'KM_RAMP', T = 20., F = 54. /
&RAMP ID = 'KM_RAMP', T = 800., F = 27.3 /
&RAMP ID = 'KM_RAMP', T = 1000., F = 27.3 /

== Steel specific heat capacity ramp.
&RAMP ID = 'CPM_RAMP', T = 20., F = 0.44 /
&RAMP ID = 'CPM_RAMP', T = 700., F = 0.76 /
&RAMP ID = 'CPM_RAMP', T = 735., F = 5.0 /
&RAMP ID = 'CPM_RAMP', T = 760., F = 0.8 /
&RAMP ID = 'CPM_RAMP', T = 1000., F = 0.65 /

&TAIL /
```

Annex C. Two-dimensional FDS model

This annex discusses the implementation of the experimental set-up from large scale fire tests into the three dimensional solid heat transfer model of FDS. The three-dimensional solver is on the beta testing phase at the version 6.5.3, which is the most current one at the time of writing (McGrattan et al., 2016, p. 77). The wool slab is installed in large scale fire tests on a 3 · 3 meters steel plate which has vertical L-shaped steel profiles on regular 60 cm intervals to attach the wool slab onto the steel plate. As the structure is continuous in the direction parallel to steel profiles and repeating, implementation of a singular steel profile along with a piece of wool slab was deemed adequate for the two-dimensional model. The two-dimensional calculation is invoked in FDS by setting the number of grid cells to unity in the y-direction. This annex also presents the input file for the two-dimensional model.

Namelist groups HEAD, TIME, DUMP, MISC, TAIL and RAMP are as described already in Annex B2. Therefore, they are not discussed any more in detail here.

Figure 68 presents an example of a cross section of a wool slab along with supporting steel structures, structural dimensions being in millimetres. The geometry of the two-dimensional model is a reproduction of this structure.

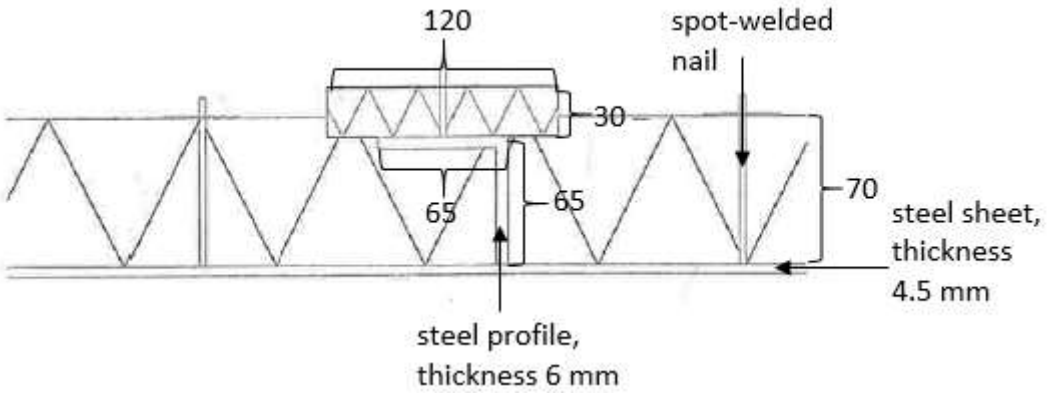

Figure 68. Structure of wool slab installation in a large scale fire test.

The namelist group MESH parameters define the computational domain as described previously in Annex B. However, now there are two preset options to be chosen from. The first mesh has a grid cell resolution of 0.005 m and the second 0.0025 m. The first option is intended for fast calculations, for example if some quantity is needed to be iterated over multiple simulation runs. The another one is

for more precise calculations, which however demands a considerably longer computational time. The justification for these resolutions is that all structural dimensions are either precisely or very closely divisible by five millimeters. For example, the steel sheet separating the slab from the furnace is 4.5 mm thick, and the steel profiles are 65 mm in width and height and consist of 6 mm thick steel. Further, for an obstruction to exist in the 3d-model it should be at least one grid cell layer thick. As a conclusion, 0.005 m, or 5 mm is the coarsest resolution which still yields sensible results. A still more precise resolution would of course aid in capturing the structures even more realistically, but the computational cost would become exceedingly high. For example, with the resolution of 0.0025 m, simulation of a one-hour experiment took already half an hour. Theoretically, computational time is inversely proportional to the third power of grid cell resolution in two-dimensional simulation, since twice as precise resolution causes twofold increase in amount of grid cells in each direction and in amount of time steps.

The solid region within which the two-dimensional thermal conduction calculation is to take place is composed of rectangular components, each denoted by its respective OBST line. Each obstacle is tied to certain material by giving MATL_ID accordingly on the OBST line. Interaction of an obstacle with the surrounding gas phase is determined by appropriate SURF line, tied to the obstacle by defining SURF_ID on the same OBST line. HT3D = .TRUE. should be written on the OBST line to invoke the three dimensional heat transfer solver. Heat is conducted from an obstacle to another according to their respective thermal properties if they are in contact with each other. Figure 69 presents the simulated geometry. Yellow region corresponds to stone wool whereas grey to steel parts. Simulated temperature measurement points above the slab are visualized here as black dots. The declared simulated cold side temperature is measured at the point furthest on the right since there the effect of the steel profile was not visible any more.

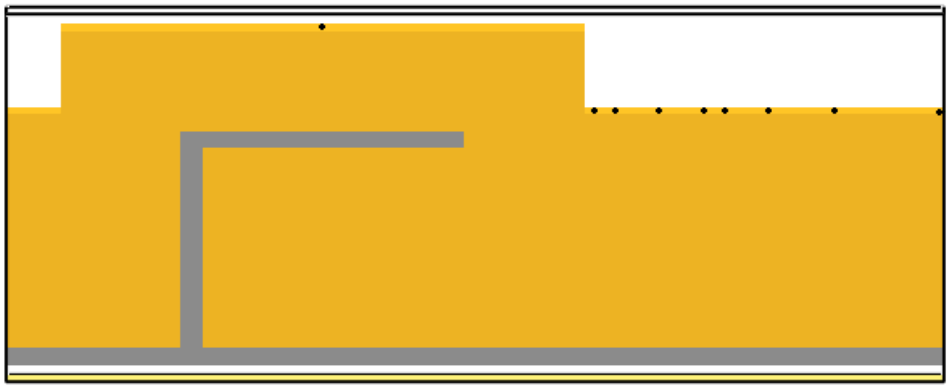

Figure 69. Simulated geometry of the 2-dimensional model.

Material properties are defined similarly by MATL lines for both wool and steel, except now reaction parameters are not defined, since the FDS pyrolysis model is not coupled to the three-dimensional conductivity solver in the beta version. Also, emissivity is now defined on the SURF line instead.

Every quantity describing heat transfer from solid to gas is now defined in the SURF lines, including emissivity and convective heat transfer properties. To achieve coupling of solid and gaseous phase in the three-dimensional model, HT3D = .TRUE. should be given also in the SURF lines. To avoid imprecise coupling between the solid surface and gaseous phase, the time step should be set on TIME line below the Von Neumann criterion. Equation 71 presents it in two dimensions (McGrattan et al., 2016, p. 77). The limits according to the criterion are 0.4 and 0.1 s for 0.005 and 0.0025 m grid cell resolutions, respectively. However, increasing the time step to two seconds causes no effect, most likely since the gaseous phase calculation is turned off on the MISC line.

$$\Delta t < \left[\frac{2k}{\rho c_p}\left(\frac{1}{\Delta x^2}+\frac{1}{\Delta y^2}\right)\right]^{-1} \tag{71}$$

Colors of obstructions are also defined by the SURF namelist group parameters. This is of some significance, since the temperature profile is observed with the slice file output in Smokeview. This output is however not visible inside of solid obstructions if they are nontransparent. All obstructions could be made completely invisible by leaving “/” after the parameter COLOR = 'INVISIBLE'. If it is desired to observe the simulated geometry instead, the slash sign after COLOR = 'INVISIBLE' should be removed from the SURF line determining both wool slab and steel parts. Their respective colors written afterwards overwrites the COLOR = 'INVISIBLE', thus making the simulated geometry visible. Further, if simultaneous observation of slice file and simulated geometry is desired, the slash sign after this latter color should be removed also, thus enabling the parameter TRANSPARENCY = 0.5, which leaves the geometry visible but transparent. An example of a slice file visualization in Smokeview during a simulation is presented in Figure 70.

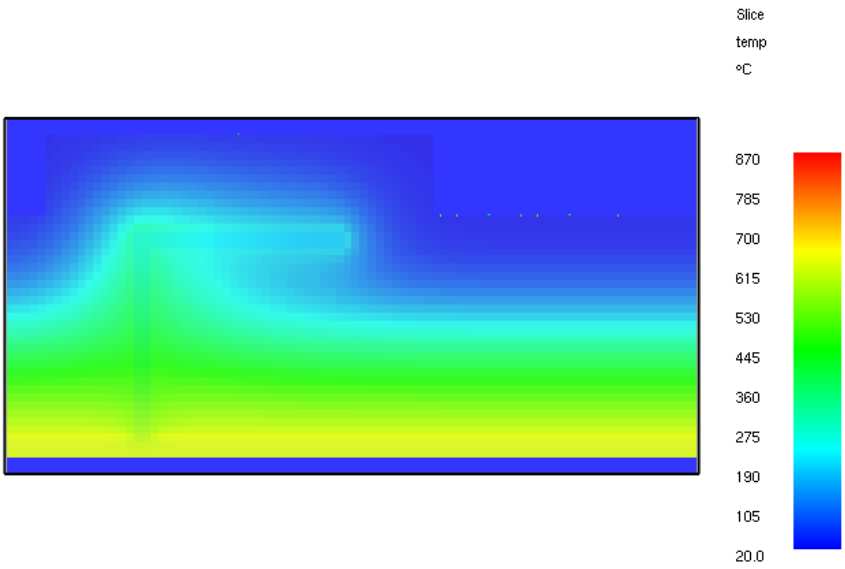

Figure 70. Visualization of temperature profile with slice file output during a 2-dimensional simulation.

The SURF line assigned with ID = 'hot surface' determines it to follow the ISO 834-1 fire curve. This surface is assigned to span the outer surface of the steel sheet with the associated VENT line, thus enforcing the hot surface of steel sheet to follow temperature development of the fire curve. This was initially deemed as reasonable approximation, since the large scale fire test furnaces are controlled with plate thermoelements. Subsection 5.5.4 however falsifies this.

Example values in the file are from wool 25.

```
== Lines where user-defined input is required are distinguished
== with instruction "INSERT" and further information on what
== parameters should be modified.

== As a result this FDS simulation will give temperature time
== series from the selected points on the slab surface and slice
== file output for examination of temperature profile inside the
== slab during a simulation.
== INSERT the desired name of output files in CHID.

&HEAD CHID = '3d_model',/


== INSERT total simulation time. The most common simulation time is
== 60 min = 3600 s in large scale fire tests.

== Determines total simulation time, temperature profile update rate
== and time step magnitude.
```

```
&TIME T_END = 3600., WALL_INCREMENT = 1., DT = 2./


== Determines measurement device output update interval.

&DUMP DT_DEVC = 10/


== Defines that simulation takes place in the solid phase only and
== all gas phase combustion reactions are suppressed. Defines the
== gas phase temperature to be equal to 20 °C.

&MISC SOLID_PHASE_ONLY = .TRUE., ASSUMED_GAS_TEMPERATURE = 20./


== Defines the computational domain. Two mesh geometries with
== different grid cell resolutions are preset as choises whether
== computational speed or precision is priority. NOTE: only one
== MESH should be active as otherwise computational performance is
== hindered.

MESH IJK = 43,1,22, XB = -0.04,0.175,0,0.0025,-0.01,0.1 /
&MESH IJK = 86,1,44, XB = -0.04,0.175,0,0.0025,-0.01,0.1 /


== Determines simulation geometry as a combination of rectangular
== elements. After each line is a description which part of the
== geometry the OBST line defines.

&OBST XB = 0.0925,0.175,0,0.0025,0,0.07,
HT3D = .TRUE., MATL_ID='wool', SURF_ID = 'wool slab' / Wool slab

&OBST XB = 0.065,0.0925,0,0.0025,0,0.065,
HT3D = .TRUE., MATL_ID='wool', SURF_ID = 'wool slab' / Wool slab right to the profile

&OBST XB = -0.0275,0,0,0.0025,0,0.065,
HT3D = .TRUE., MATL_ID='wool', SURF_ID = 'wool slab' / Wool slab left to the profile

&OBST XB = -0.04,-0.0275,0,0.0025,0,0.07,
HT3D = .TRUE., MATL_ID='wool', SURF_ID = 'wool slab' / Wool slab further to the left

&OBST XB = -0.0275,0.0925,0,0.0025,0.065,0.095,
HT3D = .TRUE., MATL_ID='wool', SURF_ID = 'wool slab' / Wool slab above the profile

&OBST XB = 0.005,0.065,0,0.0025,0,0.06,
HT3D = .TRUE., MATL_ID='wool', SURF_ID = 'wool slab' / Wool slab under the profile

&OBST XB = 0,0.065,0,0.0025,0.06,0.065,
HT3D = .TRUE., MATL_ID='metal', SURF_ID = 'steel parts' / Steel profile, horizontal part

&OBST XB = 0,0.005,0,0.0025,0,0.06,
HT3D = .TRUE., MATL_ID='metal', SURF_ID = 'steel parts' / Steel profile, vertical part

&OBST XB = -0.04,0.175,0,0.0025,-0.005,0,
HT3D = .TRUE., MATL_ID='metal', SURF_ID = 'steel parts' / Steel sheet
```

```
== INSERT wool density in kg/m^3 at DENSITY.

== Defines properties of wool as inserted here or according to
== RAMPs below. Reaction parameters are not included as at the time
== of writing the FDS pyrolysis model is not hooked up with the 3D
== conduction model.

&MATL ID = 'wool',
DENSITY = 63.9,
CONDUCTIVITY_RAMP = 'K_RAMP'
SPECIFIC_HEAT_RAMP = 'CP_RAMP'/

&MATL ID = 'metal',
CONDUCTIVITY_RAMP = 'KM_RAMP',
SPECIFIC_HEAT_RAMP = 'CPM_RAMP',
DENSITY = 7850./


== If temperatures are desired to be observed with the slice file
== output in Smokeview, then COLOR in the SURF lines should be
== switched 'INVISIBLE' or transparency should be enabled prior to
== running the simulation. Otherwise it is not possible to make the
== slice file visible. To observe the geometry of the simulation,
== remove "/" after COLOR = 'INVISIBLE' as the latter COLOR
== overwrites the previous one. Further, enabling TRANSPARENCY
== allows for simultaneous observation of geometry and slice file
== output.

== Visualization of the slice file in Smokeview: Load/Unload ->
== Slice file -> Show slice in blockage and Load/Unload ->
== Slice file -> TEMPERATURE (cell centered) -> Y=0.00125.

&SURF ID = 'wool slab',
HT3D = .TRUE.,
EMISSIVITY = 0.85,
CONVECTION_LENGTH_SCALE = 3.,
C_VERTICAL = 1.85,
C_HORIZONTAL = 1.85,
COLOR = 'INVISIBLE',
COLOR = 'GOLDENROD',
TRANSPARENCY = 0.5 /

&SURF ID = 'steel parts',
HT3D =.TRUE.,
COLOR = 'INVISIBLE',
COLOR = 'GRAY',
TRANSPARENCY = 0.5 /


== Enforces the hot surface of the steel sheet to follow the
== ISO 834-1 fire curve. The latter VENT line determines the hot
== surface to span the whole bottom of the simulated solid.
```

```
&SURF ID = 'hot surface',
COLOR = 'RED',
TMP_FRONT = 1006.
RAMP_T = 'ISO 834-1'/

&VENT XB = -0.04,0.2,0,0.0025,-0.005,-0.005, SURF_ID='hot surface'/


== Defines the top boundary of the mesh to be open into ambient.

&VENT MB='ZMAX', SURF_ID='OPEN'/


== Defines slice file output for temperature profile observation
== and temperature point measurement devices across the wool slab.

&SLCF PBY = 0.0025, QUANTITY = 'TEMPERATURE', CELL_CENTERED = .TRUE. /
&DEVC XYZ = 0.0325,0.00125,0.095, QUANTITY = 'WALL TEMPERATURE', IOR = +3, ID = 'Above steel
profile' /
&DEVC XYZ = 0.095,0.00125,0.07, QUANTITY = 'WALL TEMPERATURE', IOR = +3, ID = 'Slab next to the
profile' /
&DEVC XYZ = 0.1,0.00125,0.07, QUANTITY = 'WALL TEMPERATURE', IOR = +3, ID = '0.1' /
&DEVC XYZ = 0.11,0.00125,0.07, QUANTITY = 'WALL TEMPERATURE', IOR = +3, ID = '0.11' /
&DEVC XYZ = 0.12,0.00125,0.07, QUANTITY = 'WALL TEMPERATURE', IOR = +3, ID = '0.12' /
&DEVC XYZ = 0.125,0.00125,0.07, QUANTITY = 'WALL TEMPERATURE', IOR = +3, ID = '0.125' /
&DEVC XYZ = 0.135,0.00125,0.07, QUANTITY = 'WALL TEMPERATURE', IOR = +3, ID = '0.135' /
&DEVC XYZ = 0.150,0.00125,0.07, QUANTITY = 'WALL TEMPERATURE', IOR = +3, ID = '0.150' /
&DEVC XYZ = 0.175,0.00125,0.07, QUANTITY = 'WALL TEMPERATURE', IOR = +3, ID = '0.175' /


== INSERT thermal conductivity and specific heat capacity of stone
== wool as a function of temperature into their respective RAMPs
== as obtained with the help of MATLAB script FDS_ramp.m.

== Determination of temperature development on the hot surface of
== the metal sheet according to ISO 834-1 curve and
== temperature-dependent thermal properties as RAMPs.

== Temperature of the hot surface according to ISO 834-1 fire curve
&RAMP ID = 'ISO 834-1', T = 0., F = 0. /                0 minutes
&RAMP ID = 'ISO 834-1', T = 3., F = 0.05113 /
&RAMP ID = 'ISO 834-1', T = 6., F = 0.08932 /
&RAMP ID = 'ISO 834-1', T = 9., F = 0.1198 /
&RAMP ID = 'ISO 834-1', T = 12., F = 0.1452 /
&RAMP ID = 'ISO 834-1', T = 15., F = 0.1669 /
&RAMP ID = 'ISO 834-1', T = 30., F = 0.2446 /           0.5
&RAMP ID = 'ISO 834-1', T = 45., F = 0.2957 /
&RAMP ID = 'ISO 834-1', T = 60., F = 0.3339 /           1
&RAMP ID = 'ISO 834-1', T = 75., F = 0.3644 /
&RAMP ID = 'ISO 834-1', T = 90., F = 0.3898 /
&RAMP ID = 'ISO 834-1', T = 120., F = 0.4305 /          2
&RAMP ID = 'ISO 834-1', T = 150., F = 0.4626 /
&RAMP ID = 'ISO 834-1', T = 180., F = 0.4891 /          3
&RAMP ID = 'ISO 834-1', T = 240., F = 0.5313 /          4
&RAMP ID = 'ISO 834-1', T = 360., F = 0.5918 /          6
```

```
&RAMP ID = 'ISO 834-1', T = 480., F = 0.6343 /          8
&RAMP ID = 'ISO 834-1', T = 600., F = 0.6678 /          10
&RAMP ID = 'ISO 834-1', T = 720., F = 0.6952 /          12
&RAMP ID = 'ISO 834-1', T = 960., F = 0.7385 /          16
&RAMP ID = 'ISO 834-1', T = 1200., F = 0.7722 /         20
&RAMP ID = 'ISO 834-1', T = 1800., F = 0.8335 /         30
&RAMP ID = 'ISO 834-1', T = 2400., F = 0.877 /          40
&RAMP ID = 'ISO 834-1', T = 3000., F = 0.9108 /         50
&RAMP ID = 'ISO 834-1', T = 4200., F = 0.9619 /         70
&RAMP ID = 'ISO 834-1', T = 5400., F = 1. /             90 minutes

== Stone wool thermal conductivity ramp.
&RAMP ID = 'K_RAMP', T = 20., F = 0.034702 /
&RAMP ID = 'K_RAMP', T = 100., F = 0.047262 /
&RAMP ID = 'K_RAMP', T = 200., F = 0.067588 /
&RAMP ID = 'K_RAMP', T = 300., F = 0.094701 /
&RAMP ID = 'K_RAMP', T = 400., F = 0.13028 /
&RAMP ID = 'K_RAMP', T = 500., F = 0.17592 /
&RAMP ID = 'K_RAMP', T = 600., F = 0.23317 /
&RAMP ID = 'K_RAMP', T = 700., F = 0.30354 /
&RAMP ID = 'K_RAMP', T = 800., F = 0.3885 /
&RAMP ID = 'K_RAMP', T = 900., F = 0.48952 /
&RAMP ID = 'K_RAMP', T = 1000., F = 0.60807 /

== Stone wool specific heat capacity ramp.
&RAMP ID = 'CP_RAMP', T = 20., F = 0.99415 /
&RAMP ID = 'CP_RAMP', T = 100., F = 1.0063 /
&RAMP ID = 'CP_RAMP', T = 200., F = 1.0216 /
&RAMP ID = 'CP_RAMP', T = 300., F = 1.037 /
&RAMP ID = 'CP_RAMP', T = 400., F = 1.0524 /
&RAMP ID = 'CP_RAMP', T = 500., F = 1.0678 /
&RAMP ID = 'CP_RAMP', T = 600., F = 1.0832 /
&RAMP ID = 'CP_RAMP', T = 700., F = 1.0985 /
&RAMP ID = 'CP_RAMP', T = 800., F = 1.1139 /
&RAMP ID = 'CP_RAMP', T = 900., F = 1.1292 /
&RAMP ID = 'CP_RAMP', T = 1000., F = 1.1446 /

== Metal thermal conductivity ramp.
&RAMP ID = 'KM_RAMP', T = 20., F = 54. /
&RAMP ID = 'KM_RAMP', T = 800., F = 27.3 /
&RAMP ID = 'KM_RAMP', T = 1000., F = 27.3 /

== Steel specific heat capacity ramp.
&RAMP ID = 'CPM_RAMP', T = 20., F = 0.44 /
&RAMP ID = 'CPM_RAMP', T = 700., F = 0.76 /
&RAMP ID = 'CPM_RAMP', T = 735., F = 5.0 /
&RAMP ID = 'CPM_RAMP', T = 760., F = 0.8 /
&RAMP ID = 'CPM_RAMP', T = 1000., F = 0.65 /

&TAIL /
```

Annex D. Input file of FDS reproduction of thermogravimetric analysis of binder-oil mixture

```
&HEAD CHID='binder&oil TGA',TITLE='TGA test of wool organic fraction' /

&MESH IJK=3,1,4, XB=-2,2,-0.5,0.5,0,1 /

&TIME T_END=60. /

&REAC FUEL='pyrolyzate', C=6, H=10, O=5, SOOT_YIELD=0.01 /

&VENT XB=-1,1,-0.5,0.5,0.0,0.0, SURF_ID='SAMPLE' /

&SURF ID                    = 'SAMPLE'
TGA_ANALYSIS                = .TRUE.
TGA_HEATING_RATE            = 3.
COLOR                       = 'RED'
THICKNESS                   = 0.02
MATL_ID(1,1)                = 'binder'
MATL_ID(1,2)                = 'oil'
MATL_MASS_FRACTION(1,:)     = 0.49, 0.51/

Thermal parameters do not influence the results of a TGA test!
Heats of reaction are in kJ/kg.

&MATL ID                    = 'binder'
EMISSIVITY                  = 1.0
DENSITY                     = 1300.
CONDUCTIVITY                = 0.2
SPECIFIC_HEAT               = 1.7
HEAT_OF_REACTION            = -25.0E3
N_REACTIONS                 = 1
REFERENCE_TEMPERATURE       = 525.
PYROLYSIS_RANGE             = 222.
N_S                         = 0.7
HEATING_RATE                = 3.
NU_SPEC                     = 0.71653
SPEC_ID                     = 'pyrolyzate'
NU_MATL                     = 0.28347
MATL_ID                     = 'char' /

&MATL ID                    = 'oil'
DENSITY                     = 750.
CONDUCTIVITY                = 0.2
SPECIFIC_HEAT               = 1.7
N_REACTIONS                 = 1
REFERENCE_TEMPERATURE       = 370.
PYROLYSIS_RANGE             = 230.
N_S                         = 0.2
HEATING_RATE                = 3.
NU_SPEC                     = 1.
SPEC_ID                     = 'pyrolyzate'
NU_MATL                     = 0.
```

```
MATL_ID                 = 'char'
HEAT_OF_REACTION        = -45.0E3 /

&MATL ID                = 'char'
EMISSIVITY              = 1.0
DENSITY                 = 120.
CONDUCTIVITY            = 0.1
SPECIFIC_HEAT           = 1.0  /

&TAIL /
```

Annex E. Temperature development on the cold side predicted by MATLAB and FDS models compared to experimental measurements

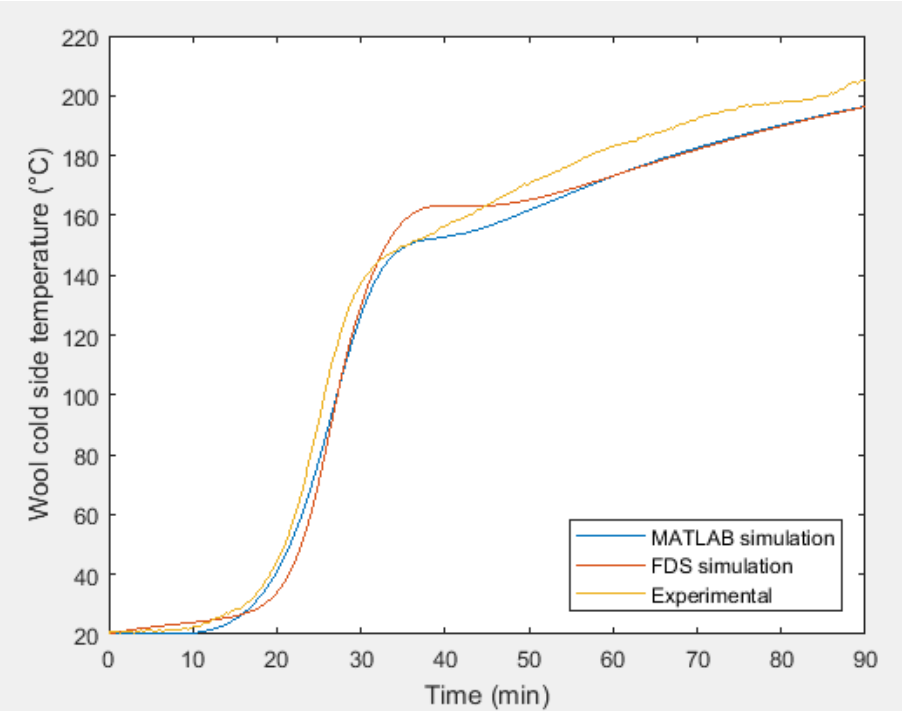

Figure 71. Wool 1.

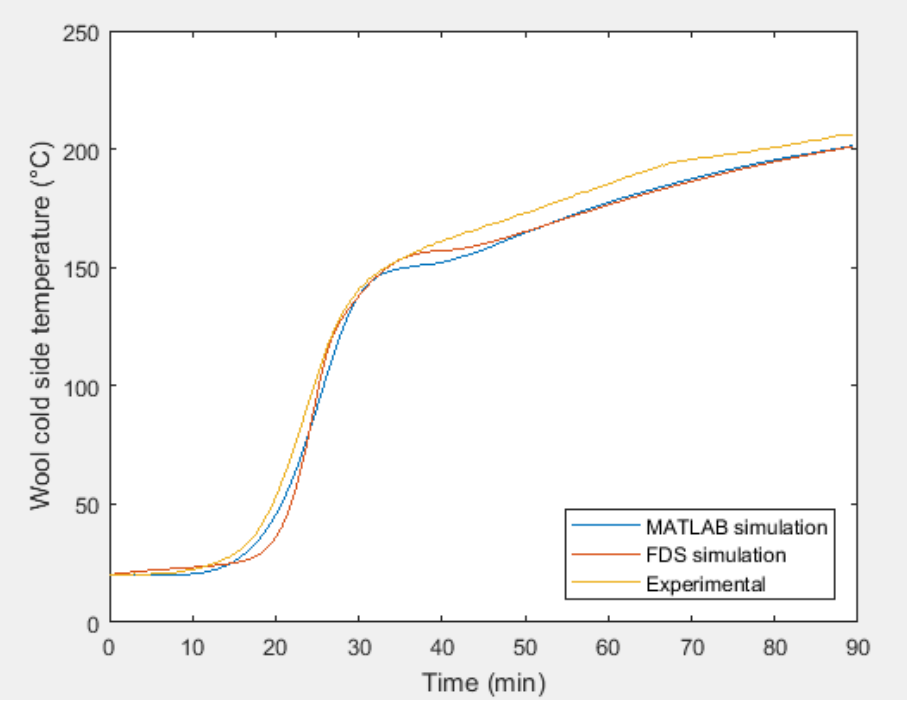

Figure 72. Wool 2.

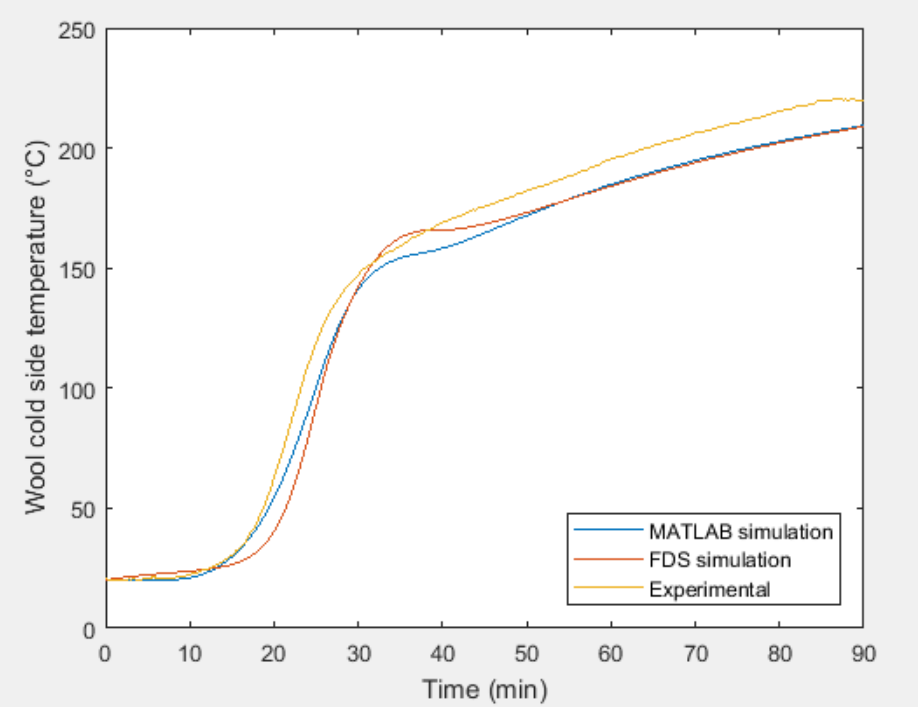

Figure 73. Wool 3.

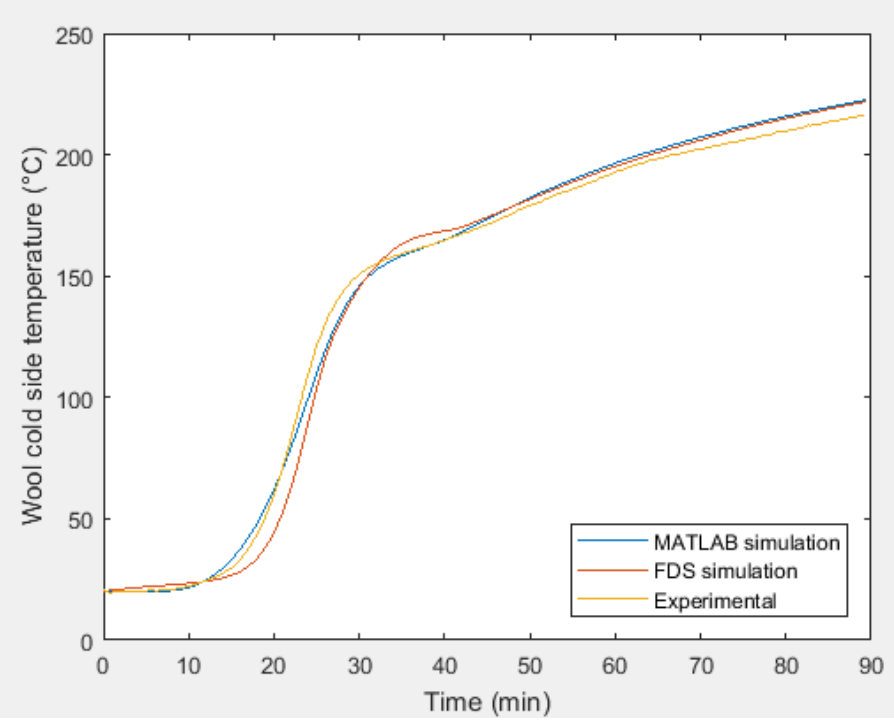

Figure 74. Wool 4.

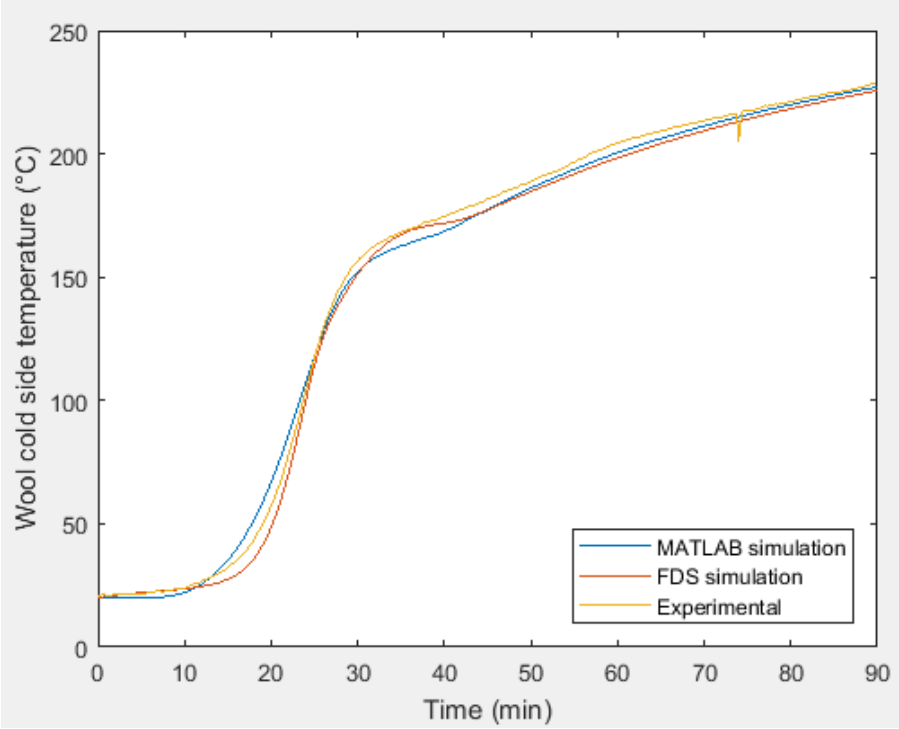

Figure 75. Wool 5.

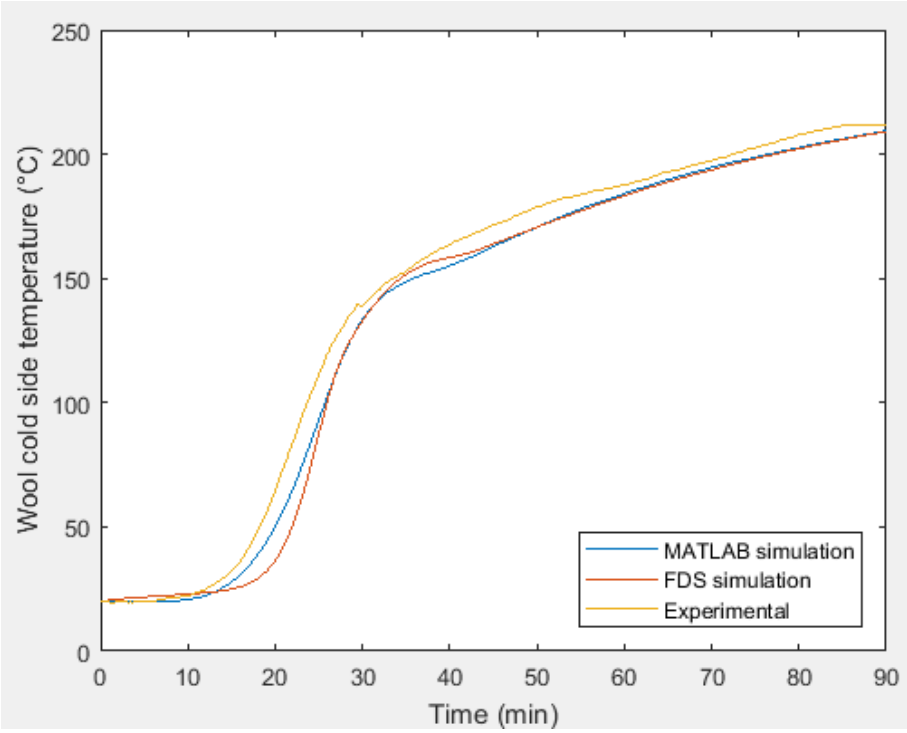

Figure 76. Wool 6.

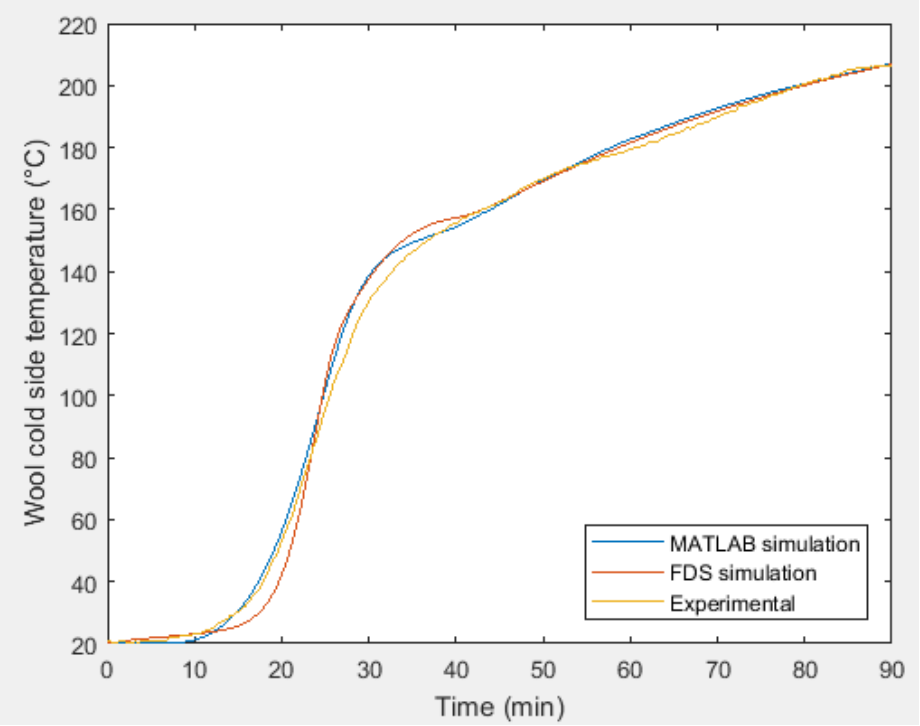

Figure 77. Wool 7.

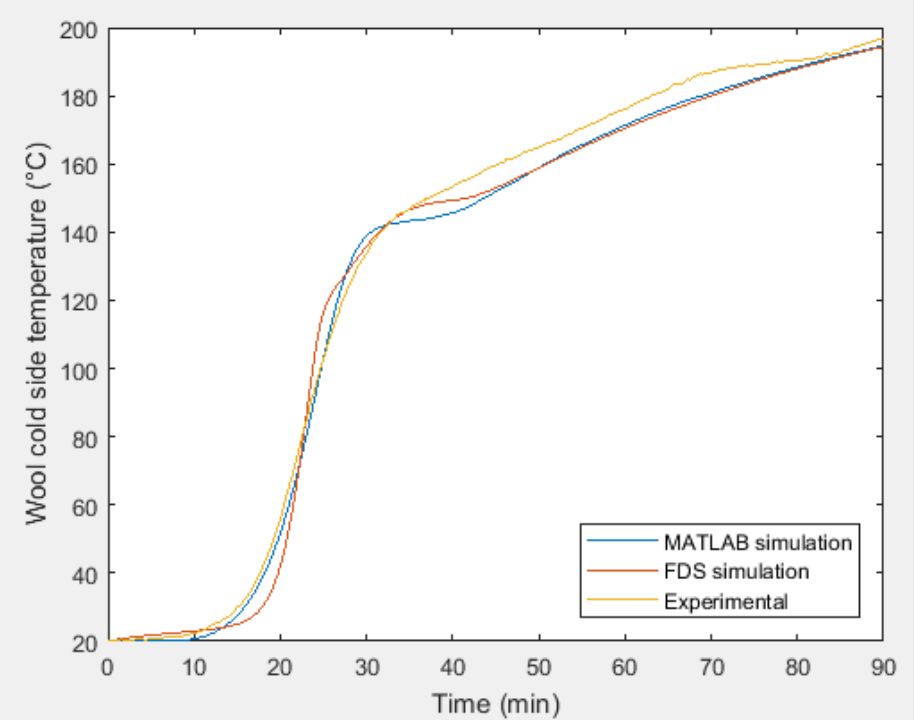

Figure 78. Wool 8.

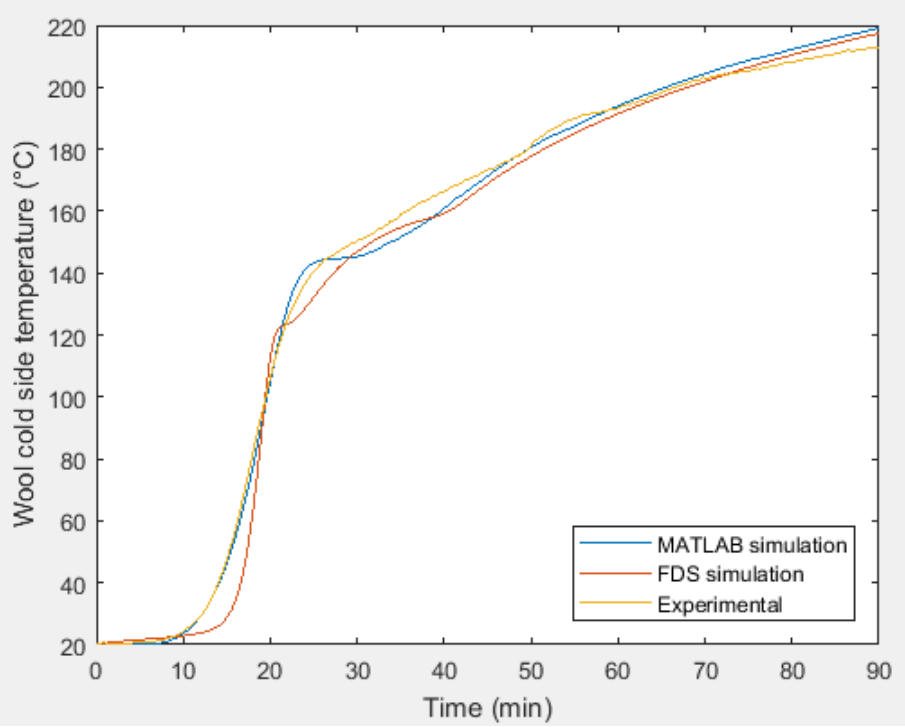

Figure 79. Wool 9.

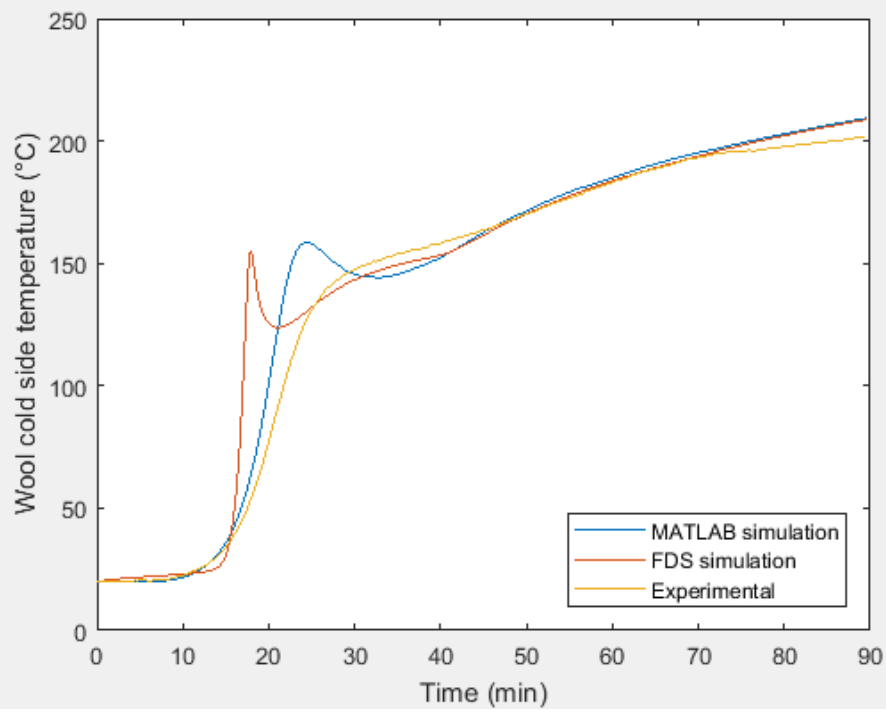

Figure 80. Wool 10.

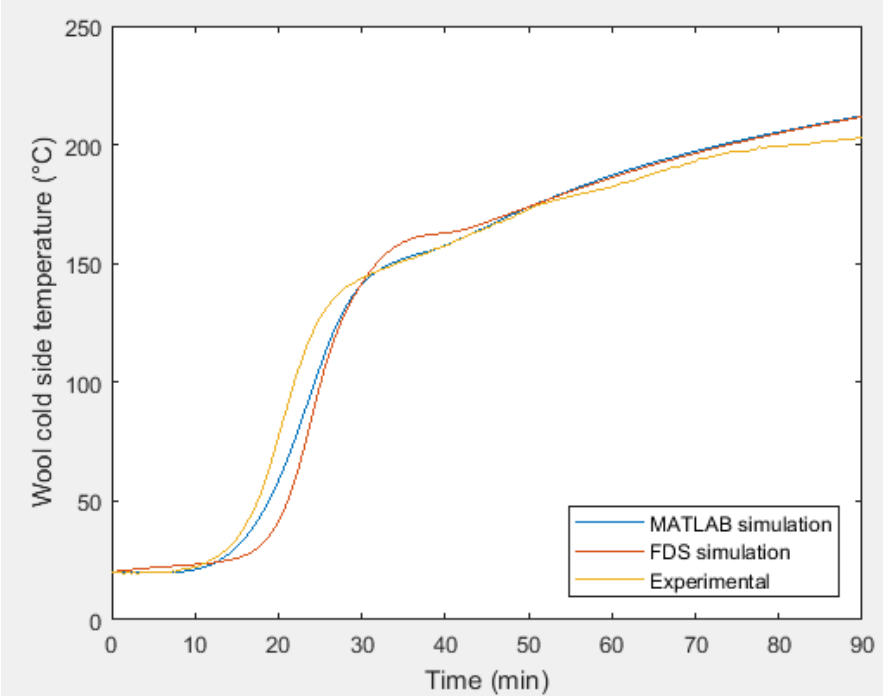

Figure 81. Wool 11.

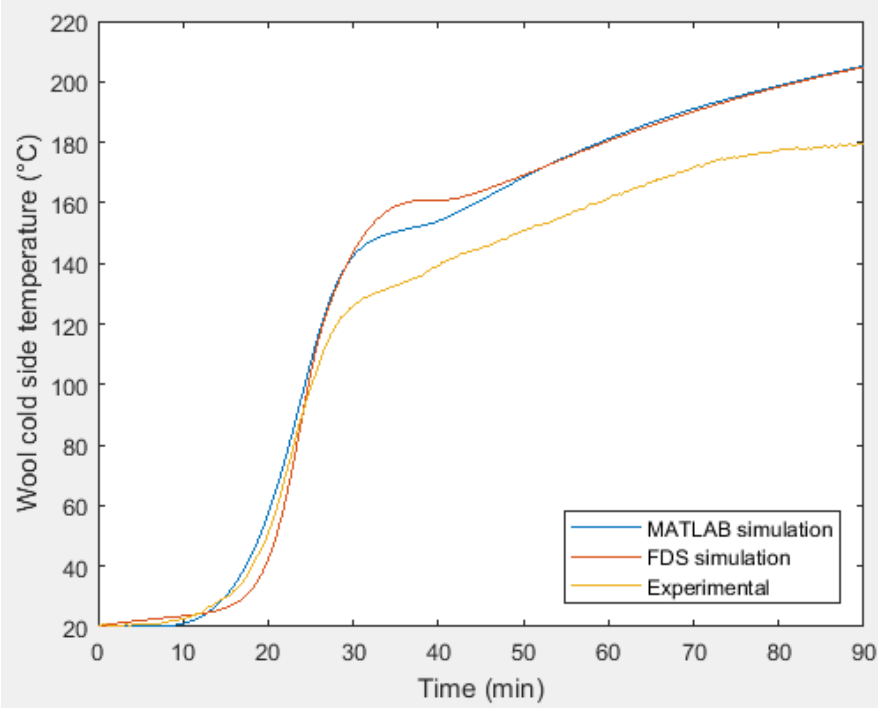

Figure 82. Wool 12.

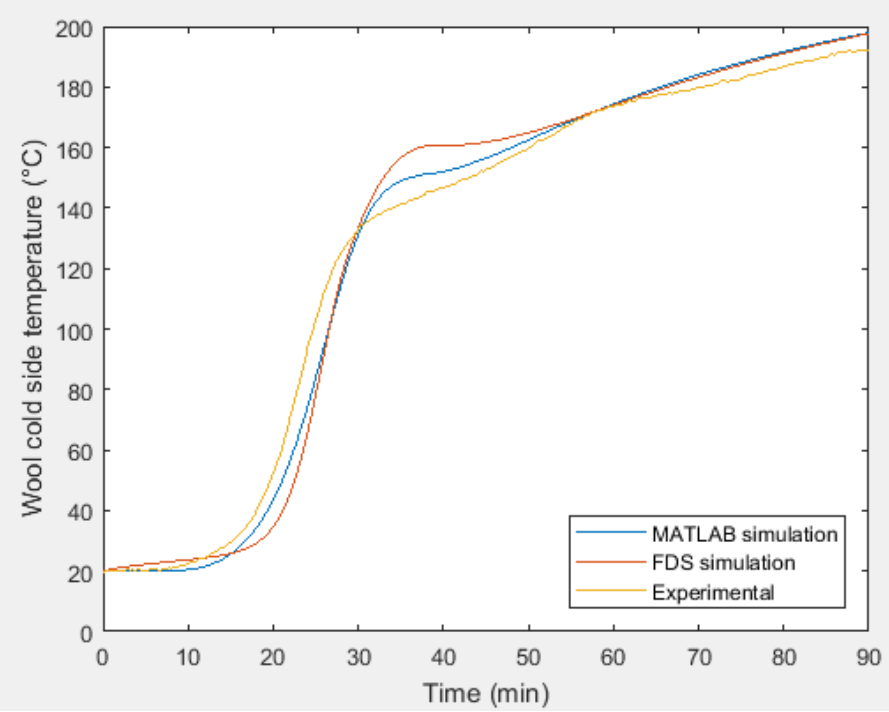

Figure 83. Wool 13.

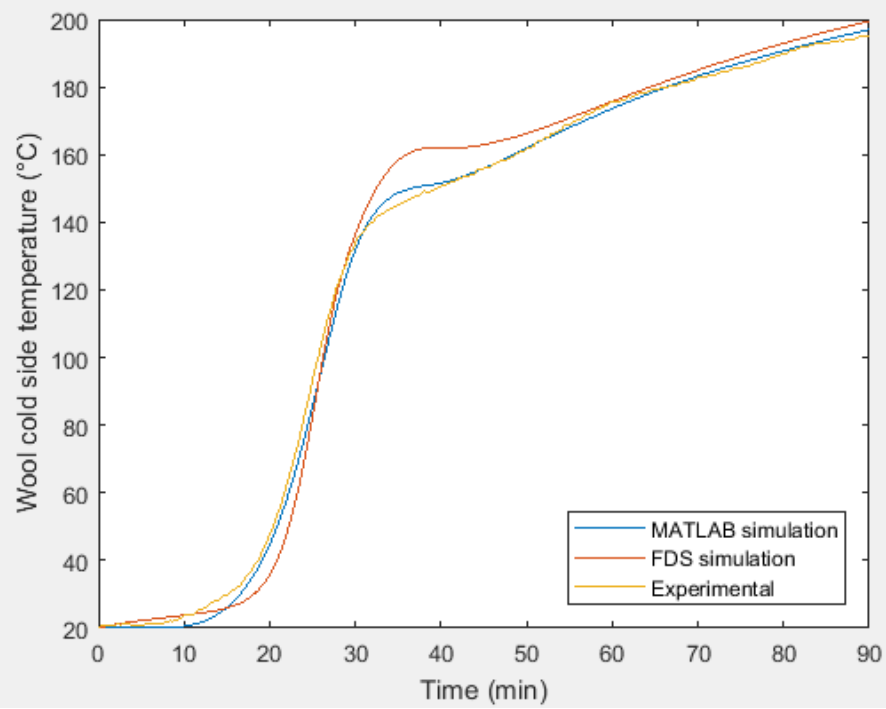

Figure 84. Wool 14.

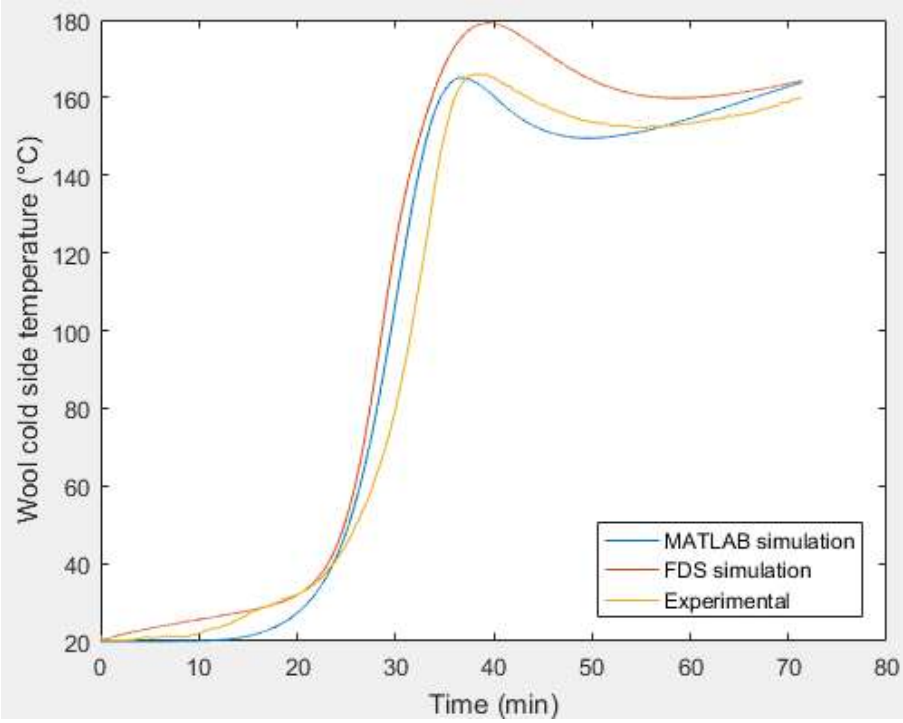

Figure 85. Wool 15.

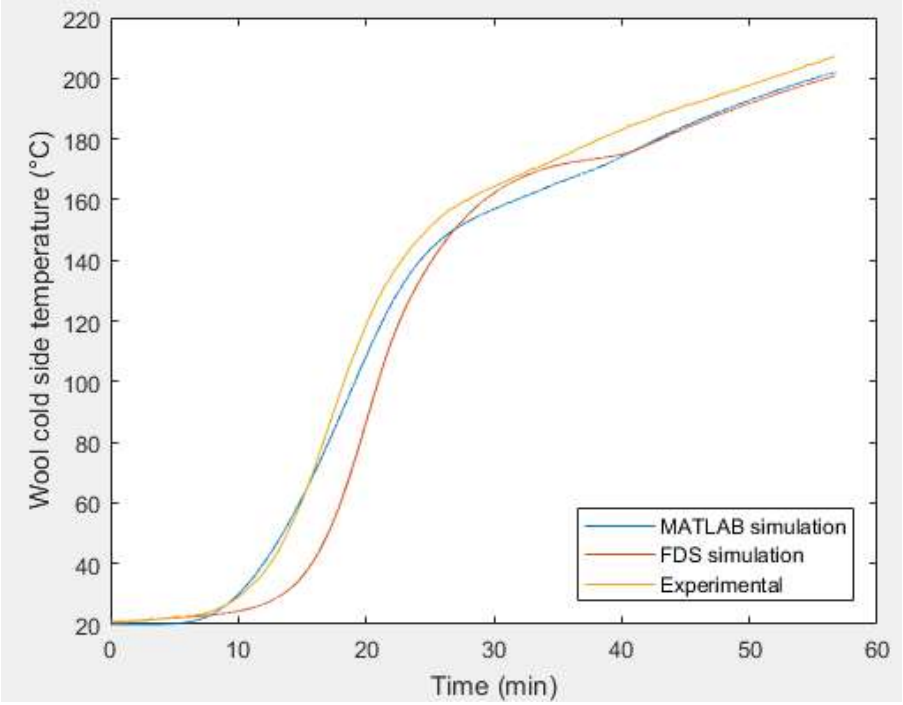

Figure 86. Wool 16

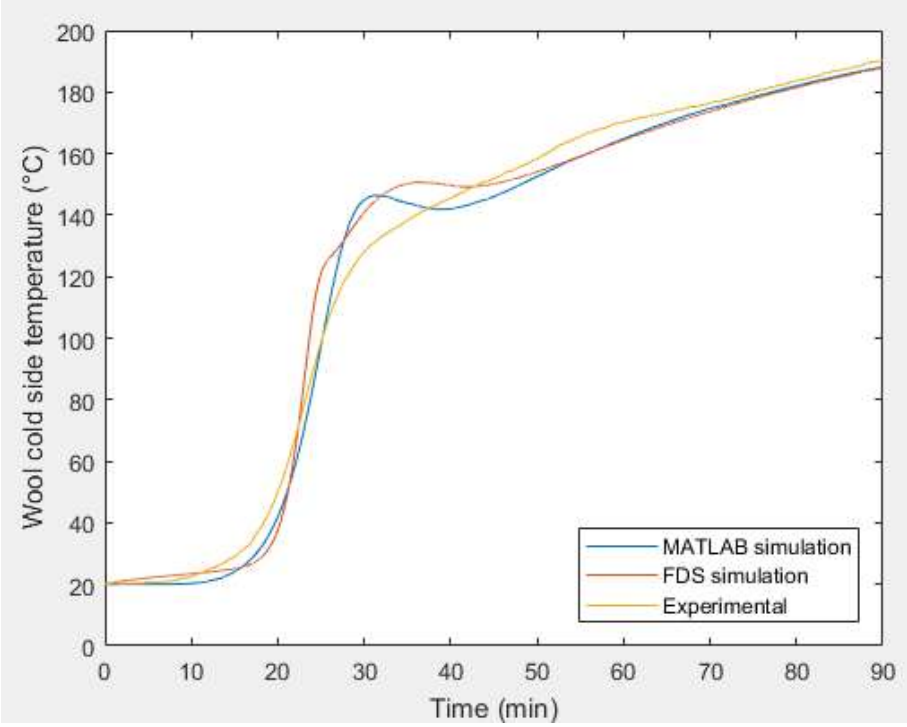

Figure 87. Wool 17.

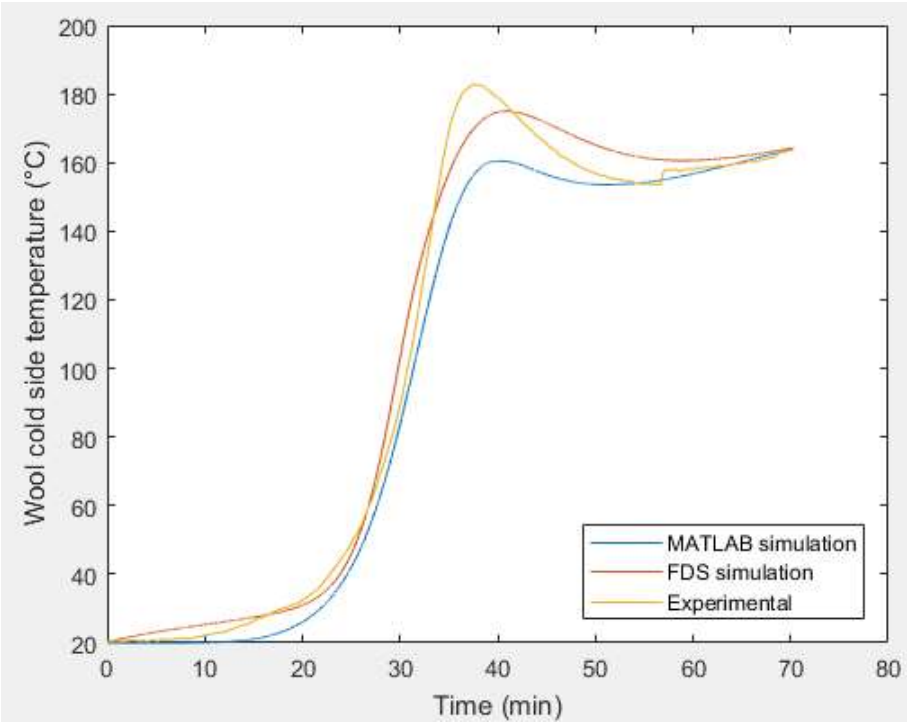

Figure 88. Wool 18.

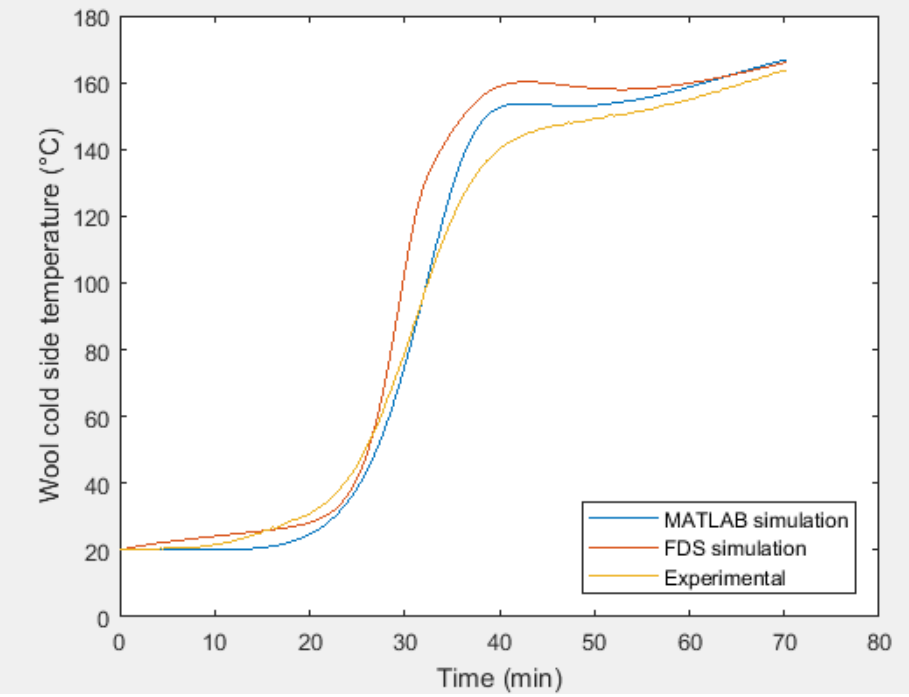

Figure 89. Wool 19.

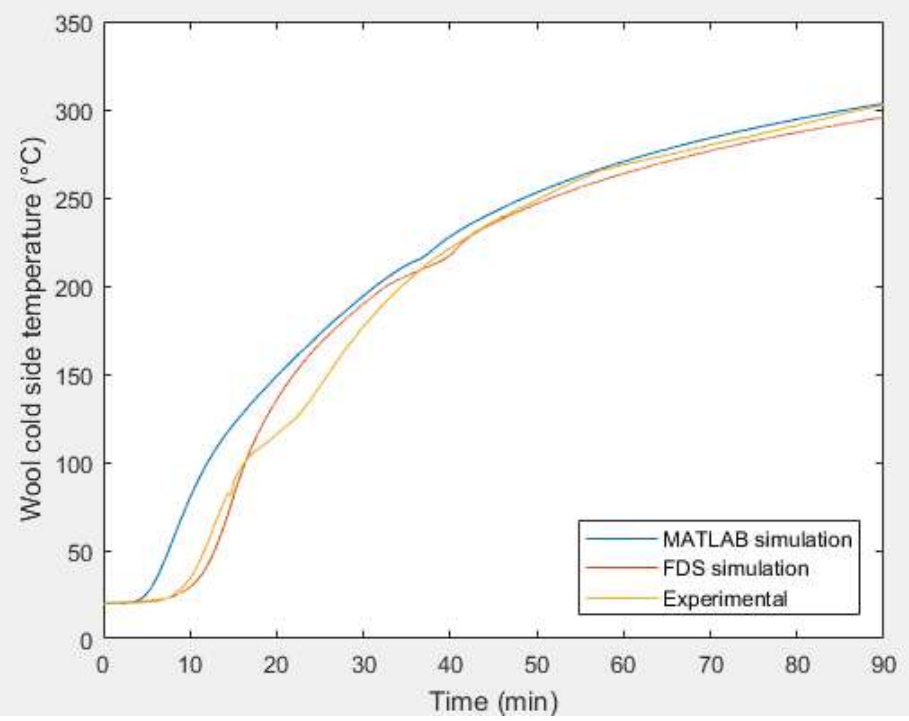

Figure 90. Wool 20.

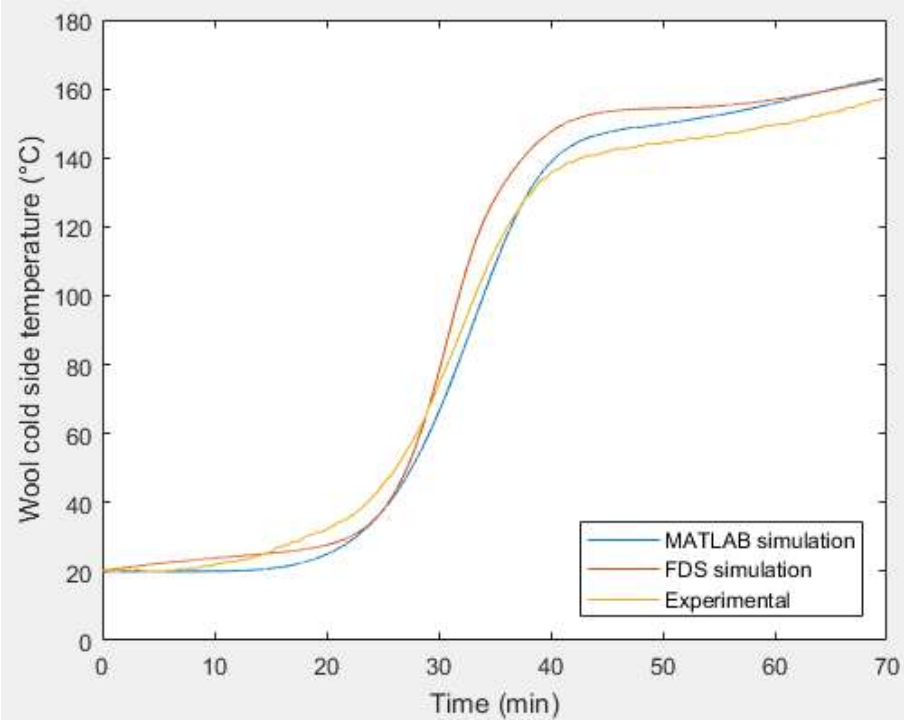

Figure 91. Wool 21.

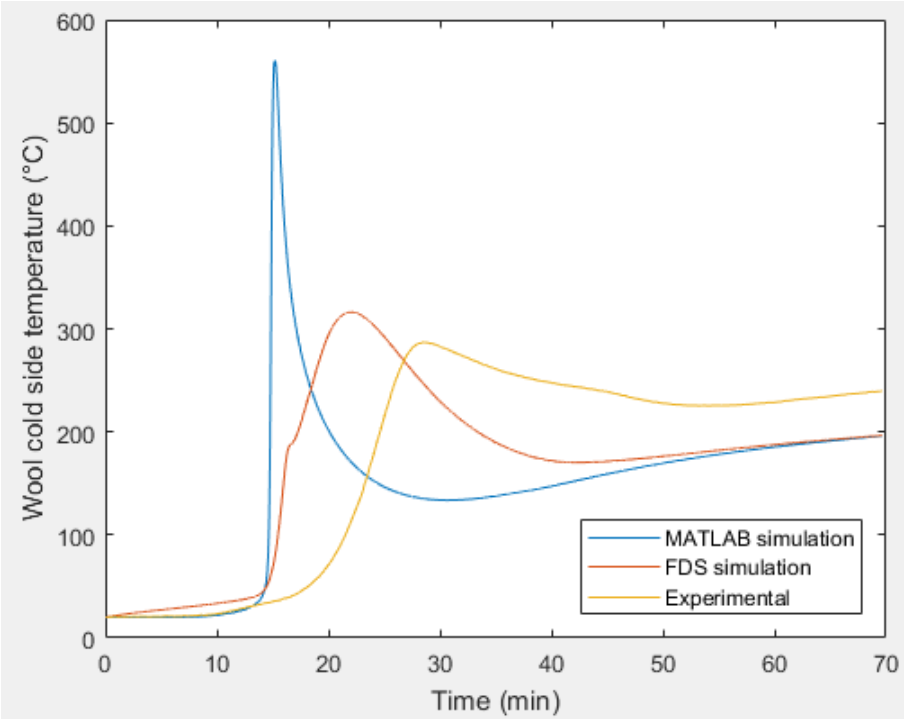

Figure 92. Wool 22.

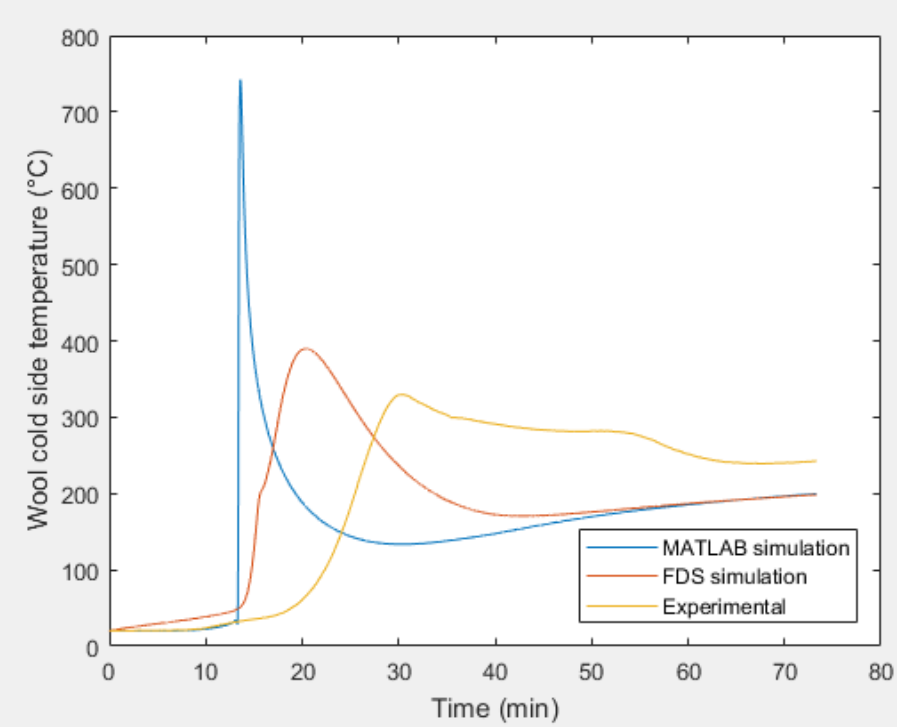

Figure 93. Wool 23.

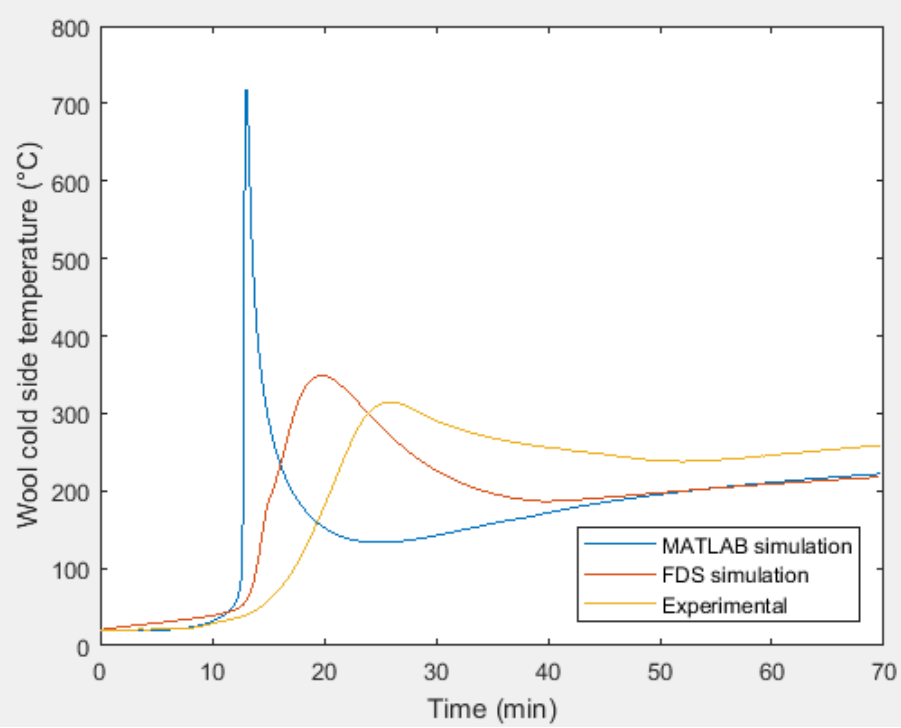

Figure 94. Wool 24.

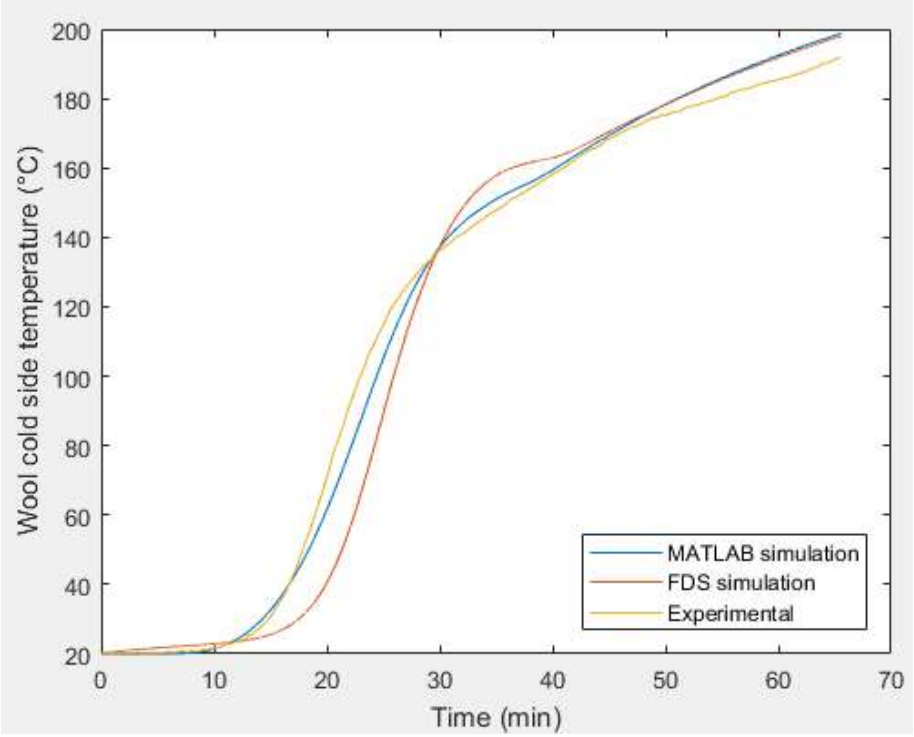

Figure 95. Wool 25.

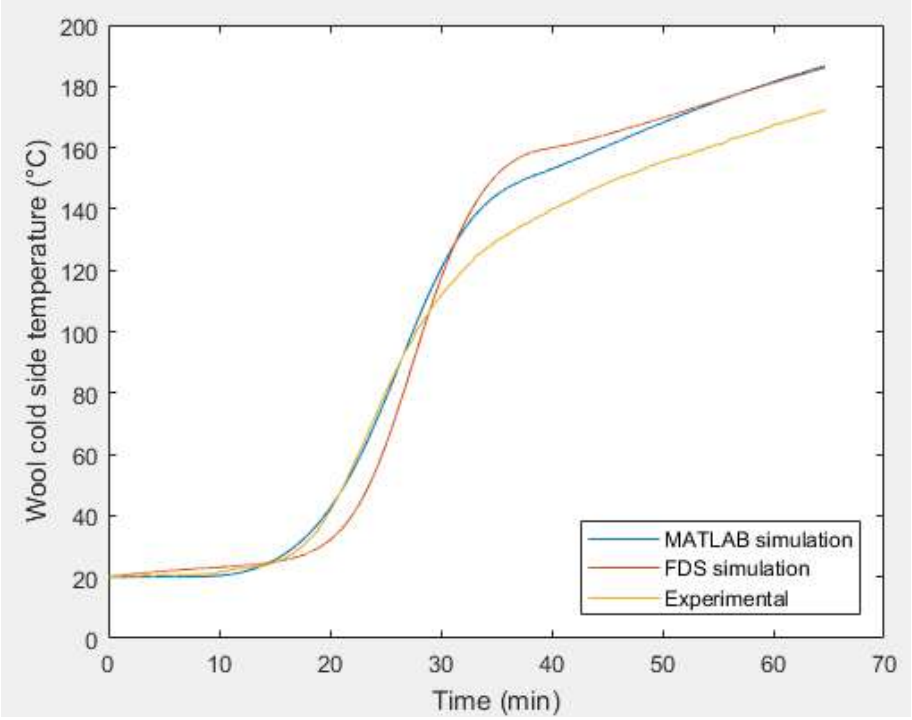

Figure 96. Wool 26.

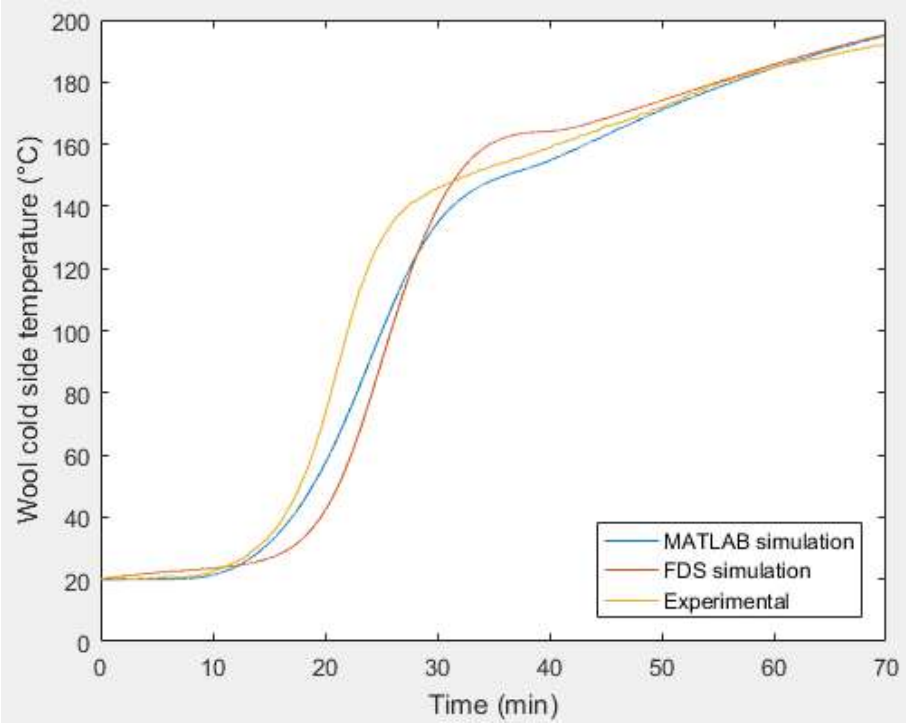

Figure 97. Wool 27.

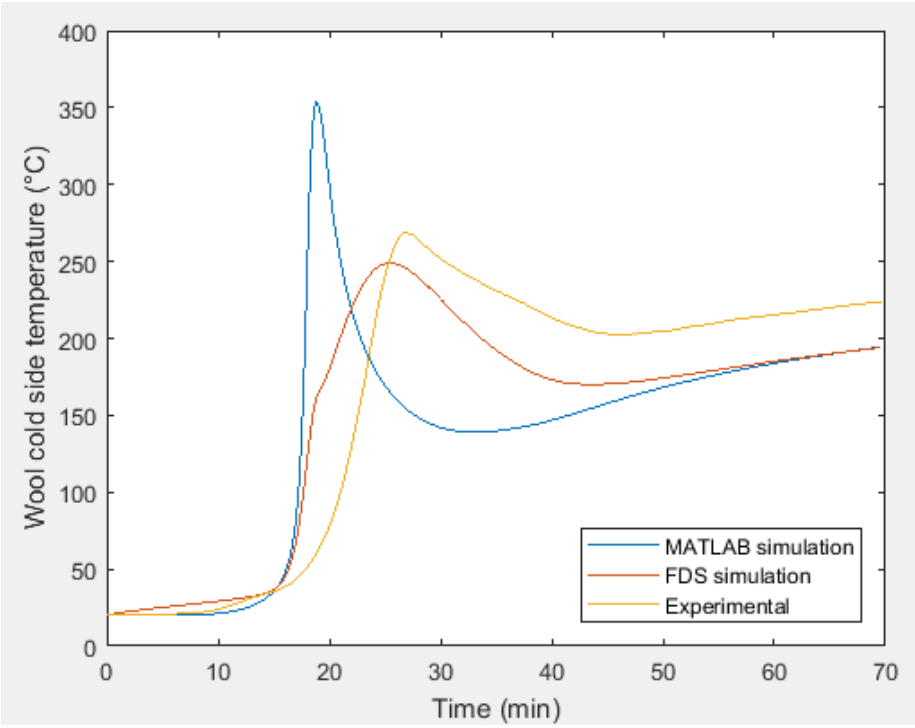

Figure 98. Wool 28.

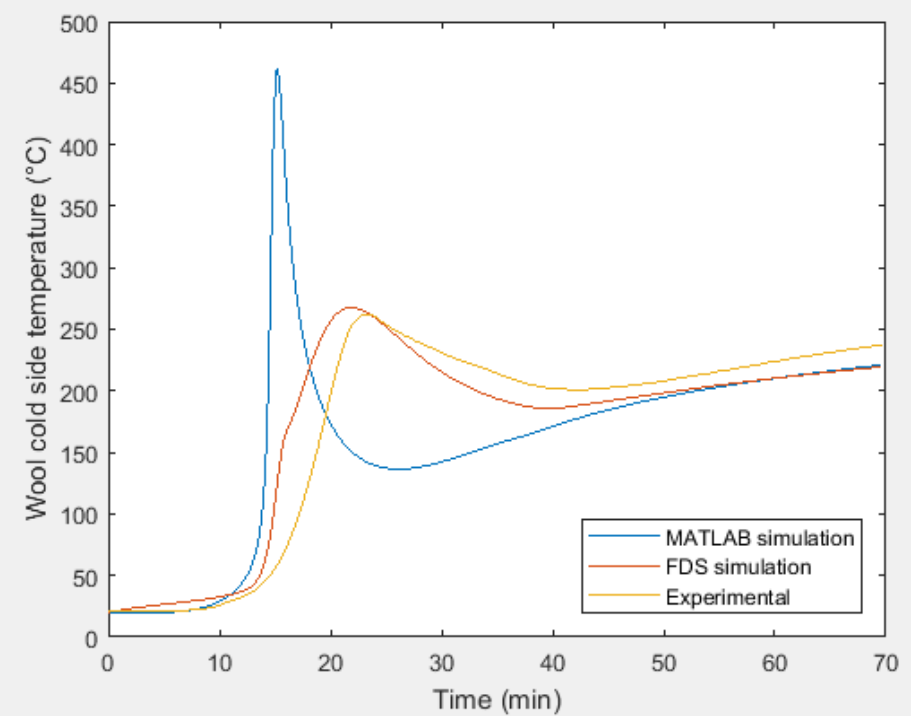

Figure 99. Wool 29.

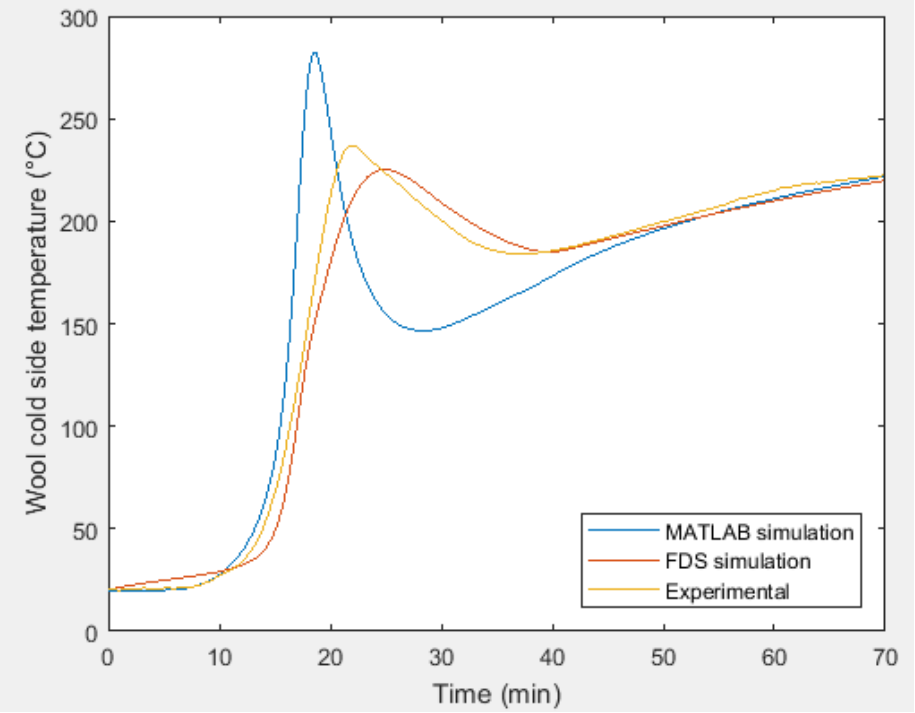

Figure 100. Wool 30.